國立中山大學材料科學研究所

碩士論文

中山 eThesys 學位論文

添加硼對高功能鎂銅釔合金非晶質化及奈米結晶行為之影響

Amorphization and Nanocrystallization Behavior in Mg-Cu-Y Alloy by Adding Boron

研究生：鄭宇庭 撰

指導教授：黃志青 博士

中華民國 九十四 年 七 月

Content

Table List

Figures List

論文摘要

近幾十年來，多元非晶質合金由於具有一些獨特的物理特性及化學特性，已引起眾多學者的研究與探討。而在這些多元非晶質系統中，鎂基非晶質合金因具有高強度重量比，低玻璃轉換溫度及輕密度等特性。因此在輕金屬應用中，佔有相當大的發展潛力及優勢。

本研究以在鎂基非晶質合金之中，具有高玻璃形成能力的$Mg_{65}Cu_{25}Y_{10}$非晶質為母材，藉由添加小原子尺寸的硼探討對母材熱性質、非晶質化及奈米結晶行為的影響。在實驗流程上，首先利用小型電弧爐及高週波爐熔鍊得到厚度約 100~200 μm鎂基非晶質薄帶，分別為$Mg_{65}Cu_{25-x}Y_{10}B_x$(x = 1, 3, 5, 10)及$Mg_{65}Cu_{25}Y_{10-x}B_x$(x = 1, 3, 5, 10)兩組系統，再利用XRD、TEM來觀察合金的非晶質化與結晶結構及DSC恆溫、非恆溫的結晶動力學研究與分析。

由非恆溫實驗結果發現，$Mg_{65}Cu_{25-x}Y_{10}B_x$(x = 1, 3, 5, 10)此組其結晶所需活化能經由Kissinger方程式計算，可得知從 138 kJ/mol提高至 156 kJ/mol，表示硼的添入有增加其母材熱穩定性；且ΔT_x與 γ 值於$Mg_{65}Cu_{22}Y_{10}B_3$合金成分時會有最大值分別為 66 K及0.420。而在恆溫實驗結果，經由Arrhenius 方程式計算也可推得其結晶所需活化能由原本母材的 150 kJ/mol 提升至$Mg_{65}Cu_{22}Y_{10}B_3$的 210 kJ/mol。推測由於硼的添加阻礙的原子間的擴散行為，進而增加第一個結晶相(Mg_2Cu)產生所需克服的活化能。此結果也與XRD所得結果相符，隨著硼元素的含量的增加，Mg_2Cu將會被抑制產生。

此外添加硼元素之後，$Mg_{65}Cu_{25-x}Y_{10}B_x$非晶相的硬度值也由 220$H_v$提高至 320$H_v$，而$Mg_{65}Cu_{25}Y_{10-x}B_x$非晶相的硬度值則由 220$H_v$提高至 290$H_v$，可推測硼原子的添入增加了結構的緻密度使得硬度質有效的提昇。

Abstract

The glass forming ability (GFA) of the lightweight $Mg_{65}Cu_{25}Y_{10}$ alloy has been widely studied. This alloy contains a medium sized Mg matrix (0.16 nm in atomic radius), a small sized Cu (0.14 nm) and a large sized Y (0.18 nm). The glass transition temperature T_g, supercooled temperature range ΔT, and the glass forming γ index are 425 K, 54 K, and 0.40, respectively. Follow-up studies have applied other large sized elements, such as Tb (0.178 nm) and Gd (0.18 nm), to replace Y, and resulted in satisfactory performance. It has recently suggested that the addition of the even smaller sized B (0.08 nm) in the Zr based bulk amorphous alloys to a certain level can further enhance GFA and provide the chance in fabricating larger bulk amorphous billet, partly due to the extra-small atomic size to complicate the atom arrangements and partly due to the absorption of oxygen by B. The current study extends the concept of adding B to the $Mg_{65}Cu_{25}Y_{10}$ based alloy, including the replacement of Y or Cu by 1-10 at% (1, 3, 5, and 10%), using the drop casting and melt spinning methods. The amorphous alloys are further subject to thermal annealing at temperatures within the supercooled temperature region in DSC, and the data are analyzed in terms of their thermal stability and crystallization kinetics under the isothermal or non-isothermal DSC conditions.

In the non-isothermal analyses, the activation energy of the $Mg_{65}Cu_{25}Y_{10}$ amorphous alloy for crystallization determined by the non-isothermal Kissinger method is 138 kJ/mol. With increasing B content, it can be promoted to a high energy barrier against crystallization, and $Mg_{65}Cu_{22}Y_{10}B_3$ has a higher value of 156 kJ/mol. T

As for the isothermal analyses, the activation energy values of the $Mg_{65}Cu_{25}Y_{10}$ and $Mg_{65}Cu_{22}Y_{10}B_3$ amorphous alloys for crystallization determined from the Arrhenius equation

are 150 and 200 kJ/mol, respectively. It means that boron can restrain the growth of Mg_2Cu. The $Mg_{65}Cu_{22}Y_{10}B_3$ amorphous alloy has the higher activation energy (210 kJ/mol) for crystallization, suggesting that the B diffusion away and the Cu diffusion toward the Mg_2Cu nuclei are also important.

中山 eThesys 學位論文

Chapter 1

Introduction and literature review

1.1 Introduction

Metallic glasses or amorphous metals, simply speaking, are referred to the systems lack of the crystalline long range order and exhibiting the liquid-like atomic arrangements as shown in Fig. 1.1 [1]. They have also been called liquid metals or non-crystalline metals alternatively.

Owing to the unique structure, metallic glass alloys show characteristic physical features such as high strength, corrosion resistance and electromagnetic properties, which are different from the corresponding crystalline alloys. The characteristics of metallic glasses are summarized in Table 1.1. Furthermore, in recent years more and more researchers worldwide discover better ways to synthesize the amorphous alloys using much lower cooling rates and new combinations of alloy compositions for glassy metals. It is believed that the metallic glasses will exhibit their significance for both basic research and application in the future.

1.2 The development of Mg-based amorphous alloys

Among a large number of amorphous alloys, Mg-based alloys have attracted much attention especially due to its high strength to weight ratio and a low glass transition temperature. Before the new Mg-based amorphous alloys with high tensile strength and good ductility were found in 1988 [2], the glass formation of Mg-based amorphous was limited to the Mg-Zn [3] and Mg-Cu [4] binary systems. However, the Zn and Cu concentrations were added to a level high as 20-40% and the resulting melt-spun ribbon would be highly brittle. Little has been known about the Mg-based amorphous alloys with high strength.

Until 1991, Inoue et al. [5] succeeded in finding new Mg-based amorphous alloys, such as Mg-Ln-TM (Ln=lanthanide metal; TM=transition metal) systems with high tensile strength. They also fabricated bulk metallic glass (BMG) with a diameter of 4 mm [6] by injection casting Mg-Cu-Y alloy into a Cu mold. Next year, Inoue's group used the high-pressure die casting method and increased even more the diameter to 7 mm [7]. Their contribution opened the door to design new families of light amorphous alloy systems.

1.3 Influence of quaternary additions on Mg-based alloys

Inoue et al. [8, 9,10] have reported the relationship between thermal stability of amorphous phase and the topological short range ordering. It is thought that the increase in packing density can cause an increase in thermal stability. The follow-up investigations on the Mg-based BMG have been directed to the addition of the quaternary element to improve the glass forming ability (GFA).

Recently, Park et al. [11] reported the effect of Ag as the substituting element for Cu on the GFA of Mg-Cu-Y-Ag. Due to the large difference in atomic size between Ag and the constituting elements, the larger mixing enthalpy of Ag-Mg and Ag-Y than that of Ag-Cu can contribute to increase the atomic packing density of the liquid structure and GFA.

Men et al. [12] also investigated the effect of substitution of Y in the $Mg_{65}Cu_{25}Y_{10}$ alloy with Gd on the GFA and crystallization behavior. Because of the difference in electronic configuration between Y ($4d^15s^2$) and Gd ($4f^75d^16s^2$), it results in a certain change of the short-range order in the undercoolded liquid of Mg-Cu-Y-Gd alloys, and shows a surprising high GFA. Other cases, for example, the $Mg_{65}Cu_{20}Zn_5Y_{10}$ [13] and $Mg_{65}Cu_{15}Ag_5Pd_5Y_{10}$ [14] alloys also exhibit high GFA and enable to fabricate metallic rods with diameters of 6 and 7 mm by a Cu-mold injection casting.

1.4 The purpose of this study

From the bibliography of Zr-Al-Ni-Cu amorphous alloy, by adding the small atom beryllium to substitute the zirconium not only decreases the excess free volume but also increases the disorder arrangement. It is apparent that GFA is improved from the DSC results and other measurements.

From the same view of topology, by the addition of the boron, it can also cause a large atomic difference in atomic size in the Mg-Cu-Y-B system and will generate strongly negative ΔH_m for Mg-B and Y-B. Also, the addition of boron may fill the liquid free volume and increase the density of randomly packed liquids; both will further improves the GFA and thermal stability against crystallization.

Chapter 2

Background

2.1 The evolution of amorphous alloys

Since the amorphous phase was first fabricated in the Au-Si system by rapid quenching from the melt in the early sixties [15], a great number of scientists have paid much attention to fabricate the new amorphous alloy systems in the bulk form. However, because of the high quenching rate higher than 10^7 K/s, only thin ribbons, foils or sheets with a thickness less than 100 μm could be fabricated.

Until 1976, the first bulk metallic glass, Pd-Ni-P [16] alloy, was fabricated by a simple suction casting method. More and more amorphous alloys were synthesized by various preparation methods. In 1980s, a variety of solid-state amorphization techniques, which are completely different mechanisms from rapid quenching as shown in Fig. 2.1, such as mechanical alloying, diffusion induced amorphization in multilayer, and ion beam mixing were developed. The diameter of bulk metallic glasses were also raised to the millimeter scale.

In the late 1980s, Inoue et al. [17] in Tohoku University of Japan succeeded in finding new multicomponent alloy systems consisting mainly of common metallic elements and proposed the empirical rules to form the bulk amorphous alloys with high GFA and lower critical cooling rate (R_c). According to the empirical rules, a number of bulk amorphous alloys with much lower R_c have been developed in multicomponent alloy systems and these new multicomponent alloy systems have enabled to produce the bulk amorphous alloys with a thickness range up to about 72 mm for the Pd-Cu-Ni-P alloy [18] by conventional solidification methods.

But owing to the cost and heavyweight of the Pd alloys, recent years, the lightweight glassy metals such as the Zr, Ti, Mg, Al base alloys with the aim of meliorating the specific strength were the developing emphasis. In addition, the alloys with the mixture of amorphous and nano-crystalline phases prepared from the crystallization of the original amorphous alloys have also attracted attention due to the various characteristics [19]. It is generally believed that the amorphous or the nanocrystalline alloys will own highly developing potential in the future.

2.2 The systems of glassy metals

The systems of glassy metals component can be divided into five major categories as shown in Table 2.1 [20]. The binary alloys consisting of metal and metalloid (such as Si, B, P) are the most popular glassy metals before 1988. But the disadvantages of these binary alloys are the very high cooling rate (10^6-10^8 K/s) to be vitrified and the small production size. Until the noble metal base amorphous alloys, such as Pd-Ni-P and Pt-Ni-P alloys with lower critical cooling rates of the order of 10^3 K/s [21] and larger size [22], were announced, the development of amorphous alloys makes a big breakthrough. Recently, the lightweight Mg-Ce-Ni amorphous with much lower cooling rates (below 10^3 K/s) was proposed by Inoue et al.. This kind of glassy metal has very high tensile fracture and large GFA. After that, the Mg-TM-Ln, Ln-Al-TM, Ti-Zr-TM and Zr-Al-TM amorphous alloy systems with great GFA and unique properties have been developed gradually. More recently, researchers focused on the multicomponent alloy systems, such as the Zr [23], Ti [24], Mg [25], Al [26] base alloys, because these alloy systems could be vitrified into a bulk form by casting with a much lower cooling rate of about 10 K/s and their supercooled region is wide. Table 2.2 [9] summarizes the typical bulk amorphous alloys systems reported since 1988 up to date, and they can be divided into the nonferrous and ferrous alloy systems.

2.3 The dominant factors for the GFA

The glass forming ability (GFA), as related to the ease of devitrification, is very crucial to understand the origins of glass formation and can act as a guideline for exploring new bulk glassy compositions. Initially, the GFA of an alloy was determined by the R_c. The high cooling rate was used to suppress the occurrence of the crystallization and to obtained the fully amorphous alloys. However, the exact value of critical cooling rare of some vitrification methods is not easily to measure. As a result, many other criteria have been proposed to reflect the GFA of the amorphous alloys in the basis of the characteristic temperature measured by differential thermal calorimetry (DSC) or differential thermal analysis (DTA).

The most extensively used are the reduced glass transition temperature, T_{rg} [27] (= T_g/T_l, where T_g is the glass transition temperature and T_l is the liquidus temperature, respectively) and the supercooled liquid region, ΔT_x (= T_x-T_g, where T_x is the onset crystallization temperature). Lu et al. [28] also show a better correlation with GFA by T_g/T_m for BMGs (T_m is the solidus temperature), but usually we take ΔT_x and T_{rg} as indicators of the GFA for metallic glasses. There is a clear tendency for the R_c to decrease with increasing T_{rg}, as shown in Fig. 2.3.

From the T_{rg} (= T_g/T_l) view of the point, T_l is dependent on composition, choosing the suitable concentration near the eutectic point so that the probability of being able to cool fast through the supercooled liquid region without any crystallization, i.e. GFA is increased. As to another parameter ΔT_x, the thermal ability also can be increased with increasing $T_{x.}$ Figure 2.4

reveals that the R_c also decreases with increasing supercooled liquid region, so the synthesized size of glassy metal will be increased.

Although both T_{rg} and T_x are used as indicators of the GFA, they sometimes show the contrasting trends versus GFA in some alloy systems [29, 30, 31]. Therefore, a new parameter, γ (= $T_x/(T_g+T_l)$), is proposed recently by Lu and Liu [32]. The definition of γ value is shown in Fig. 2.5. Table 2.3 [32] also reveals T_{rg} ,T_x, γ for various alloy systems. Furthermore the R_c (K/s) and the critical section thickness Z_c (mm) can be expressed by the following equations,

$$R_c=5.1\text{x}10^{21}\exp(-117.19\gamma), \quad (1)$$

and

$$Z_c=2.8\text{x}10^{-7}\exp(41\gamma). \quad (2)$$

These two equations reveal much better accuracy than T_{rg}, and have been successfully applied to the bulk glass formation of the Pd-Ni-Fe-P system.

2.4 The main empirical rules for the synthesization of amorphous alloys

Over the past decade, various methods developed to produce bulk metallic glasses were mostly empirical in nature, but researchers gradually began to understand that that the correct choices of elemental constituents would lead to amorphous alloys exhibiting critical cooling rates as slow as 1-100 K/s. One of the general guiding principles designing alloys to form bulk metallic glasses was proposed by Inoue. He summarized the features of alloy components for reduced instability of supercooled liquid and proposed three empirical component rules [33, 34, 35] to fabricate metallic alloys with high GFA: (1) multicomponent consisting of more than three elements, (2) significantly different atomic size mismatches exceeding 12% among the main three constituent elements, and (3) negative heats of mixing among the main elements. The alloys satisfying the rules and having special atomic configurations in the liquid state are significantly different from those of the corresponding crystalline phases. The empirical rules can also be explained by the thermodynamics, kinetics and structure aspects, as described below.

Firstly, from the thermodynamic point of view, it starts from the generally known relation of $\Delta G = \Delta H_{mix} - \Delta S_{mix}$. The low ΔG value can be obtained in the cases of low ΔH_{mix} and large ΔS_{mix}. The large ΔS_{mix} is expected to be obtained in multicomponent alloys systems because ΔS_{mix} is proportional to the number of component. Besides, the low ΔH_{mix}, i.e. the large negative heat of mixing among the three main constituent elements, is the main factor. The large negative heat of mixing is referred to the fact that the distinct atoms tend to bond together. Hence if there are three different elements mixed together and the difference in atomic size is large, the atomic configuration tends to appear as high dense random packing as shown in Fig. 2.6.

From the kinetic point of view, in 1969, Turnbull [36] has studied the relation between the nucleation rate and GFA in the supercooled region. He proposed the homogeneous nucleation and growth of a crystalline phase with a spherical morphology from the supercooled liquid can be expressed by the following relationships:

$$I = \frac{10^{30}}{\eta}\left[\frac{-b\alpha^3\beta}{T_r(1-T_r)^2}\right] (\mathrm{cm^{-3}s^{-1}}), \tag{3}$$

and $$U = \frac{10^2 f}{\eta}\left[1-\exp\frac{\beta(1-T_r)}{T_r}\right] (\mathrm{cms^{-1}}), \tag{4}$$

where T_r is the reduced temperature (= T/T_m; T_m is the melting point), b is shape factor and is

$16\pi/3$ for the spherical nucleus, η is viscosity and f is the fraction of nucleus sites at the growth interface. α and β are dimensionless parameters related to liquid/solid interfacial energy, σ, and can be expressed as $\alpha= (N_oV)^{1/3}\ \sigma/\Delta H$ and $\beta= \Delta S/R$. Here, N_o, V and R are the Avogadro number, the atomic volume and the gas constant, respectively. In these relationships, the most important parameters are η, α and β. The increase of the three parameters will decrease the I and U values, and further leading to an increase of GFA. Moreover, the increase of α and β also implies the increase in σ and ΔS and the decrease in ΔH, consistent with the interpretation of achieving high GFA derived from the thermodynamic point of view.

Furthermore, the atomic structure development also plays an important role for the mechanism of amorphous phase forming. Form the anti-Hume-Rothery criterion, the difference in atomic size ratios above 15% will induce a dense random packing in the supercooled region. The difficulty of atomic rearrangements attributes the formation of an amorphous phase and impedes the formation of a crystalline alloy.

Form the above described, the new amorphous alloys following these empirical rules must have a higher liquid/solid interfacial energy, leading to the suppression of nucleation of crystalline phase as well as the difficulty of atomic rearrangements. The latter contributes the low atomic diffusivity and high viscosity, leading to the difficulty of growing a crystalline phase. These mechanisms for the reduced instability and the formation of bulk glassy alloys are shown in Fig. 2.7.

Furthermore, there are many other empirical criterions for the glass forming ability. Shek et al. [37] have proposed that the composition of the amorphous alloys and their crystalline counterparts should possess a constant value of e/a. Fang et al. [38] have also proposed an empirical criterion between bond parametric functions that comprises of electronegativity difference and atomic size parameters to the relationship and the widths of the supercooled liquid region of Mg-Based bulk metallic glasses. It will be discussed thoroughly in the next section.

2.4.1 Bonding parameter for Mg-based BMGs

In order to further clarify the interatomic effect on GFA and thermal stability for the BMGs, the electronegativity difference (Δx) and atomic size parameter (δ) of multicomponent have also been introduced to explain the GFA of the Mg-based alloys, which show a nearly linear relationship with GFA [38]. The relationship is summarized in Fig. 2.8. The electronegativity difference Δx and atomic size parameter δ among the elements of a multicomponent alloy are defined by

$$\Delta x = \sqrt{\sum_{i=1}^{n} C_i \left(x_i - \bar{x}\right)^2} \quad , \tag{5}$$

and
$$\delta = \sqrt{\sum_{i=1}^{n} C_i \left(1 - \frac{r_i}{\bar{r}}\right)^2} \quad , \tag{6}$$

where C_i is the atomic percentage of the element i in the alloy; x_i and r_i are the Pauling electronegativity and covalent atomic radius of the element i, respectively; $\bar{x}$ and $\bar{r}$ are the arithmetical mean value of electronegativity and covalent atomic radius for a compound, respectively, which can be calculated as following equation:

$$\bar{x} = \sum_{i=1}^{n} C_i \cdot x_i \quad , \tag{7}$$

and
$$\bar{r} = \sum_{i=1}^{n} C_i \cdot r_i \quad . \tag{8}$$

In general, the larger the electronegativity difference Δx and the atomic size parameter δ would be, the higher the glass forming ability it becomes. The accuracy for judging the GFA of Mg-Cu-Y-B amorphous systems will be discussed in Chapter 5.

2.5 Characterization of amorphous alloys

The metallic glasses have various properties which are superior to the traditional crystalline materials due to their unique structure. And the unique properties are described below.

2.5.1 Mechanical properties

Due to the dense packing structure and irregular rearrangement of atoms, when the stress is applied, the amorphous alloys only allow small displacements of atoms to resist deformation without the invoke of dislocations as for the case of crystalline metals. Therefore, the amorphous alloys show higher tensile strengths than the traditional crystalline alloys, as shown in Fig. 2.9.

Moreover, the most useful characteristic of metallic glasses is their ability to be shaped and formed in the supercooled liquid region. This characteristic is related to superplastic behavior due to the Newtonian viscous flow. By utilizing the ideal superplasticity in supercooled liquid region, Zr-Al-Ni-Cu alloys [39] exhibit an extremely large elongation of 1.5×10^6 %. Furthermore, the strain rare sensitivity exponent (m-value) of amorphous alloys in supercooled region can reach 1.0 [40] under the deformation condition obeying the Newtonian flow behavior.

2.5.2 Magnetic properties

Permeability stands for the soft magnetic property of the material. Because the greater part of the magnetic materials is the pieces form, such as silicon steel lamination and wave filter, it is easy to fabricate the amorphous ribbons by melt spinning. Moreover, some amorphous alloys exhibit great permeability and minimum magnetic energy loss. Hence, the application of this kind of magnetic amorphous alloy has been very wide [41]. The typical magnetic amorphous alloy systems can be divided into two categories: TM-M and TM-TM (TM: Fe, Co, Ni, Zr, Hf, etc; M: B, C, Si, P, Ge, etc).

2.5.3 Chemical properties

The very high corrosion resistance has been observed in some amorphous alloys due to the homogeneous single-phased structure which is lack of grain boundaries, dislocations, and the other crystal defects. In addition, one can improve the corrosion resistance of amorphous alloys by adding some kinds of corrosive solute. For instance, the corrosion resistance of Zr-Al-Ni-Cu amorphous alloy increases as adding the corrosive solute, such as Nb, Ta, Ti, and Cr [42]. The other amorphous alloys, such as Pd-based as well as Fe-based [43] amorphous alloys, also have the highest corrosion resistance and they can serve as practical corrosion resistance materials.

2.5.4 Other properties and behavior of bulk amorphous alloys

For application of bulk metallic glasses as industrial materials, it is necessary to establish the bonding technology of BMGs. The major contribution in this aspect is made by Kawamura et al. [44]. They have reported that different bulk metallic glasses were successfully welded together by friction welding. Besides, the glassy state can be retained after the processes, and no crystallization and defect was observed in the interface. It is confirmed that, with careful control of the process parameters, the joints remain amorphous and the strength is comparable to the bulk of the metallic glasses.

2.6 Crystallization transformation of amorphous alloys

The amorphous solid is thermodynamically metastable, due to the Gibbs free energy difference between the amorphous and the crystalline states, the amorphous state will transform to the crystalline state under appropriate conditions (i.e., heat treatment, irradiation, or mechanical attrition). In general, the crystallization of an amorphous alloy takes place in there modes which are polymorphous, eutectic and primary crystallization.

Upon polymorphous crystallization, the crystallization of an amorphous phase transform to a crystalline phase without any change in the composition of that phase. This transformation may produce a single compound phase or a supersaturated solid solution phase. Upon eutectic crystallization, crystalline phases of different compositions form simultaneously. This reaction has no concentration difference across the reaction front, but takes longer than the polymorphous crystallization to proceed because the two components have to separate by diffusion into two separate phases within the crystallized region. Upon primary crystallization, a phase of the alloy constituents is first to crystallize. This dispersed primary crystallized phase coexists with the amorphous matrix and may serve as nucleation sites for the secondary or tertiary crystallization.

2.6.1 The Kissinger plot

Activation energy is one of the important parameters describing the transformation kinetics. In order to estimate the activation energy for crystallization, the Kissinger relation is frequently used for non-isothermal heating DSC analysis, and can be expressed in the form as [45,46]

$$\ln\left(\frac{\phi_m}{T_p{}^2}\right) = -\frac{Q}{RT_p} + \text{constant}\ , \tag{9}$$

where ϕ_m is the heating rate, T_p corresponds to the peak temperature of transition in DSC curves, R is the gas constant and Q is the transition activation energy. By plotting $\ln(\phi_m/\ T_p{}^2)$ against $1/\ T_p$, one can derive the value of activation energy Q from the slope of the straight line plotted.

2.6.2 Modified kinetics of non-isothermal crystallization kinetics

Due to the convenience and usefulness of Kissinger and Ozawa [47] equation, Kissinger plot and Ozawa plots have been extensively used to determinate the activation energy of crystallization. As a matter of fact, these methods could not clearly interpret the crystallization of amorphous materials and the physical meaning of the activation energy because crystallization involves both the nucleation and growth processes. Furthermore, the Kissinger equation is a series expansion of Avrami equation, it is not appropriate due to the fact that the temperature changes continuously under the non-isothermal condition.

Until 1979, Matusita and Sakka [48] proposed a method for analyzing the non-isothermal crystallization kinetics on the basis of nucleation and growth processes. By using this modified equation to express the non-isothermal crystallization, the results were in agreement with those obtained isothermally and the processes of nucleation and growth could be modeled separately from the modified plots. The details are described below:

The radius, r, of a crystal particle was expressed as

$$r = \int_0^t U(T)dt = \frac{U_0}{\phi}\int_{T_0}^{T} \exp\left(\frac{-Q}{RT}\right)dT \quad . \tag{10}$$

This integral could be evaluated to a closer approximation by using the Doyle’s p function.

$$p(y) = \int_y^\infty \frac{\exp(-y)}{y^2} dy \quad , \tag{11}$$

where y equals Q/RT. Equation (11) could be written as

$$p\left(\frac{Q}{RT}\right) = \frac{R}{Q}\int_0^T \exp\left(-\frac{Q}{RT} dT\right) \quad . \tag{12}$$

If the y value is larger than 20, equation (11) could be expressed to an approximation as

$$\log p(y) = -2.315 - 0.4567\,y \quad . \tag{13}$$

Combined equations (11), (12) and (13), r could be expressed as

$$r = \frac{C}{\phi}\exp\left(-1.052\frac{Q}{RT}\right) \quad . \tag{14}$$

Assuming at the early stage, crystal particles grow three dimensionally, the variation of crystal volume fraction, X, was expressed by

$$\frac{dX}{dt} = (1-X)N4\pi r^2 \frac{dr}{dt} \quad , \tag{15}$$

where (1-X) is the correction factor for the impingement of crystal particles, and the reduction of glass phase. Integration of equation (15) leads to $-\ln(1-X)=(4\pi/3)Nr^3$ and replacing with equation (14) leads to

$$-\ln(1-X) = CN\phi^{-3}\exp\left(-1.052\times 3\frac{Q}{RT}\right) \quad , \tag{16}$$

when the metallic glass is heated at a constant rate ϕ, the number of nuclei formed per unit volume is inversely proportional to the heating rate, $N= N_o/\phi$, and equation (16) could be converted to

$$-\ln(1-X) = CN_0\phi^{-4}\exp\left(-1.052\times 3\frac{Q}{RT}\right) \quad . \tag{17}$$

In more general expression, equation (17) should be expressed

$$-\ln(1-X) = CN_0\phi^{-n}\exp\left(-1.052\times m\frac{Q}{RT}\right) \quad . \tag{18}$$

Here, n and m are the numerical factors depending on the nucleation process and growth mechanism, respectively. The value of m=3 indicates that the growth of crystallization is three-dimensional growth. And the m=2 and m=1 are two-dimensional and one-dimensional growth, respectively. Taking the logarithm of equation (18) twice yields

$$\ln\left[-\ln(1-X)\right] = n\ln\phi - 1.052m\frac{Q}{RT} + \text{constant} \; . \tag{19}$$

The n value could be obtained from the plot of ln[-ln(1-X)] against lnϕ at a specific temperature. And the value of -1.052mQ/R also could be obtained by plotting ln[-ln(1-X)] versus reciprocal temperature for several heating rates. Furthermore, determining the m value was to observe the change of n in the early crystallization behavior. If n did not change with heating, a large number of nuclei formed already in the specimen and n = m. If n decreased with heating indicates that nuclei formed during the heating. In this case, $m < n \leq m + 1$. Normally, the maximum value of n is 4 and the minimum value is 1.

2.6.3 Isothermal analysis for the crystallization kinetics of amorphous alloys

Because the crystallization activation energy calculated by the Kissinger equation cannot reflect the stability of the amorphous phase, the further kinetic analysis of crystallization was carried out by isothermal DSC. The apparent transformation kinetics is usually described by using the Johnson-Mehl-Avrami equation (JMA equation) [49,50,51] measured at different temperatures between T_g and T_x. Furthermore, the JMA equation is derived assuming that the following conditions apply.

(1) Constant radial growth rate;
(2) Constant density and shape of the growing nuclei;
(3) No volume change during phase transformation;
(4) No secondary crystallization.

A general form of JMA equation is given as

$$X = 1 - \exp\left\{-(kt)^n\right\} \ . \tag{20}$$

Then take the logarithm of equation (20) twice derives equation (21)

$$\ln[-\ln(1-X)] = n\ln k + n\ln t\,, \tag{21}$$

where X is the volume fraction of transformed, n is the Avrami exponent and k is a kinetic coefficient which is a function of the absolute temperature. The crystallization mechanisms and morphology of crystalline phases can be obtain from the Avrami exponent. For the same n value, it indicates the same crystallization mechanism for the alloy. The values of exponent n for different kinds of crystallization mechanism are listed in the Table 2.4.

2.6.4 The Arrhenius plot

On the other hand, the activation energy can also be evaluated by the isothermal sigmoid curves of crystallized volume fraction versus annealing time at different temperatures. This was carried out by using the following Arrhenius equation [52] to the time required for a fixed amount of transformation X at different temperatures, which is determined by the following equation:

$$t(X) = t_0\exp\left(\frac{Q(X)}{RT}\right), \tag{22}$$

where t(X) is the time required to transform volume fraction X, t_0 is a time constant, and Q(X) is the activation energy for transformation. It can plot t(X) against 1/RT and further obtain the activation energy from the slope. The comparison of activation energy between Kissinger plots and Arrhenius plots will be discussed in Chapter 5.

Chapter 3

Experimental procedures

3.1 Materials

The elements used in this study were purchased from the WESIS company, Taipei, Taiwan. The purity of magnesium is 99.99%, of copper is 99.999%, of yttrium is 99.9% and of boron is 99.5%. The experimental flow chart and constituent contents of the alloys prepared in this study are shown in Table 3.1 and Fig. 3.1, respectively.

3.2 Synthesis methods

3.2.1 Arc melting

In order to prepare the multicomponent amorphous alloys, the arc melting method was first adopted in this study. Pure elemental pieces are used in this route. The applied device is the Centorr Series 5 Bell Jar Single Arc Furnace, as shown in Fig. 3.2. The maximum operating temperature is 3500^{o}C.

Before the starting of arc melting process, because crystallization will result from the oxygen impurity, the argon gas needs to be continuously purged into the furnace to flush the oxygen and maintain a positive argon pressure to ensure a low oxygen vapor pressure environment inside the furnace. Cold water also needs to be poured into and flowing through the bottom of the Cu mold to increase the heat exchange rate. Finally, the chosen component placed on the Cu mold will be melt by the high voltage arc under a Ti getter argon atmosphere. It should be repeated for more than four times to confirm the homogeneous mixing of composition. Besides, the cooling rate of arc process is not fast enough to form a fully amorphous alloys, so it needs to further conduct the drop casting or melt spinning process for complete vitrification of the alloys.

3.2.2 Melt spinning

To avoid the generation of magnesium vapor and the lose of constituent accuracy, the drop casting is not adopted in this study. The last metallic glass alloys will be produced by a single-roller melt spinning method. This method is generally recognized as a convenient way to form the amorphous alloys.

First, the Cu-Y specimen (made by arc melting), magnesium pieces, and the boron element are put into the low carbon steel crucible, and the crucible needs to spray a thin layer of BN to avoid the interaction between alloy and crucible at high temperatures. Next, similar to the arc melting process, the gas flushing step was performed several times before melt spinning. Then the crucible is placed in an induction furnace controlled by the high frequency system, and argon atmosphere is maintained to 2 atm in order to decrease the generation of magnesium vapor.

After complete melting, the liquid alloy will be poured onto the surface of Cu wheel. The wheel is rotated with a high speed of 25 m/s (20 Hz) in order to reach the high cooling rate. The resulting specimen is thin ribbon type with ~10 mm in width and ~100 μm in thickness. Small parts of ribbons are sampled for latter property characterizations.

3.3 Phase identifications by XRD

The vitrification degree of the ribbon structure fabricated by melt spinning can be first identified by the SIEMENS D5000 X-ray diffractometer (XRD) at room temperature. Filtered Cu Kα radiation operated at 40 kV and 30 mA, and 0.02 mm graphite monochrometer are employed. The diffraction angle covers from $2\theta = 10^o$ to 80^o at scanning rate of 1^o per 30 second. Note that a layer of alloys made by the melting spinning around 100~200 μm needs to be ground away to remove the possible oxidized outer surface. After the heat treatments, it also needs to run the XRD to identify the phase of crystallization.

3.4 SEM/EPMA observations

Because of the smallest molecular weight of boron, SEM/EPMA (scanning electron microscope/electron probe microanalyzer) is selected to measure the quantity of chosen components. The sliced specimens from the ribbon need to be coated with a thin gold layer gold, and the JEOL 8900R EPMA equipped with Wavelength Dispersive X-ray Spectrometer (WDS) is used for the qualitative analyses.

3.5 Microhardness testing

The sample hardness testing was conducted using a SHIMADZU HMV-2000 Vicker's microhardness tester. Because the restrict of ribbon thickness, the samples were only grounded by silicon carbide abrasive papers (#800 and #1000) with water before the hardness measurement. In this testing, the parameter was carried out using a load of 200-500g with 10 second duration, and the hardness value of each sample was average from 10 datum points. The microhardness data can also be used to investigate whether the boron would cause a dense atomic structure and compared with the Mg-Cu-Y amorphous alloy.

3.6 Density measurement

Form the simple and reliable points of view, the well-know principle of Archimedes is used as an appropriate means to measure the specimen density. In this technique, the specimen contained in a vessel is weighted in air to record a value of mass W_1. Then, the specimen is weighted in a liquid of known density β to record a second value of mass W_2. Therefore, the density of amorphous alloy can be evaluated by the following equation :

$$\rho = \frac{W_1}{W_1 - W_2/\beta} \quad . \tag{23}$$

The atomic configurations of amorphous alloys are different from those of the crystalline alloys. It is expected that the short-range atomic configuration changes the density of the new amorphous alloys. Normally, the densities would increase when the amorphous phase is transformed through structural relaxation or crystallization.

3.7 DSC thermal stability analysis

The differential scanning calorimeter SETARAM DSC131 is used in this study. It can examine the thermal stability and determine the values of T_g, T_x, T_m by the heating process, as shown in Fig. 3.4. Other data such as nucleation, growth behavior, and activation energy can also be estimated from the isothermal or non-isothermal analysis. The heating rate is set to be 10-40^{o}C/min and each run begins from 40^{o}C and ends at 600^{o}C in this study. Normally, the DSC programs for non-isothermal and isothermal analyses are set as shown in Fig. 3.5. Moreover, in order to prevent oxidation and magnesium vaporization at high temperatures, samples are placed in stainless steel crucibles and tightly sealed with a nickel ring. The pre-existing air in the chamber is flushed by pure Ar and the positive Ar pressure is maintained wile heating.

3.8 Microstructure characterizations

Because the X-ray results are all referred to the averaging measurements for the bulk volume and the SEM results are limited by the image resolution, the spatial distribution between nanocrystalline and amorphous phase needs to rely on the transmission electron microscopy (TEM). Microstructure observations in this study are conducted using the JEOL 3010 analytical TEM operated at 200-300 keV with Link EXL-Ⅱ Energy Dispersive X-ray analysis, (EDS). And the EDS system is used to identify the composition of the observed phase.

The TEM samples were first punched mechanically and then ground by silicon carbide abrasive papers (#1200, #1500, and #2000) with water. Next, the TEM foils need to be adhered to a mesh 200 Cu net. Finally, the TEM foil is thinned by the Gatan 691 precision ion polishing system to produce high quality TEM specimens.

Chapter 4

Experimental Results

4.1 Specimen preparations

Since the boiling point of Mg is lower than the melting point of Cu, Y and B, respectively, the master ingot of Cu-Y binary alloy was first prepared by arc melting under a Ti-gettered argon atmosphere. Then the ingot was melted with pure Mg and B in an induction furnace under a purified argon atmosphere. Finally, glassy ribbon samples were obtained by rapid solidification of their melts on a single copper roller, as shown in Fig. 4.1. During these processes, how to keep the accuracy of constituent quantity plays a major role on the GFA of the resulting amorphous alloy. Therefore, the crucible is designed to have a cap and to keep minimum the evaporation of the pure Mg component.

The characteristic of BMG is identified as having a mirror like luster on the surface. As shown in Figs. 4.2 to 4.3, the melt spun Mg-Cu-Y-B alloys also have this distinguishing characteristic. Furthermore, the difference in the bending ductility of melt spun alloys can also be differentiated in terms of critical bending angle for fracture. For ductile ribbons, the bending angles can be as high as 180^{o} or the ribbons can be fully folded. For brittle ribbons, the bonding angles would be less than 90^{o}. The Mg-Cu-Y parent metallic glass exhibits ductile behavior with a 150^{o} bending angle. With increasing B content, the samples perform more and more brittle tendency and become easily splintered into pieces.

4.2 X-ray diffraction analyses

Figure 4-3 shows the X-ray diffraction pattern of the melt spun $Mg_{65}Cu_{25}Y_{10-x}B_{x}$ (x = 0, 1, 3, 5) alloys with Y replaced by B. It is apparent that the $Mg_{65}Cu_{25}Y_{10-x}B_x$ alloys exhibit an almost fully amorphous phase except for a couple of small peaks superimposed on the amorphous diffused hump located at 2θ ~35^o and 37^o in the alloy with 5 at.% boron content. The tiny peaks are identified to be the Mg_2Cu crystalline phase with an orthorhombic structure plus minor MgB_4, as shown in Fig. 4.4. For a more boron addition to 10at% so as to completely substitute yttrium, or the $Mg_{65}Cu_{25}Y_{10}$, only the sharp Mg_2Cu peaks are visible in the XRD curve, as shown in Fig. 4.5. However, from the Fig. 4.6, only board diffused amorphous hump occurs and no obvious crystalline peak is seen in the melt spun $Mg_{65}Cu_{25-x}Y_{10}B_x$ (x = 0, 1, 3, 5, 10) alloys with Cu replaced by B. The above XRD results imply that the partial substitution of copper and yttrium by boron has the different effects on the GFA.

Furthermore, in order to identify the different crystallization phases from the $Mg_{65}Cu_{25-x}Y_{10}B_x$ and $Mg_{65}Cu_{25}Y_{10-x}B_x$ two systems, the as-melt-spun amorphous ribbons were annealed at various temperatures in DSC and then characterized by X-ray diffraction, as presented in later sections.

4.3 SEM/EPMA observations

In order to confirm the absence of any crystalline phase over the whole sample, a SEM/BEI composition image taken from the polished surface of the Mg-Cu-Y metallic glass is shown in Fig. 4.7 (a). It can be seen that no contrast of precipitation is seen over the whole micrograph. Furthermore, from the SEM/EDS observation, the elements of Cu and Y are uniformly spread in the Mg matrix, as shown in Fig. 4.7 (b). Hence by using melt spinning to solidify, the high cooling rate and uniform composition can be obtained.

4.4 Microhardness tests

The sample hardness is measured using the HMV-2000 microhardness tester. Ten positions are chosen randomly for each sample, then the Vickers hardness (H_V) are obtained by indenting each sample at a load of 500 g and measuring the indentation size by optical microscopy.

Microhardness results of the $Mg_{65}Cu_{25-x}Y_{10}B_x$ and $Mg_{65}Cu_{25}Y_{10-x}B_x$ amorphous alloy systems are shown in Fig. 4.8. It is apparent that the H_V is sensitive to the addition of boron. With increasing the boron content, higher H_V data would be obtained. But the $Mg_{65}Cu_{25-x}Y_{10}B_x$ alloys have the higher Hv value than the $Mg_{65}Cu_{25}Y_{10-x}B_x$ amorphous alloy. The highest H_V of 321 is obtained for $Mg_{65}Cu_{20}Y_{10}B_5$, which is significant higher than the value of 220 for the parent $Mg_{65}Cu_{25}Y_{10}$ alloy. The atomic arrangement and whether the nanocrystalline phase exist may be the reason of different for Hv.

Furthermore, when the sample is applied a compression by the indenter, the plastic deformation morphology can be seen in the form of the pile-up of the semi-circular shear bands, as shown in Fig. 4.9. In a crystalline material, these bands extend a short way along the grain boundary then stop when they run into a crystal, but in amorphous substance these bands just keep on growing at stress point. Because the element of copper and yttrium are ductile in the Mg-Cu-Y-B system, lots of shear bands appeared but each one was small and thin. These bands appear to increase to overall toughness by interfering with each other so that no one band can extend into a long crack.

4.5 Density measurements

Due to the improvement of the hardness in the Mg-Cu-Y-B amorphous alloys, the atomic arrangement is of concern. The simplest method to detect whether the volume is changed is to measure the density. Table 4.1 shows the density results obtained by means of the Archimedean theorem. The $Mg_{65}B_{25}Y_{10}$ based alloy has the smallest density value 3.09 g/cm^3. The density values of $Mg_{65}Cu_{25-x}Y_{10}B_x$ (x = 3,5) systems are 3.46 and 3.24 g/cm^3, respectively. And the $Mg_{65}Cu_{25}Y_{10-x}B_x$ (x = 3,5) systems have the higher density values 3.81 g/cm^3 and 3.74 g/cm^3, respectively.

4.6 Thermal analyses

4.6.1 Non-isothermal analyses and kinetics

In order to understand the origin of the high thermal stability and excellent glass-forming ability, it is very important to clarify the crystallization behavior of the supercooled liquid. By using the DSC instrument, it is sensitive to detect the glass transition and the nanocrystallization.

In the $Mg_{65}Cu_{25-x}Y_{10}B_x$ alloy systems, from the Figs. 4.10 to 4.13, all the samples exhibit a distinct glass transition, followed by a wide supercooled region and then exothermic reactions due to crystallization. Figure 4.14 shows with increasing x from 0 to 3, the glass transition temperature is nearly constant at 410 K but the crystallization temperature increases slightly from 468 to 476 K. Therefore, the ΔT_x value also slightly increases from 58 K at x = 0 to 66 K at x = 3. With further increasing x to the 5 and 10 at%, ΔT_x becomes smaller with the addition of B content, 50 K for 5 at% B and 45 K for 10 at%. Figure 4.15 shows the variations of T_g, T_x against the B content. It is suggested that the B substitution for Cu is of no harm for the GFA of Mg-Cu-Y amorphous alloy.

In contrast, the shape of the $Mg_{65}Cu_{25}Y_{10-x}B_x$ alloy systems is different, as shown in Fig. 4.16. With increasing x from 0 to 5, it is noticed that the first exothermic peak for x = 0 splits into two exothermic peaks for alloys with x＞3. Furthermore, Form Fig. 4.17, the shape of these two curves is greatly different. The $Mg_{65}Cu_{22}Y_{10}B_3$ alloy, only one sharp exothermic peak with high enthalpy of transformation is observed. This is due to the fact that this alloy is presumed to have a higher degree of dense random packed structure. It indirectly indicates the different atomic arrangement between the $Mg_{65}Cu_{25-x}Y_{10}B_x$ and $Mg_{65}Cu_{25}Y_{10-x}B_x$ systems.

The melting behavior of Mg-based low melting alloys is also determined using the DSC at a heating rate of 20 K/min. The ratio of the glass transition temperature T_{rg} and the offset melting temperature (liquidus) T_l, is often used as a parameter to estimate the GFA. From the former study [19], $Mg_{65}Cu_{25}Y_{10}$ exhibited a single endothermic peak with a narrow melting range about 30 K. The onset and offset temperatures of the melting designated by T_m^{solid} and T_m^{liquid} are 728 and 760 K, respectively. It indicates that the $Mg_{65}Cu_{25}Y_{10}$ alloy is close to the ternary eutectic composition.

Compared with the parent alloy, from Fig. 4.18, the T_m^{solid} of the x = 3 and 5 alloys decrease to about 715 and 712 K, and T_m^{liquid} also decrease to about 738 and 736 K. Although the x =3 alloy has two endotherm peaks, the lower melting point and small melting interval (<30 K) indicate that the replacement of Cu by B would result in the significant narrowing of supercooled liquid region and enhance the GFA of Mg-Cu-Y amorphous alloys. When further increasing the boron content x to 5 at%, the single endothermic peak and the narrow melting interval demonstrate that $Mg_{65}Cu_{20}Y_{10}B_5$ alloy may be very near to the quaternary eutectic composition.

4.6.2 Kissinger plots for non-isothermal analyses

In non-isothermal analyses, the dependency of crystallization temperature on heating rate can be used to estimate the activation energy of crystallization by means of the Kissinger peak shift method. Figures 4.19 to 4.20 show the Kissinger plots of ln(ϕ/T_x) against reciprocal T_x taken from the dependence of crystallization temperature on various heating rates (ϕ = 10, 20, 30 K/min) in the DSC curves (T_x is referred to the onset crystallization temperature). The activation energy of the first crystallization for the $Mg_{65}Cu_{25}Y_{10}$ amorphous alloy derived from the slop of Kissinger plot is 138 kJ/mol, as shown in Fig. 4.19 (a). As a comparison, the activation energy values for $Mg_{65}Cu_{25-x}Y_{10}B_x$ (x = 3, 5, 10) amorphous ribbons evaluated by the slope of this Kissinger plot, as shown in Figs. 4.19 to 4.20, are 156, 149 and 150 kJ/mol, respectively. These values are about 10% higher than the parent alloy. It indicates that the substitution of Cu by B improves the thermal stability for the Mg-based amorphous alloys. Furthermore, some researchers use the shift of crystallization temperature T_p (T_p is referred to peak temperature of the crystallization) to yield the activation energy of crystallization (E_{xp}) by using the Kissinger equation. Pryds et al. also used this method to determine the activation energy of crystallization for $Mg_{60}Cu_{30}Y_{10}$ [53] and Mg-Cu-Y-Al [54] amorphous alloys. The activation energy of the first crystallization peak is approximately 1.6 eV ($\approx$154 kJ/mol). It is interesting to note that the activation energy for the first phase transition (Mg_2Cu) in Mg-based multicomponent alloys is the same as found by Sommer et al. [55] for the binary amorphous alloys $Mg_{78}Cu_{22}$ alloy which has E_{xp} =1.58 eV ($\approx$152 kJ/mol). It implies that the process of the primary crystallization is similar in the binary, ternary and quaternary Mg-based amorphous alloys.

4.6.3 Modified Kissinger plots for non-isothermal analyses

The non-isothermal DSC thermogram also has been used to ascertain the mechanism and kinetics of first crystallization by the method of modified Kissinger equation. The fraction of crystallization could be calculated by integrating the area under the exothermal peak from the non-isothermal DSC curves, namely,

$$X = \frac{\int_{\mathrm{Tx\ onst}}^{T} H(T)dT}{\int_{\mathrm{Tx\ onset}}^{\mathrm{Tx\ end}} H(T)dT} \quad , \qquad (24)$$

where X is the volume fraction of crystallization, H(T) is the heat as function of temperature. For the evaluation of the parameter n, ln[-ln(1-X)] is plotted as a function of lnϕ. Figures 4.21 and Fig. 4.22 show the variation of n which is temperature dependence. Theoretically, n should not exceed 4 (i.e., the bulk nucleation and three dimensional growth). In the early crystallization stage, because nuclei are in random distribution, the n values extracted from the plots for the initial transient stage will exceed 4. The similar high values of n (n = 6) also has been reported for a ternary chalcogenide glass [56]. Since the n value is much larger than 1, bulk nucleation should be dominant in the early stage of phase transformation. With increasing temperature, the n value decreases to 1 and surface nucleation dominates the later stage of transformation until only growth process dominates.

Figures 4.23 to 4.26 are the plots of ln[-ln(1-X)] against the 1/T for several heating rates. From the slope, -1.052mQ/R can be obtained. Since no particular heat treatment was given to nucleate the samples before thermal analysis, the dimensionality of growth parameter m is taken to be equal to (n - 1) in the early crystallization stage and m is equal to n when a large number of nuclei exist in the final crystallization stage. From the view of the slope, it is apparent that the early crystallization stage has a nearly linear and steep slope (means higher activation energy for crystallization) and then suddenly decreases when pass through a break in the slope.

This break in the slope above a specific volume fraction can be observed for each heating rate. From Lin and Shen's research [57] infer that the slope breaks on the ln[-ln(1-X)] vs. 1/T plot is the saturation of nucleation sites. Below the break temperature, the activation energy includes the nucleation activation energy and growth activation energy. On the contrary, due to the saturation of nucleation, only the growth activation energy remains above the break temperature. This inference is also consistent with the slope observed.

Furthermore, it is noted that the slope breaks at nearly the same transformed volume fraction $X \approx 0.6$ ($\ln[-\ln(1-X)] \approx 0$) for all the Mg-based amorphous alloys in Figs. 4.23 to 4.25. It means the nucleation behavior is similar in all Mg-based amorphous alloys.

4.6.4 Isothermal analyses and kinetics

The samples of the Mg-based amorphous alloys are annealed isothermally at 433, 435, 438, and 440 K between T_g and T_x. Figures 4.27 and 4.28 show the results of the isothermal calorimetry for the $Mg_{65}Cu_{25}Y_{10}$ and $Mg_{65}Cu_{22}Y_{10}B_3$ amorphous alloys. It cannot be considered as one primary crystallization for the $Mg_{65}Cu_{22}Y_{10}B_3$ alloy, where the multi-exothermic peaks are observed. In order to follow the JMA assumption, the multi-exothermic reaction is separated by using the PeakFit software. As shown in Figs. 4.29 to 4-30, the modified exothermic peaks all exhibit a symmetric shape.

Figure 4.31 and Fig. 4.32 show the plot that the degree of transformation as a function of time for different Mg-based amorphous alloys. With increasing annealing temperature, the incubation time and the time for a complete crystallization would both decrease. The incubation time at the annealing temperature of 433, 435, 438, and 440 K for the $Mg_{65}Cu_{25}Y_{10}$ amorphous alloy are 1420, 810, 580 and 373 s and for the $Mg_{65}Cu_{22}Y_{10}B_3$ amorphous alloys are 1568, 1031, 778 and 595 s, respectively. the latter alloy always exhibit longer incubation time as compared with the parent alloy.

Furthermore, for the evaluation of the Avrami exponent n, ln[-ln(1-X)] is plotted versus ln(t) for different annealing temperatures. Figures 4.33 to 4.34 reveal that the Avrami exponent n of $Mg_{65}Cu_{25}Y_{10}$ and $Mg_{65}Cu_{22}Y_{10}B_3$ amorphous alloys are temperature dependent during the isothermal crystallization process. Form the slopes of the straight lines, the average value of n for $Mg_{65}Cu_{25}Y_{10}$ is about 3.5. It means that the crystallization is mainly controlled by three dimensional nuclei with constant growth rate until the whole amorphous phase is completely crystallized. In the $Mg_{65}Cu_{22}Y_{10}B_3$ amorphous alloy, the average value of n is also about 3.2. The results indicate that the Mg-based amorphous alloys exhibit similar crystallization behavior .

In isothermal analyses, the activation energy can also be evaluated by the isothermal curves of crystallized volume fraction versus annealing time at different temperatures. This is carried out by using the Arrhenius equation, $t = t_o \exp(Q/RT)$. For each annealing temperature, the time to reach the integer multiple of 10% crystallization is selected and the plots of lnt versus1/T for Mg-based amorphous alloys are made, as shown in Figs. 4.35 and 4.36. From the slopes, the average activation energies determined for the first crystalline phase (Mg_2Cu) of the $Mg_{65}Cu_{25}Y_{10}$ and $Mg_{65}Cu_{22}Y_{10}B_3$ amorphous alloys are 156 and 210 kJ/mol, respectively. This indicates that the boron can increase the activation energy of crystallization for the $Mg_{65}Cu_{25}Y_{10}$ based alloy and results in the improvement of the thermal stability against crystallization. The activation energy of the second crystalline phase for the

$Mg_{65}Cu_{22}Y_{10}B_3$ which are also determined by the Arrhenius equation are 200 kJ/mol, as shown in the Fig. 4.37.

4.7 TEM observations

TEM micrograph is taken to understand the local structure of the as-melt-spun $Mg_{65}Cu_{22}Y_{10}B_3$ amorphous alloy, and the result is shown in Fig. 4.38. For the majority case, no crystallity is visible in the TEM micrograph, and the corresponding diffraction pattern always shows a typical halo for an amorphous phase, in good agreement with the XRD results. Occasionally, few small yttrium oxides are observed in the amorphous matrix, as shown in Fig. 4.39.

Figures 4.40 to 4.45 show the crystallization products of the $Mg_{65}Cu_{22}Y_{10}B_3$ amorphous alloy while heated to 670 K at a heating rate of 20 K/min in an Ar atmosphere and held for 300s followed by cooling to room temperature. The nanocrystalline phases measuring from 200 to 400 nm are observed.

Chapter 5

Discussions

5.1 The effect of the boron element

According the empirical BMG formation criteria, the bulk glass formation should satisfy: (1) the multicomponent alloy systems consisting of more than three elements; (2) large differences in atomic size between the constituent elements; (3) negative heat of mixing among the major elements; and (4) alloy compositions close to the deep eutectic point. In accordance with these rules for achieving high GFA, one of the important factors for the formation of the amorphous phase is related to a large difference in atomic size among the main constituents. Therefore, the interstitial atom boron, a suitable candidate for this research, may tighten the alloy structure and then stabilize the amorphous alloy against crystallization. On the other hand, due to the lightweight of the Mg-based alloys, it is widely used on the industry. By the addition of B, it will not degrade the density advantage of the $Mg_{65}Cu_{25}Y_{10}$ amorphous alloy (Table 4.1) and will show no harm on the GFA.

It can also be rationalized the different crystallization behavior by the effect of atomic size, heat mixing, and the bond parameter. The values of Δx and δ for the Mg-Cu-Y-B alloys are shown in Table 5.1. Because boron has a small atomic size ratio and a higher electronegativity value among the main constituents, it is reasonable that the atomic size parameter and electronegativity difference would both increase with increasing B addition. Figure 5.1 shows that the $Mg_{65}Cu_{25-x}Y_{10}B_x$ alloys indeed have higher products of Δx and δ than the $Mg_{65}Cu_{25}Y_{10-x}B_x$ alloys. It is demonstrated from the DSC experimental results that the B substitution for Cu really provides better GFA. But an opposite trend is observed for the B substitution for Y; the higher value of Δx and δ in $Mg_{65}Cu_{25}Y_{10-x}B_x$ is accompanied by a lower GFA in DSC results. Therefore, the difference of crystalline phase and the mixing enthalpy value among the elements need to be considered in Mg-Cu-Y-B systems. The zero value of mixing enthalpy between Cu and B may account for the worse GFA in the $Mg_{65}Cu_{25}Y_{10-x}B_x$ systems.

Nevertheless, even with higher $\Delta x \cdot \delta$ values for the $Mg_{65}Cu_{25-x}Y_{10}B_x$ alloys. GFA for the alloys with x = 10 would again drop, since the abundant B content would promote B-containing (e.g. MgB_4) crystallization. It seems that there is an optimum B content to result in the highest GFA.

5.2 XRD analyses

Figures 5.2 and 5.3 show the overall crystallization of $Mg_{65}Cu_{22}Y_{10}B_3$ and $Mg_{65}Cu_{15}Y_{10}B_{10}$ amorphous alloys. For the $Mg_{65}Cu_{22}Y_{10}B_3$ alloy, Mg_2Cu phase forms in the amorphous matrix, then the amorphous phase are fully crystallized. For the $Mg_{65}Cu_{15}Y_{10}B_{10}$ amorphous alloy, the MgB_4 phase does form first. It implies that the higher boron content would retrain the growth of Mg_2Cu by growing another phase which is less stable than Mg_2Cu at high temperatures.

Furthermore, a close inspection of the XRD positions of the Mg_2Cu peaks (orthorhombic structure) would show a slight shift from the simulated angles. This discrepancy may be due to the partial dissolution of yttrium and boron in the Mg_2Cu phase, or the possibilities that the Mg_2Cu phase is not of the exact stoichiometric composition. It can be identified by the TEM EDS analysis.

5.3 Thermodynamics and kinetics analyses

From the non-isothermal analyses, the addition of boron really enhances the thermal stability in the Mg-based alloys. In the $Mg_{65}Cu_{25-x}Y_{10}B_x$ alloy systems, all samples exhibit a sharp exothermic peak during continuous DSC heating. With increasing boron content from 0 to 3 at%, the ΔT_x can increase from 58 to 66 K and can further decrease the melting point. The γ value for $Mg_{65}Cu_{25-x}Y_{10}B_x$ (x = 0, 3, 5) also increase from 0.40 to 0.42 and 0.41, respectively, as shown in Table 5.2. In contrast, the multi-exothermic peaks of the $Mg_{65}Cu_{25}Y_{10-x}B_x$ alloys system would appear along with the primary crystallization and ΔT_x would decrease with increasing B content.

The Kissinger plots have been shown in Figs. 4.19 and 4.20, the activation energy evaluated by the onset crystallization temperature (or the very initial stage) is lower than that by the peak temperature. Because of the different stages of crystallization, it causes the difference in activation energy. Normally, the derived activation energy by the onset crystallization temperature is considered to be the energy barrier for nucleation, and the derived activation energy by the peak temperature is though to involve both nucleation and growth of crystallization. Hence, the later was extracted to be a higher value of activation energy. Activation energies in the range of 160-240 kJ/mol for crystallization of Mg-based amorphous alloys were also reported [58].

Besides, the activation energy for any specific volume fraction of crystallization can also be obtained by the non-isothermal Kissinger equation. For instance, the volume fraction of transformed of $Mg_{65}Cu_{25}Y_{10}$ for the peak temperatures at heating rate 10, 20 and 30 K/min are 58%, 50% and 40%, respectively. It does not have too much meaning on their Kissinger slope. But according to the peak shift of the linear heating DSC curves for the same volume fraction of transformed crystallization at different heating rates, the activation energy for any specific volume fraction of crystallization also can be obtained by the Kissinger slope. The Kissinger plots are shown in Figs. 5.4 to 5.6. It is apparent that the activation energy is almost constant below 60% transformed volume, then drop to small value when above 60% transformed volume. This phenomenon is consistent with the description for the modified Kissinger plots. The nucleation saturation sites are observed nearly the 63% transformed volume at several heating rates. It means that the growth mechanism dominates the later crystallization stage due to the absence of nucleation. Hence, the activation energy will decrease until the amorphous phase is completely crystallized.

In isothermal analyses, it is found that the value of Avrami exponent n may be influenced by the determination procedures, such as the calibration of baselines in the isothermal DSC curve, the incubation time, and the degree of crystallization. Furthermore, the n value is not an fixed integral. In comparison with the exponent n of $Mg_{65}Cu_{25}Y_{10}$ and $Mg_{65}Cu_{22}Y_{10}B_3$, the average values of n are all about 3. This result implies that two alloys exhibit similar crystallization process.

For the activation energy evaluated by the isothermal analyses, the average activation energy of the $Mg_{65}Cu_{25}Y_{10}$ and $Mg_{65}Cu_{22}Y_{10}B_3$ amorphous alloys for the primary crystallization of Mg_2Cu are 150 and 210 kJ/mol, respectively. Because Mg has the low activation energy for diffusion at low temperatures, it postulated that the growth of the Mg_2Cu phase is controller by the Mg diffusion.

As for the $Mg_{65}Cu_{22}Y_{10}B_3$ amorphous alloy, the growth of Mg_2Cu phase during isothermal annealing involves more than Mg diffusion. Figures 5.2 and 5.3 show the overall crystallization of the $Mg_{65}Cu_{25}Y_{10}$ and the $Mg_{65}Cu_{22}Y_{10}B_3$ amorphous alloys. Due to the addition of boron, the first peak is not Mg_2Cu phase until heating to higher temperatures, it means that boron can restrain the growth of Mg_2Cu. The $Mg_{65}Cu_{22}Y_{10}B_3$ amorphous alloy has the higher activation energy (210 kJ/mol) for crystallization, suggesting that the B diffusion away and the Cu diffusion toward the Mg_2Cu nuclei are also important.

Chapter 6

Conclusions

(1) Using the melting spinning method, the $Mg_{65}Cu_{25}Y_{10}$, $Mg_{65}Cu_{25-x}Y_{10}B_x$ (x=0 ~ 5), and $Mg_{65}Cu_{25}Y_{10-x}B_x$ (x=0 ~ 10) are all amorphous alloys except for the $Mg_{65}Cu_{25}Y_5B_5$ and $Mg_{65}Cu_{25}B_{10}$ alloys which have the crystalline phases of Mg_2Cu and MgB.

(2) The addition of B would increase the hardness from 220 to 327 H_v for $Mg_{65}Cu_{25-x}Y_{10}B_x$ (x=0 ~ 5), and $Mg_{65}Cu_{25}Y_{10-x}B_x$ (x=0 ~ 10) amorphous alloys.

(3) The density of the modified MgCuY amorphous alloys increases owing to the filling of free volume by the small B atoms. Nevertheless, the density value are all still below 4 kg/m^3 considered as light weight amorphous alloys.

(4) In the $Mg_{65}Cu_{25}Y_{10}$ amorphous alloy, the replacement of Cu by B can further enhance the thermal stability and glass forming ability. The supercooled temperature range ΔT and the glass forming γ index is increased to 66 K and 0.420, respectively.

(5) The activation energy of the $Mg_{65}Cu_{25}Y_{10}$ amorphous alloy for crystallization determined by the non-isothermal Kissinger method is 138 kJ/mol. With increasing B content, it can be promoted to a high energy barrier against crystallization, and $Mg_{65}Cu_{22}Y_{10}B_3$ has a higher value of 156 kJ/mol.

(6) The modified Kissinger plot for the non-isothermal analyses can characterize the nucleation behavior and growth mechanism form the slope. It can also observe the site saturation at a given transformed volume fraction.

(7) The activation energy values of the $Mg_{65}Cu_{25}Y_{10}$ and $Mg_{65}Cu_{22}Y_{10}B_3$ amorphous alloys for crystallization determined from the isothermal analysis are 150 and 200 kJ/mol, respectively. Due to the addition of boron, it can restrain the growth of Mg_2Cu and increase the activation energy.

(8) From the n exponent extracted from the isothermal JMA equation, it implies that the Mg-based amorphous alloys exhibit the similar crystallization processes.

(9) The crystallization products of the $Mg_{65}Cu_{22}Y_{10}B_3$ amorphous alloy measuring from 200 to 400 nm are observed in TEM. The Mg_2Cu, solid solution and yttrium rich compound are traced.

References

[1] 吳學陞，工業材料, 149 (1999), pp. 154-165.

[2] A. Inoue, K. Ohtera, K. Kita and T. Masumoto, Jpn. J. Appl. Phys., 27 (1988) L.2248.

[3] A. Calka, M. Madhava, D. E. Polk, B. C. Giessen and J. V. Sande, Scripta. Metall., 11 (1970), p. 65.

[4] F. Sommer, G. Bucher and B. Fredel, J. Phys. C, 41 (1980), p. 563.

[5] A. Inoue and T. Masumoto, Mater. Sci. Eng. A, 133 (1991), p. 6.

[6] A. Inoue, A. Kato, T. Zhang, S. G. Kim and T. Masumoto, Mater. Trans. JIM, 32 (1991), pp. 609-616.

[7] A. Inoue, T. Nakamura, N. Nishiyama and T. Masumoto, Mater. Trans. JIM, 33 (1992), pp. 937-945.

[8] A. Inoue, T. Zhang and T. Masumoto, J. Non-Cryst. Solids, 156-158 (1993), p. 473.

[9] A. Inoue, Acta Mater., 48 (2000), pp. 279-306.

[10] A. Inoue, T. Zhang, M. W. Chen and T. Sakurai, J. Mater. Res., 15 (2000), p. 2195.

[11] E. S. Park, H. G. Kang, W. T. Kim and D.H. Kim., J. Non-Cryst. Solids, 279 (2001), p. 154.

[12] H. Men, W. T. Kim and D. H. Kim., J. Non-Cryst. Solids, 337 (2004), p. 29.

[13] H. Men, Z. Q. Hu and J. Xu, Scripta Mater., 46 (2002), pp. 699-703.

[14] K. Amiya and A. Inoue, Mater. Trans. JIM, 41 (2000), pp. 1460-1462.

[15] W. Klement, R. H. Willens and P. Duwez: Nature, 187 (1960), p. 869.

[16] H. S. Chen, Mater. Sci. Eng., 25 (1976), p. 59.

[17] A. Inoue, T. Zhang and T. Masumoto, Mater. Trans. JIM, 30 (1989), pp. 965-972.

[18] A. Inoue, N. Nishiyama and H. M. Kimura, Mater. Trans. JIM, 38 (1997), pp. 179-183.

[19] Y. H. Kim, A. Inoue and T. Masumoto, Mater. Trans. JIM, 31 (1990), pp. 747-749.

[20] R. W. Cahn, P. Hassen and E. J. Kramer (ed.): Materials Science and Technology, Vol.9,

New York, USA, 1991.

[21] H. S. Chen, Rep. Prog. Phys., (1980), p.353.

[22] H. W. Kui and D. Turnbull, Appl. Phys. Lett., 45 (1984), p. 615.

[23] A. Peker and W. L. Johnson, Appl. Phys. Lett., 63 (1993), p. 25.

[24] A. Inoue, N. Nishiyama, K. Amiya, T. Zhang and T. Masumoto, Mater. Lett., 19 (1994), p. 131.

[25] A. Inoue and T. Masumoto, Mater. Sci. Eng. A, 173 (1993), pp. 1-8.

[26] J. Q. Guo, K. Kita and K. Ohtera, Mater. Lett., 24 (1995), pp. 127-132.

[27] D. Turbbull and J. C. Fisher, J. Chem. Phys., 17 (1949), p. 71.

[28] Z. P.Lu, H. Tan, Y. Li and S. C. Ng, Scripta Mater., 42 (2000), pp. 667-673.

[29] A. Inoue, W. Zhang, T. Zhang and K. Kurosaka, Acta Mater., 49 (2001), pp. 2645-2652.

[30] T. A. Waniuk, J. Schroers and W. L. Johnson, Appl. Phys. Lett., 78 (2001), p. 1213.

[31] S. V. Madge and A. L. Greer, Mater. Sci. Eng., A 375 (2004), p. 759.

[32] Z. P. Lu and C. T. Liu, Acta Mater., 50 (2002), p. 3501.

[33] A. Inoue, Mater. Trans. JIM, 36 (1995), pp. 866-875.

[34] A. Inoue, T. Zhang and A. Takeuchi, Mater. Sci. Forum., 269-272 (1998), p. 855.

[35] A. Inoue, A. Takeuchi and T. Zhang, Metall. Mater. Trans., A29 (1998), p. 1779.

[36] D. Turnbull, Contemp. Phys., 10 (1969), p. 473.

[37] C. H. Shek, Y. M. Wang and C. Dong, Mater. Sci. Eng., A 291 (2000), p. 78.

[38] S. Fang, X. Xiao, L. Xia, W. Li and Y. Dong, J. Non-Cryst. Solids, 321 (2003), p. 120.

[39] Y. Kawamura, T. Shibata, A. Inoue and T. Masumoto, Appl. Phys. Lett., 69 (1996), p. 1208.

[40] A. Inoue, Mater. Sci. Eng., A 267 (1999), p. 171.

[41] A. Inoue and T. Masumoto, J. Mater. Sci., 15 (1980), p. 1993.

[42] T. G. Park, S. Yi and D. H. Kim, Scripta Mater., 43 (2000), p. 1093.

[43] S. Pang, T. Zhang, K. Asami and A. Inoue, Mater. Trans., 42 (2001), p. 376.

[44] Y. Kawamura and Y. Ohno, Scripta Mater., 45 (2001), p. 127.

[45] H. E. Kissinger, Arial. Chem., 29 (1957), pp. 1702-1706.

[46] J. Vazquez, R. L. Lopez-Alemany, P. Villares and R. Jimenez-Garay, Thermochim. Acta Mater., 157 (2000), p. 181.

[47] T. Ozawa, Polymer, 12 (1971), pp. 150-158.

[48] K. Matusita and S. Sakka, Phys. Chem. Glasses, 20 (1979), pp. 81.

[49] M. Avrami, J. Chem. Phys., 7 (1939), pp. 1103-1112.

[50] M. Avrami, J. Chem. Phys., 8 (1940), pp. 212-224.

[51] M. Avrami, J. Chem. Phys., 7 (1941), pp. 177-184.

[52] J.W. Christian (Ed.), The Theory of Transformation in Metals and Alloys, Pergamon Press, London, 1965.

[53] N. H. Pryds, M. Eldrup and A. S. Pedersen, Proceedings and 22nd Riso international symposium on materials science: Science of metastable and nanocrystalline alloys – Structure, properties and modeling, (2001), pp. 377-382.

[54] S. Linderoth, N. H. Pryds, M. Ohnuma, A. S. Pedersen, M. Eldrup, N. Nishiyama and A. Inoue, Mater. Sci. Eng. A, 304-306 (2001), p. 656-659.

[55] F. Sommer, G. Bucher and B. Predel, J. de Phys., 41 (1980), p. 563.

[56] S. Mahadevan, A. Giridhar and A. K. Singh, J. Non-cryst. Solids, 88 (1986), p. 11.

[57] C.C. Llin and P. Shen, J. Solid state Chem., 112 (1994), pp. 387-391.

[58] S. Orimo, K. Ikeda, H. Fujii, K. Yamamoto, J. Alloys Comp., 260 (1997), p. 143.

Table 1.1 Application filed for bulk metallic glasses [9].

Properties	Application Field
High strength	Machinery structural materials
High hardness	Cutting materials
High fracture toughness	Die materials
High impact fracture energy	Tool materials
High fatigue strength	Bonding materials
High elastic energy	Sporting goods materials
High corrosion resistance	Corrosion resistance materials
High wear resistance	Writing appliance materials
High reflection ratio	Optical precision materials
High hydrogen storage	Hydrogen storage materials
Good soft magnetism	High magnetostrictive materials
High frequency permeability	Electrode materials
Efficient electrode	Composite materials
High viscous flowability	Acoustic absorption materials
Self-sharping property	Penetrator
High wear resistance and manufacturability	Medical device materials

Table 2.1 The classification of amorphous alloy systems [9].

I	ETM(or Ln) + Al + LTM	Zr-Al-Ni、Zr-Al-Cu、Zr-Al-Ni-Cu、Zr-Ti-Al-Ni-Cu、Zr-Nb-Al-Ni-Ln、Zr-Ga-Ni
		Ln-Al-Ni、Ln-Al-Cu、Ln-Al-Ni-Cu、Ln-Ga-Ni、Ln-Ga-Cu
II	LTM + ETM + Metalloid	Fe-Zr-B、Fe-Hf-b、Fe-Zr-Hf-B、Fe-Co-Ln-B、Co-Zr-Nb-B
III	LTM(Fe) + Al or Ga + Metalloid	Fe-(Al,Ga)-Metalloid
IV	Mg + Ln +LTM	Mg-Ln-Ni、Mg-Ln-Cu
	TM(Zr or Ti) + Be + LTM	Zr-Ti-Be-Ni-Cu
V	LTM + Metalloid	Pd-Ni-P、Pd-Cu-Ni-P、Pt-Ni-p

ETM = IVB~VIB Group Transition Metal

LTM = VIIB~VIIIB Group Transition Metal

Table 2.2 The annual of bulk amorphous alloy was first published [9].

I. Nonferrous metal base		II. Ferrous metal base	
Constituents	Year	Constituents	Year
Mg-Ln-M	1988	Fe-(Al, Ga)-(P, C, B, Si, Ge)	1995
Ln-Al-TM	1989	Fe-(Nb, Mo)-(Al, Ga)-(P, B, Si)	1995
Ln-Ga-TM	1989	Co-(Al, Ga)-(P, B, Si)	1996
Zr-Al-TM	1990	Fe-(Zr, Hf, Nb)-B	1996
Zr-Ti-Al-TM	1990	Co-Fe-(Zr, Hf, Nb)-B	1996
Ti-Zr-TM	1993	Ni-(Zr, Hf, Nb)-(Cr, Mo)-B	1996
Zr-Ti-TM-Be	1993	Fe-Co-Ln-B	1998
Zr-(Nb, Pd)-Al-TM	1995	Ni-Ti-P	1999
Pd-Cu-Ni-P	1996	Ni-(Nb, Cr, Mo)-(P, B)	1999
Pd-Ni-Fe-P	1996	Fe-Mn-Mo-Cr-C-B	2002
Pd-Cu-B-Si	1997		
Ti-Ni-Cu-Sn	1998		
Zr-Nb-Cu-Fe-Be	2000		

Ln = Lanthanide Metal, M = Ni, Cu, Zn

TM = VIB~VIIIB Group Transition Metal

Table 2.3 Summary of △T_x, T_{rg}, γ, critical cooling rate Rc and critical section thickness Z_c for typical bulk amorphous alloys [32].

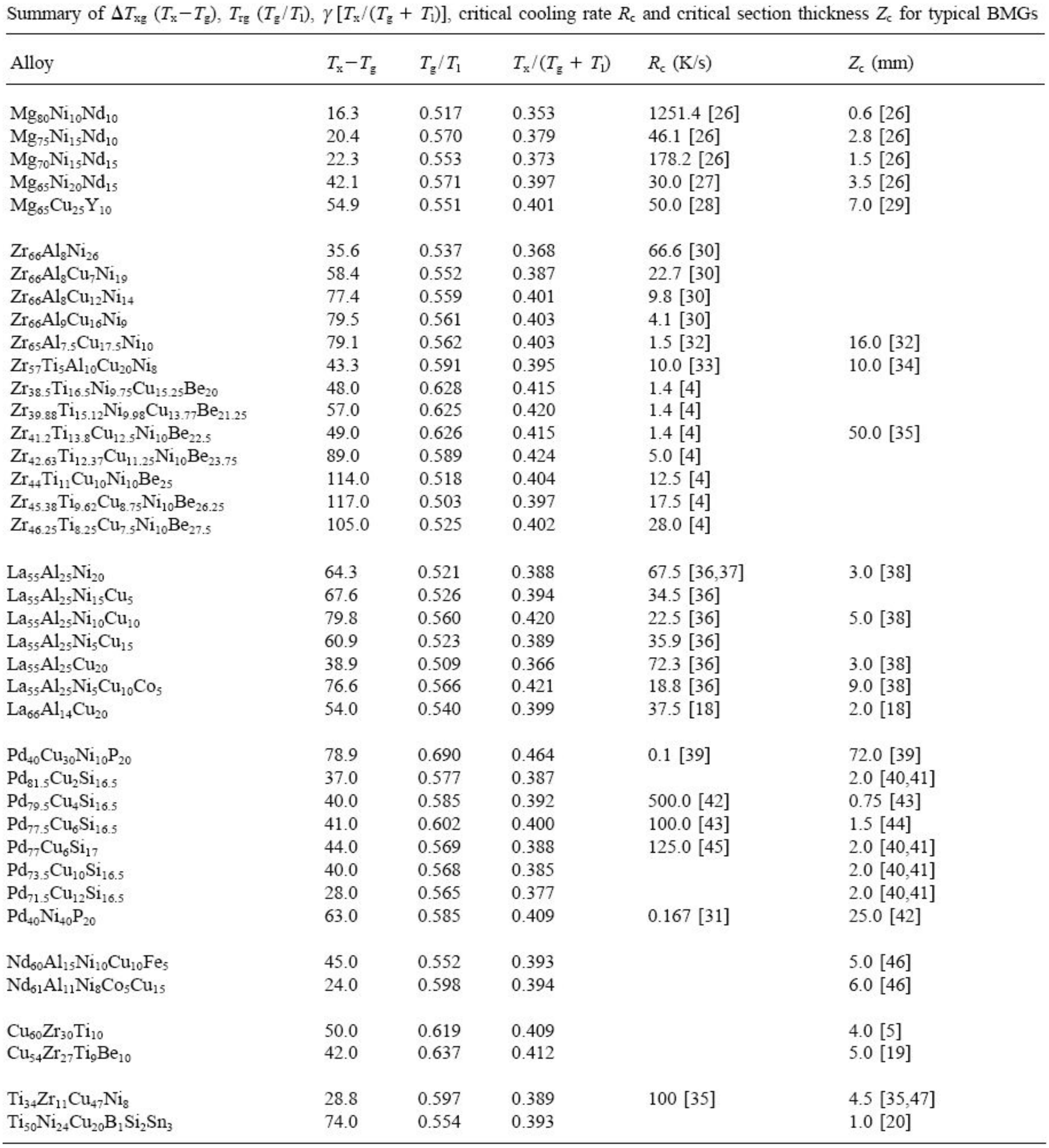

Summary of ΔT_{xg} ($T_x - T_g$), T_{rg} (T_g/T_l), γ [$T_x/(T_g + T_l)$], critical cooling rate R_c and critical section thickness Z_c for typical BMGs

Alloy	$T_x - T_g$	T_g/T_l	$T_x/(T_g + T_l)$	R_c (K/s)	Z_c (mm)
$Mg_{80}Ni_{10}Nd_{10}$	16.3	0.517	0.353	1251.4 [26]	0.6 [26]
$Mg_{75}Ni_{15}Nd_{10}$	20.4	0.570	0.379	46.1 [26]	2.8 [26]
$Mg_{70}Ni_{15}Nd_{15}$	22.3	0.553	0.373	178.2 [26]	1.5 [26]
$Mg_{65}Ni_{20}Nd_{15}$	42.1	0.571	0.397	30.0 [27]	3.5 [26]
$Mg_{65}Cu_{25}Y_{10}$	54.9	0.551	0.401	50.0 [28]	7.0 [29]
$Zr_{66}Al_8Ni_{26}$	35.6	0.537	0.368	66.6 [30]	
$Zr_{66}Al_8Cu_7Ni_{19}$	58.4	0.552	0.387	22.7 [30]	
$Zr_{66}Al_8Cu_{12}Ni_{14}$	77.4	0.559	0.401	9.8 [30]	
$Zr_{66}Al_9Cu_{16}Ni_9$	79.5	0.561	0.403	4.1 [30]	
$Zr_{65}Al_{7.5}Cu_{17.5}Ni_{10}$	79.1	0.562	0.403	1.5 [32]	16.0 [32]
$Zr_{57}Ti_5Al_{10}Cu_{20}Ni_8$	43.3	0.591	0.395	10.0 [33]	10.0 [34]
$Zr_{38.5}Ti_{16.5}Ni_{9.75}Cu_{15.25}Be_{20}$	48.0	0.628	0.415	1.4 [4]	
$Zr_{39.88}Ti_{15.12}Ni_{9.98}Cu_{13.77}Be_{21.25}$	57.0	0.625	0.420	1.4 [4]	
$Zr_{41.2}Ti_{13.8}Cu_{12.5}Ni_{10}Be_{22.5}$	49.0	0.626	0.415	1.4 [4]	50.0 [35]
$Zr_{42.63}Ti_{12.37}Cu_{11.25}Ni_{10}Be_{23.75}$	89.0	0.589	0.424	5.0 [4]	
$Zr_{44}Ti_{11}Cu_{10}Ni_{10}Be_{25}$	114.0	0.518	0.404	12.5 [4]	
$Zr_{45.38}Ti_{9.62}Cu_{8.75}Ni_{10}Be_{26.25}$	117.0	0.503	0.397	17.5 [4]	
$Zr_{46.25}Ti_{8.25}Cu_{7.5}Ni_{10}Be_{27.5}$	105.0	0.525	0.402	28.0 [4]	
$La_{55}Al_{25}Ni_{20}$	64.3	0.521	0.388	67.5 [36,37]	3.0 [38]
$La_{55}Al_{25}Ni_{15}Cu_5$	67.6	0.526	0.394	34.5 [36]	
$La_{55}Al_{25}Ni_{10}Cu_{10}$	79.8	0.560	0.420	22.5 [36]	5.0 [38]
$La_{55}Al_{25}Ni_5Cu_{15}$	60.9	0.523	0.389	35.9 [36]	
$La_{55}Al_{25}Cu_{20}$	38.9	0.509	0.366	72.3 [36]	3.0 [38]
$La_{55}Al_{25}Ni_5Cu_{10}Co_5$	76.6	0.566	0.421	18.8 [36]	9.0 [38]
$La_{66}Al_{14}Cu_{20}$	54.0	0.540	0.399	37.5 [18]	2.0 [18]
$Pd_{40}Cu_{30}Ni_{10}P_{20}$	78.9	0.690	0.464	0.1 [39]	72.0 [39]
$Pd_{81.5}Cu_2Si_{16.5}$	37.0	0.577	0.387		2.0 [40,41]
$Pd_{79.5}Cu_4Si_{16.5}$	40.0	0.585	0.392	500.0 [42]	0.75 [43]
$Pd_{77.5}Cu_6Si_{16.5}$	41.0	0.602	0.400	100.0 [43]	1.5 [44]
$Pd_{77}Cu_6Si_{17}$	44.0	0.569	0.388	125.0 [45]	2.0 [40,41]
$Pd_{73.5}Cu_{10}Si_{16.5}$	40.0	0.568	0.385		2.0 [40,41]
$Pd_{71.5}Cu_{12}Si_{16.5}$	28.0	0.565	0.377		2.0 [40,41]
$Pd_{40}Ni_{40}P_{20}$	63.0	0.585	0.409	0.167 [31]	25.0 [42]
$Nd_{60}Al_{15}Ni_{10}Cu_{10}Fe_5$	45.0	0.552	0.393		5.0 [46]
$Nd_{61}Al_{11}Ni_8Co_5Cu_{15}$	24.0	0.598	0.394		6.0 [46]
$Cu_{60}Zr_{30}Ti_{10}$	50.0	0.619	0.409		4.0 [5]
$Cu_{54}Zr_{27}Ti_9Be_{10}$	42.0	0.637	0.412		5.0 [19]
$Ti_{34}Zr_{11}Cu_{47}Ni_8$	28.8	0.597	0.389	100 [35]	4.5 [35,47]
$Ti_{50}Ni_{24}Cu_{20}B_1Si_2Sn_3$	74.0	0.554	0.393		1.0 [20]

Table 2.4 The exponent n for the JMA equation for different kinds of crystallization mechanisms [48-51].

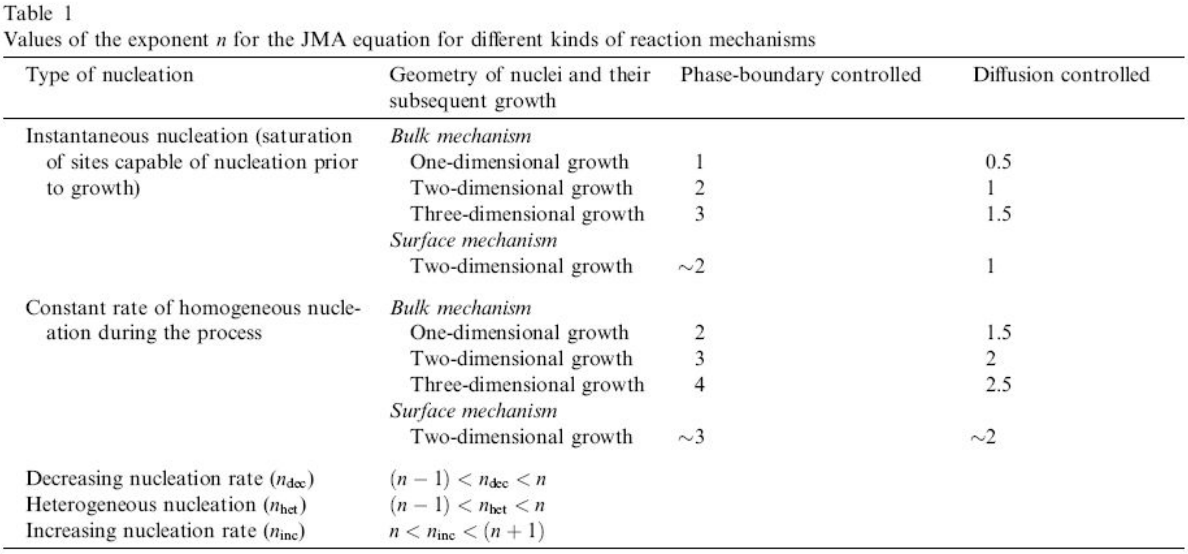

Table 1
Values of the exponent n for the JMA equation for different kinds of reaction mechanisms

Type of nucleation	Geometry of nuclei and their subsequent growth	Phase-boundary controlled	Diffusion controlled
Instantaneous nucleation (saturation of sites capable of nucleation prior to growth)	*Bulk mechanism*		
	One-dimensional growth	1	0.5
	Two-dimensional growth	2	1
	Three-dimensional growth	3	1.5
	Surface mechanism		
	Two-dimensional growth	~2	1
Constant rate of homogeneous nucleation during the process	*Bulk mechanism*		
	One-dimensional growth	2	1.5
	Two-dimensional growth	3	2
	Three-dimensional growth	4	2.5
	Surface mechanism		
	Two-dimensional growth	~3	~2
Decreasing nucleation rate (n_{dec})	$(n-1) < n_{dec} < n$		
Heterogeneous nucleation (n_{het})	$(n-1) < n_{het} < n$		
Increasing nucleation rate (n_{inc})	$n < n_{inc} < (n+1)$		

Table 3.1 The alloy systems selected in this study.

	Mg		**Cu**		**Y**		**B**	
	at%	wt%	at%	wt%	at%	wt%	at%	wt%
$Mg_{65}Cu_{25}Y_{10}$	65	9.74	25	9.78	10	5.48	0	0
$Mg_{65}Cu_{25}Y_9B_1$	65	9.93	25	9.98	9	5.02	1	0.07
$Mg_{65}Cu_{25}Y_7B_3$	65	10.33	25	10.38	7	4.07	3	0.22
$Mg_{65}Cu_{25}Y_5B_5$	65	10.77	25	10.83	5	3.03	5	0.37
$Mg_{65}Cu_{25}B_{10}$	65	12.06	25	12.12	0	0	10	0.82
$Mg_{65}Cu_{24}Y_{10}B_1$	65	9.86	24	9.52	10	5.55	1	0.07
$Mg_{65}Cu_{22}Y_{10}B_3$	65	10.13	22	8.96	10	5.70	3	0.21
$Mg_{65}Cu_{20}Y_{10}B_5$	65	10.41	20	8.37	10	5.86	5	0.36
$Mg_{65}Cu_{15}Y_{10}B_{10}$	65	11.19	15	6.75	10	6.30	10	0.76

Table 4.1 Summary of the density for various alloy combinations

Composition	Theoretical density Mg/m^3	True density Mg/m^3
$Mg_{65}Cu_{25}Y_{10}$	3.82	3.09
$Mg_{65}Cu_{24}Y_{10}B_1$	3.82	--
$Mg_{65}Cu_{22}Y_{10}B_3$	3.62	3.46
$Mg_{65}Cu_{20}Y_{10}B_5$	3.49	3.24
$Mg_{65}Cu_{15}Y_{10}B_{10}$	3.16	--
$Mg_{65}Cu_{25}Y_7B_3$	3.76	3.81
$Mg_{65}Cu_{25}Y_5B_5$	3.71	3.74
$Mg_{65}Cu_{25}B_{10}$	3.61	--

Pure elements:

* Mg: 1.74 Mg/m^3; Cu: 8.96 Mg/m^3; Y: 4.48 Mg/m^3; B: 2.35 Mg/m^3

Table 5.1 Summary of bonding parameter Δx and δ for Mg-Cu-Y-B alloys.

Compositions	**Δx**	**δ**	**Δx · δ**
$\mathbf{Mg_{65}Cu_{25}Y_{10}}$	0.305	0.07	0.021
$\mathbf{Mg_{65}Cu_{24}Y_{10}B_1}$	0.306	0.08	0.025
$\mathbf{Mg_{65}Cu_{22}Y_{10}B_3}$	0.307	0.10	0.031
$\mathbf{Mg_{65}Cu_{20}Y_{10}B_5}$	0.309	0.11	0.034
$\mathbf{Mg_{65}Cu_{15}Y_{10}B_{10}}$	0.321	0.14	0.045
$\mathbf{Mg_{65}Cu_{25}Y_7B_3}$	0.316	0.09	0.028
$\mathbf{Mg_{65}Cu_{25}Y_5B_5}$	0.323	0.10	0.032
$\mathbf{Mg_{65}Cu_{25}B_{10}}$	0.334	0.12	0.040

Table 5.2 Summary of T_g , T_x , ΔT_x and γ value for the Mg-Cu-Y-B amorphous alloys at a heating of 20 K/min.

Compositions	T_g	T_x	ΔT_x	T_m^{solid}	T_m^{liquid}	γ
$Mg_{65}Cu_{25}Y_{10}$	410	468	58	728	760	0.40
$Mg_{65}Cu_{22}Y_{10}B_3$	410	476	66	715	738	0.42
$Mg_{65}Cu_{20}Y_{10}B_5$	420	470	50	712	736	0.41
$Mg_{65}Cu_{15}Y_{10}B_{10}$	420	465	45	---	---	---
$Mg_{65}Cu_{25}Y_7B_3$	420	457	37	---	---	---
$Mg_{65}Cu_{25}Y_5B_5$	408	430	22	---	---	---
$Mg_{65}Cu_{25}B_{10}$	Not amorphous alloy					

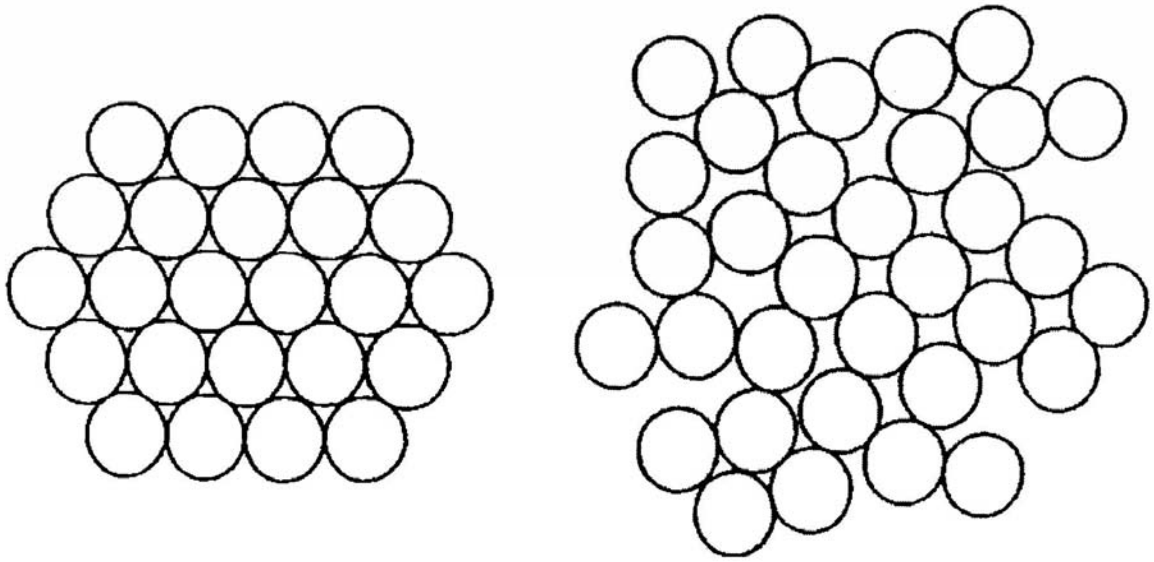

Fig. 1.1 The atomic arrangements of crystal and amorphous alloy [1].

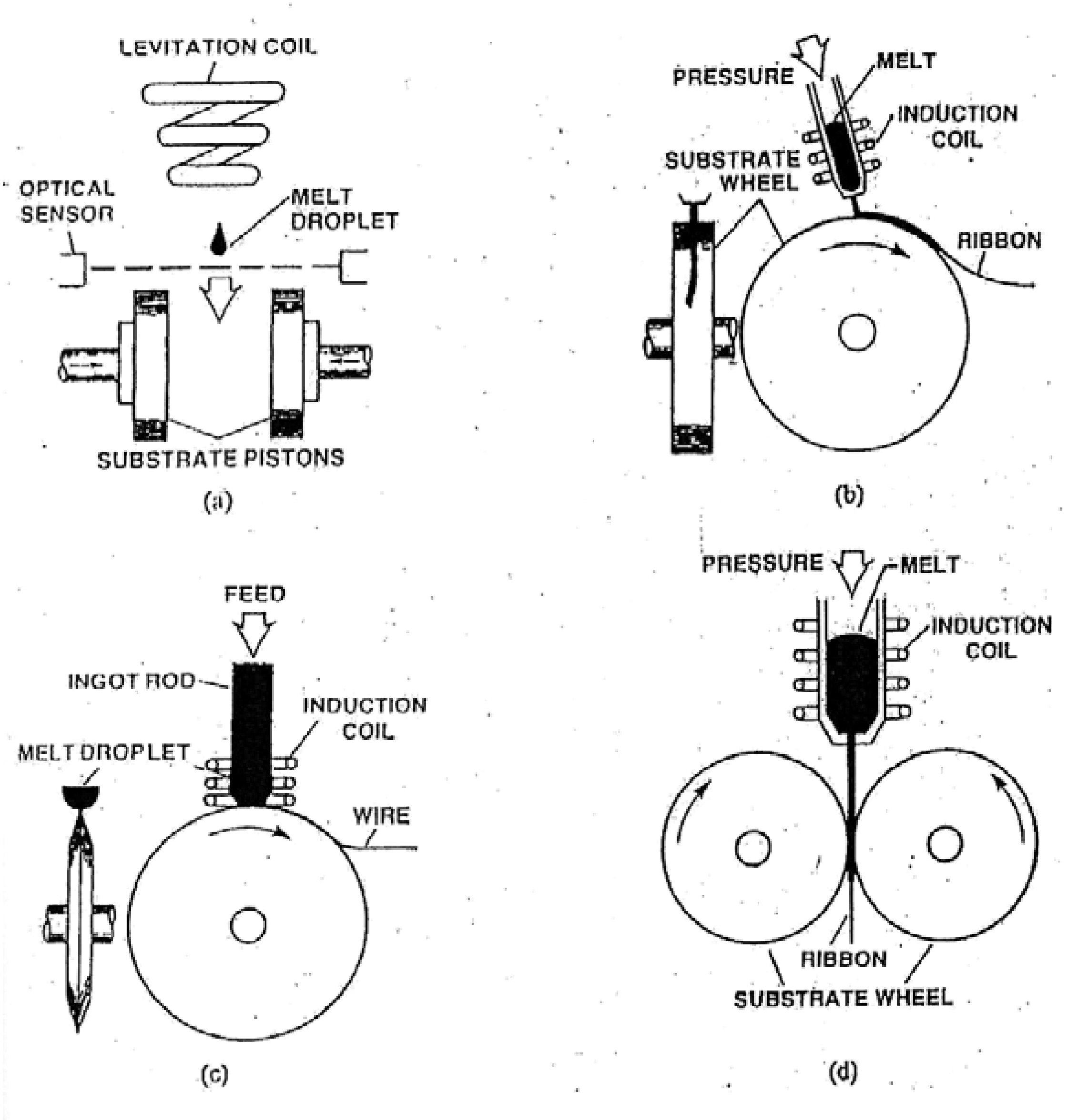

Figs. 2.1 Schematic drawings of four quenching methods from the melt: (a) piston and anvil, (b) melt spinning, (c) melt extraction, and (d) twin roller quenching.

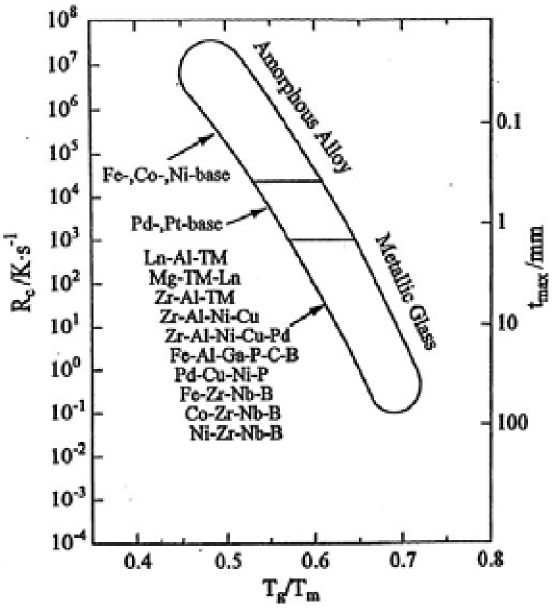

Fig. 2.3 Relationship between the critical cooling rate (R_c), the maximum sample thickness (t_{max}) and reduced glass transition temperature (T_g/T_m) for bulk amorphous systems [9].

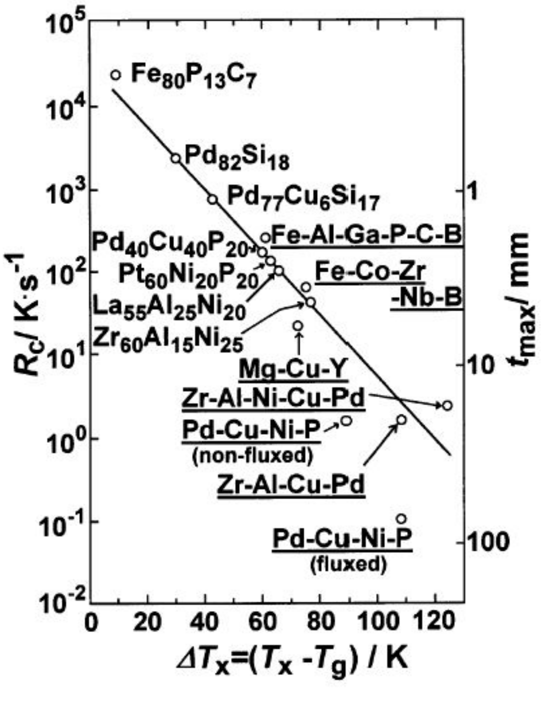

Fig. 2.4 Relationship between the critical cooling rate (R_c) and the maximum sample thickness (t_{max}) for bulk amorphous alloy systems [9].

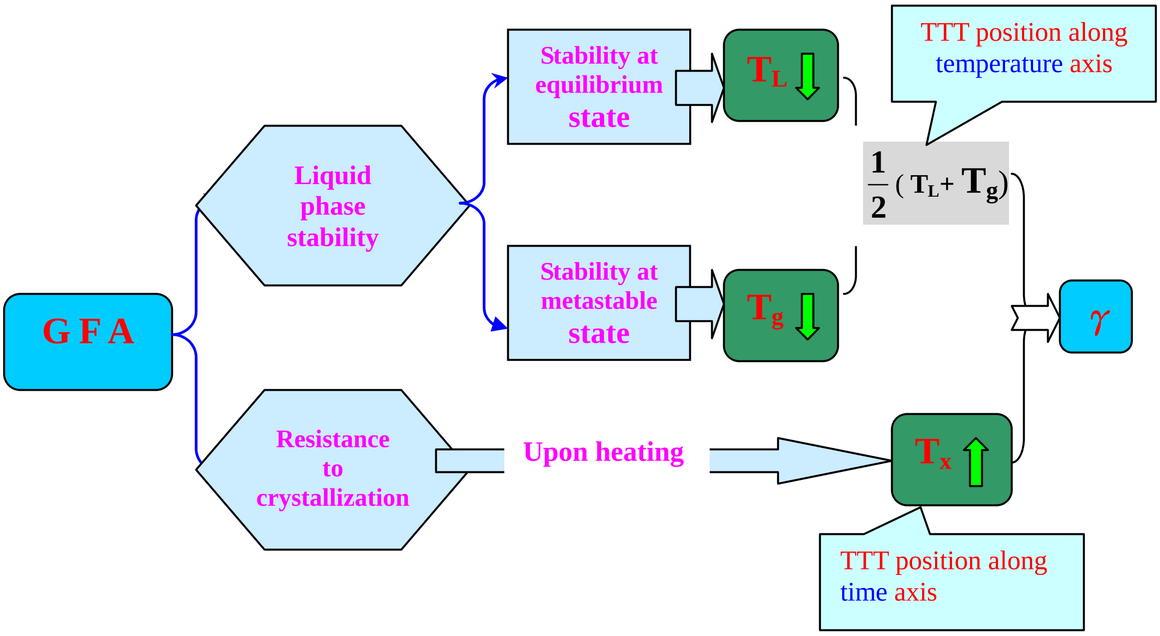

Fig. 2.5 The parameter of γ for glass forming ability (GFA) [32].

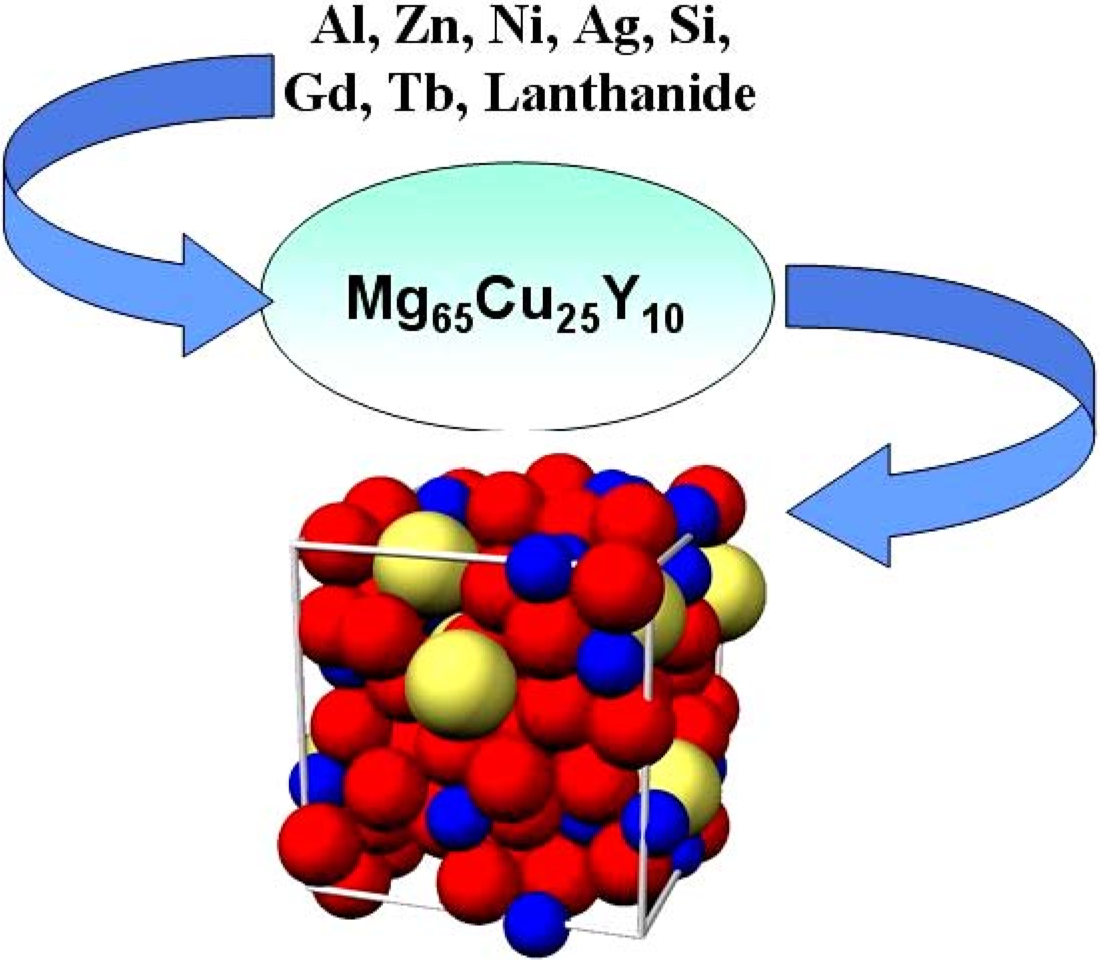

Fig. 2.6 The atomic arrangement of the different atomic size system.

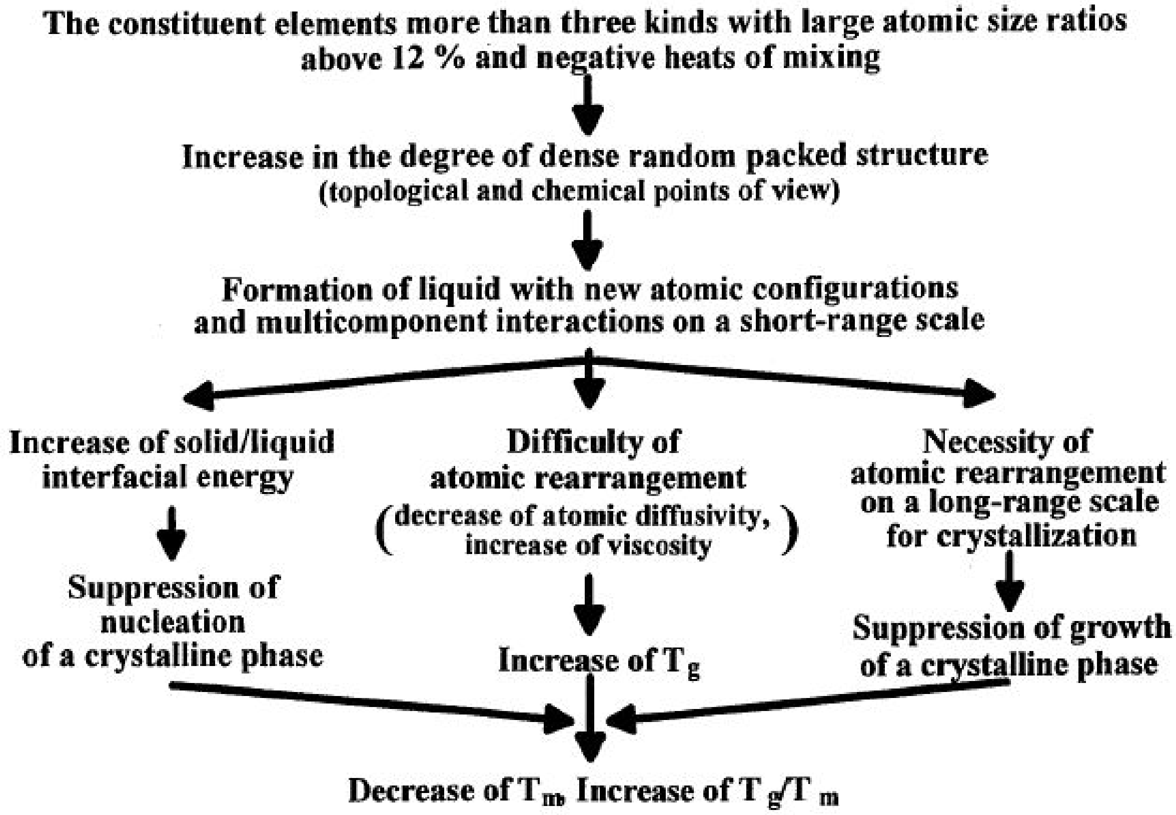

Fig. 2.7 The three empirical rules was proposed by Inoue [33].

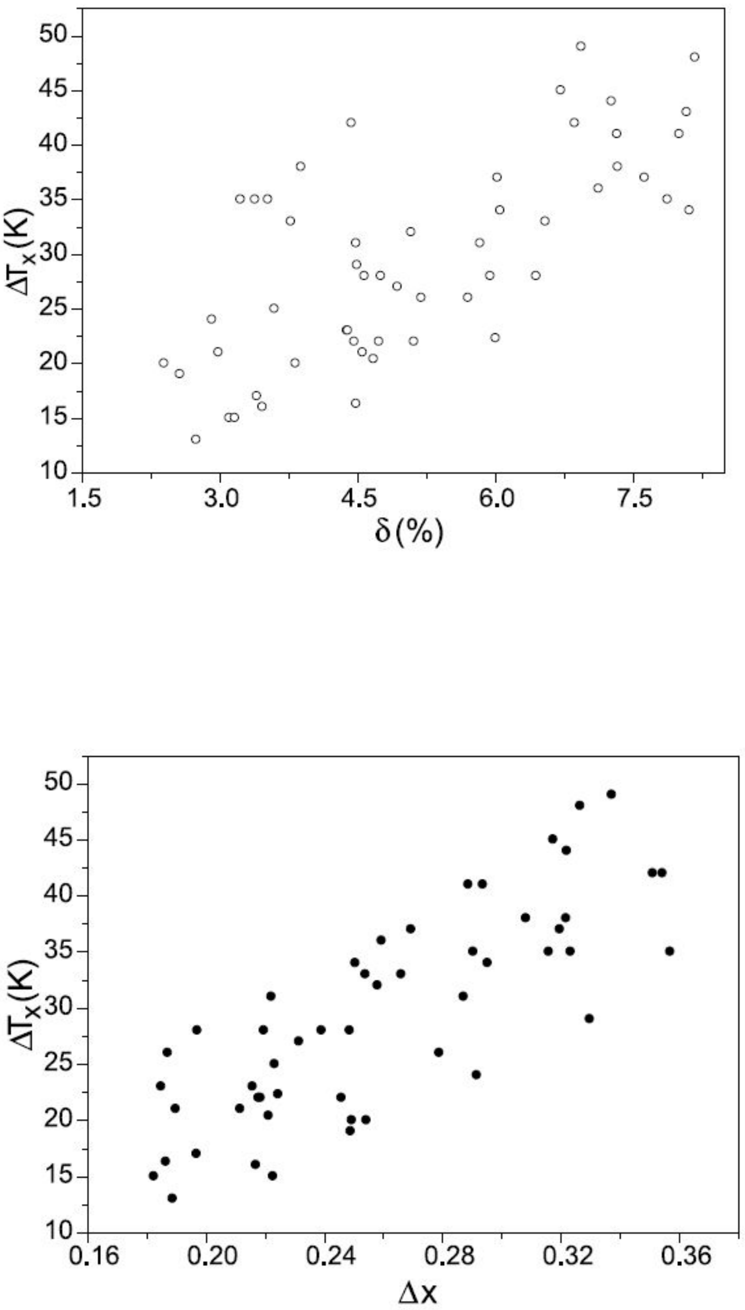

Figs. 2.8 The relationship between the bond parameters, including electronegativity difference (ΔX) and atomic size parameters (δ), and the widths of supercooled liquid region (ΔT_x) in Mg-Based bulk metallic glasses [38].

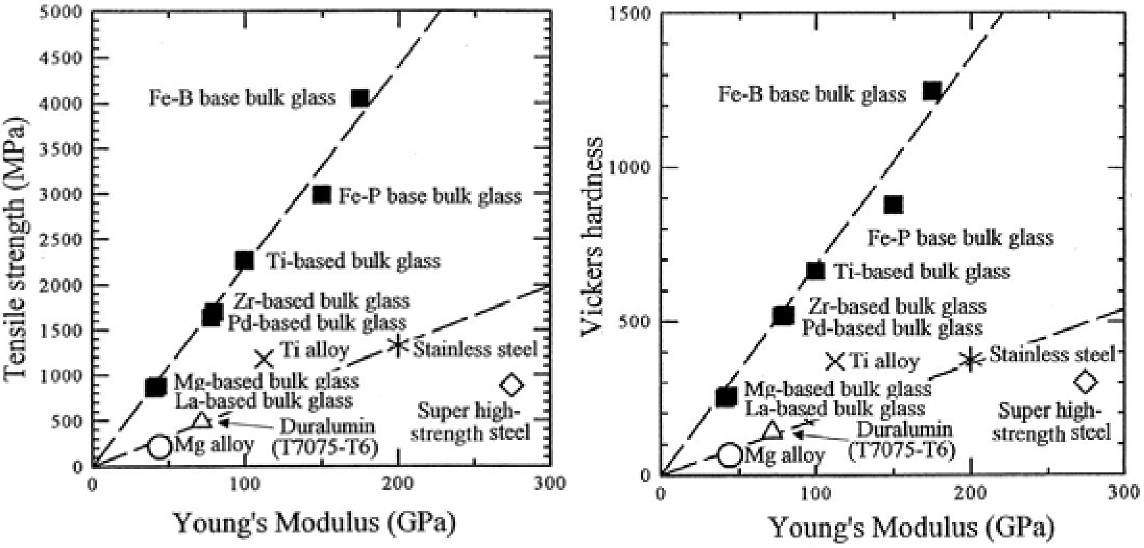

Figs. 2.9 Relationship between the Young’s modulus, tensile strength and hardness for various metallic glass systems [9].

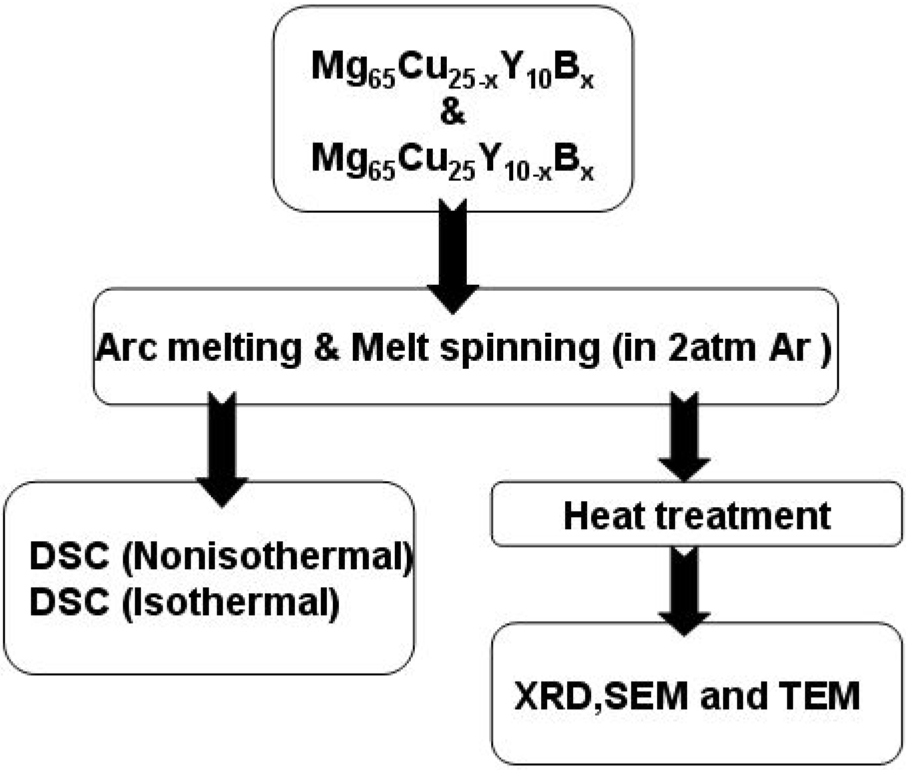

Fig. 3.1 Flow chart showing the experiment procedures.

Fig. 3.2 Photograph of the arc melting device.

Fig. 3.3 Photography of the melt spinning device.

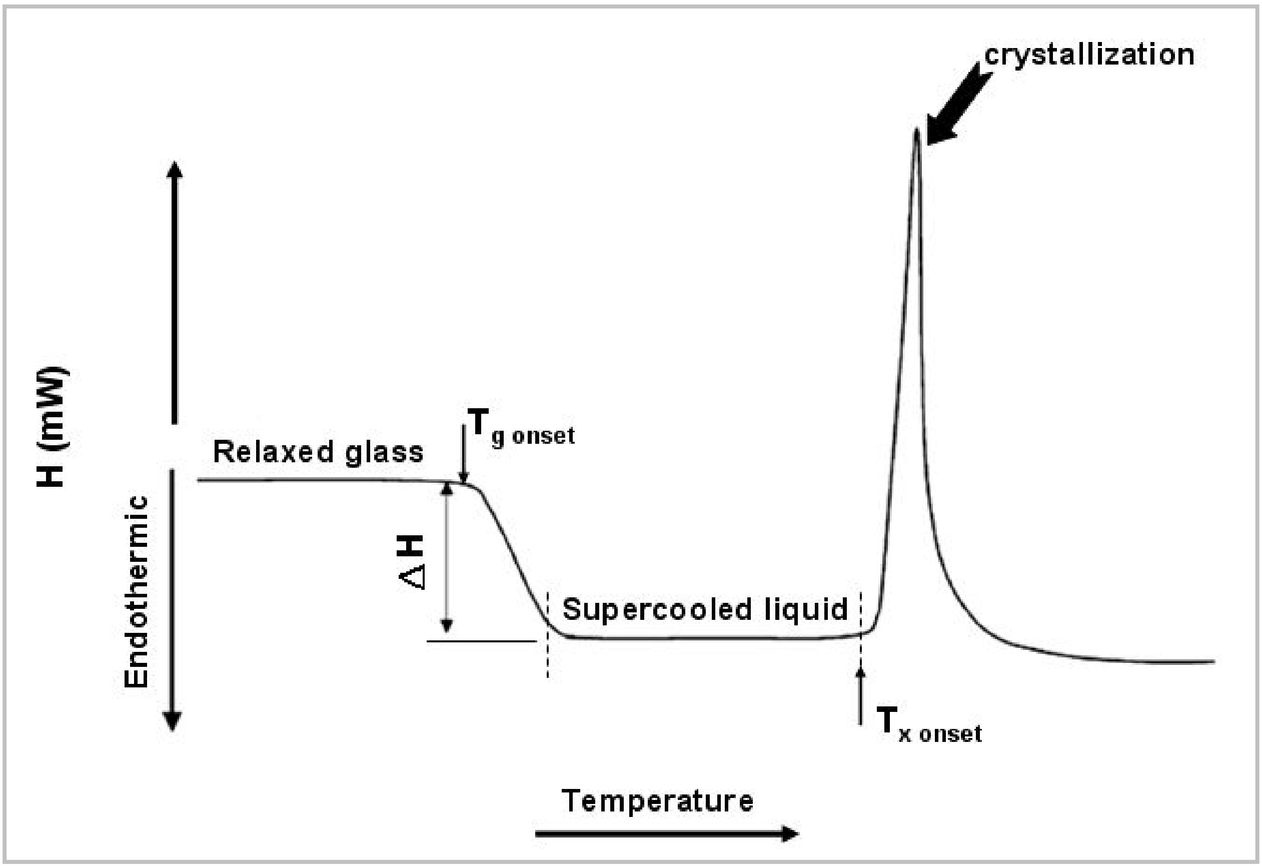

Fig. 3.4   The DSC trace for amorphous alloy at heating.

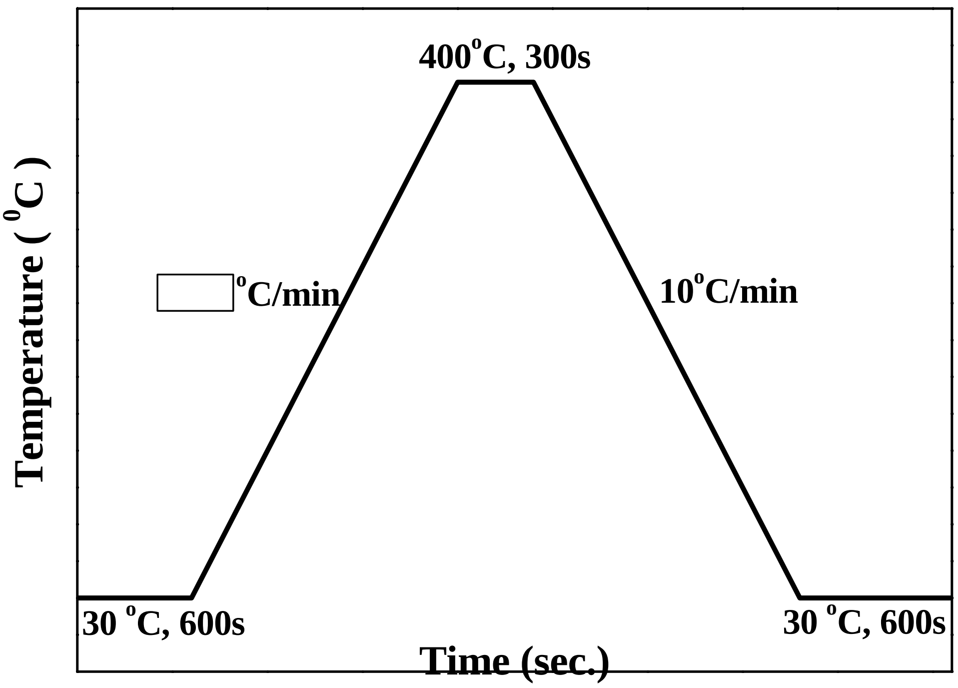

(a)

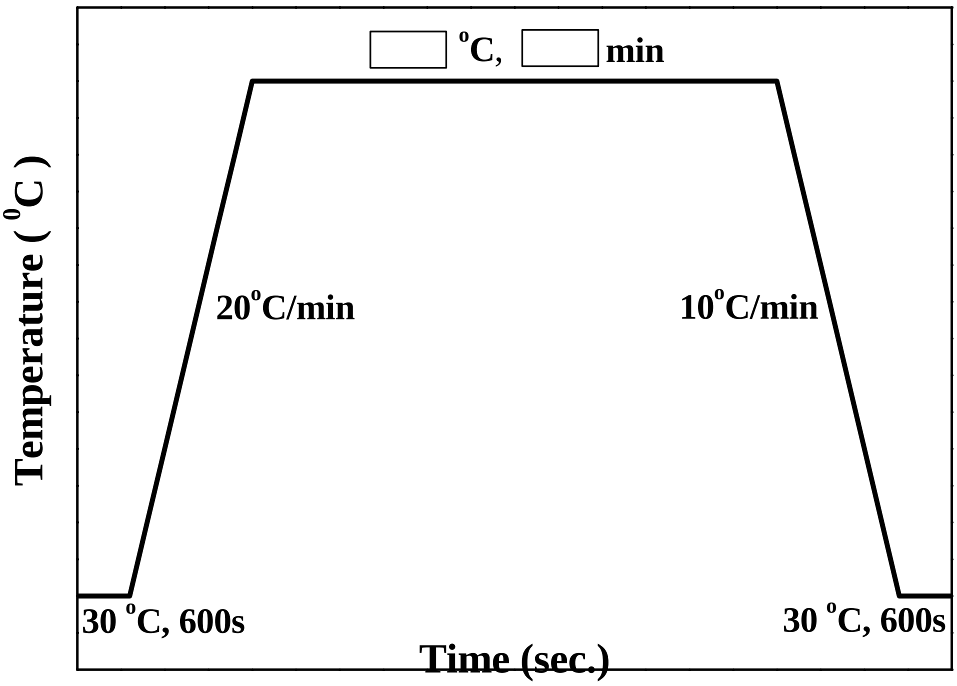

(b)

Fig. 3.5 The DSC programs for (a) non-isothermal, and (b) isothermal analyses.

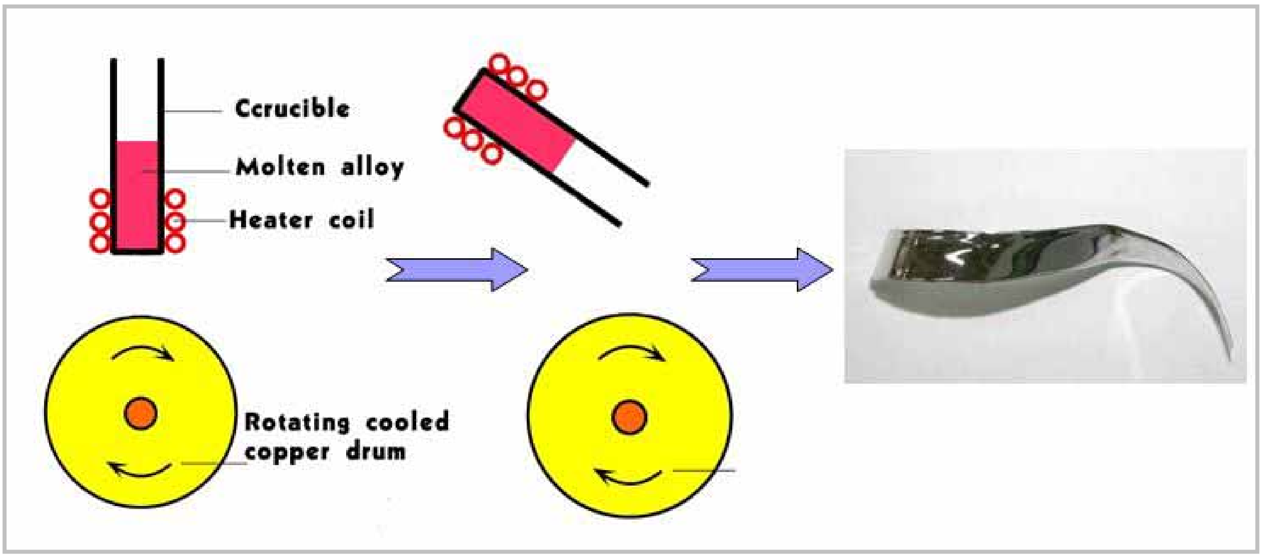

Fig. 4.1 The experiment procedures for Mg-based amorphous alloys.

Fig. 4.2 Surface appearance of the melt spun Mg-Cu-Y-B amorphous alloy.

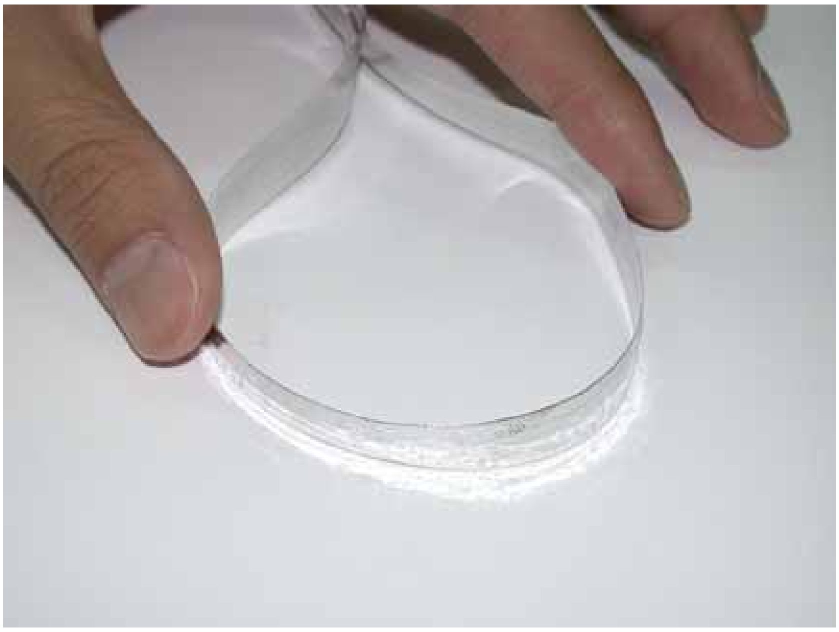

Fig. 4.3 Bending behavior of the Mg-Cu-Y amorphous alloy.

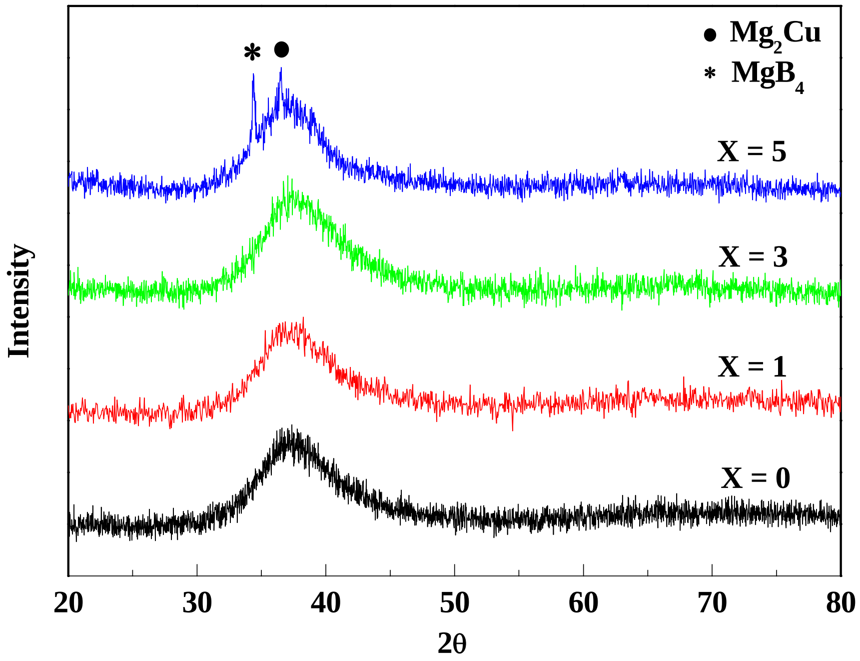

Fig. 4.4 X-ray diffraction patterns for the melt spun $Mg_{65}Cu_{25}Y_{10-x}B_x$ alloy.

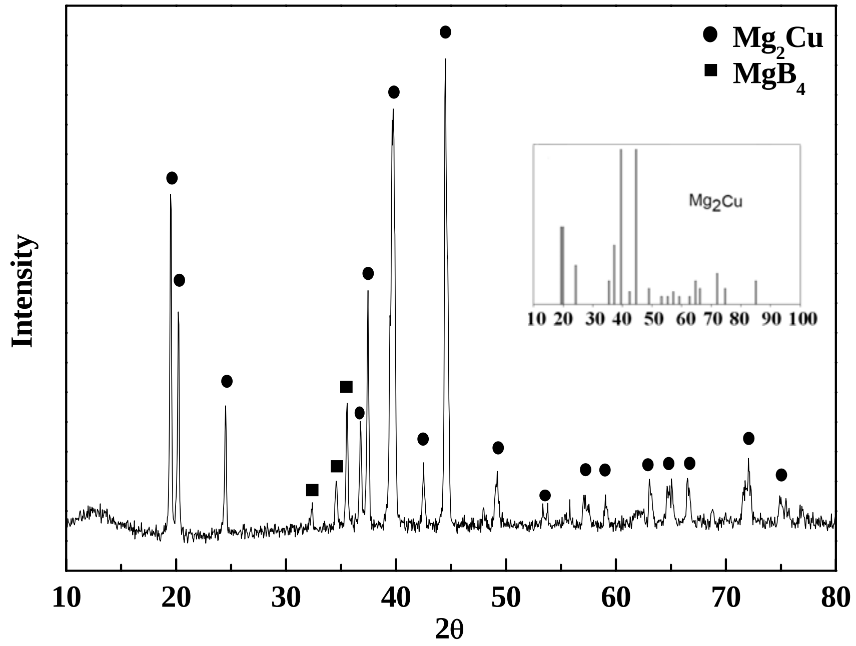

Fig. 4.5 X-ray diffraction patterns of the melt spun $Mg_{65}Cu_{25}B_{10}$ alloy.

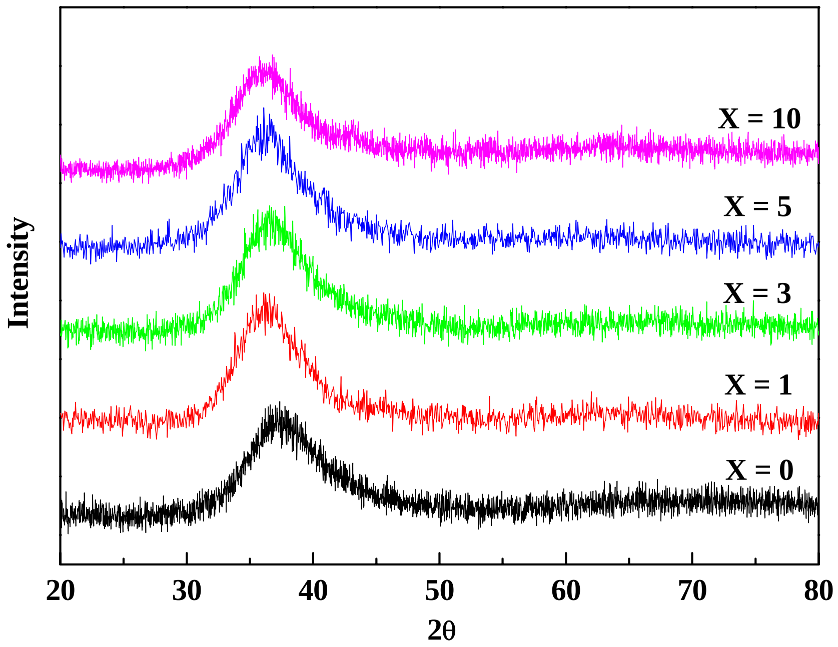

Fig. 4.6 X-ray diffraction patterns for the melt spun $Mg_{65}Cu_{25-x}Y_{10}B_x$ alloy.

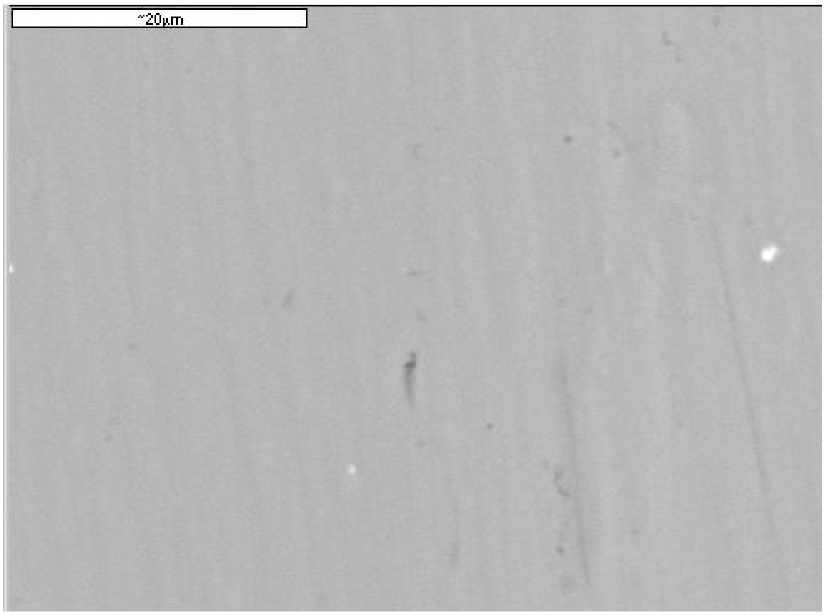

(a)

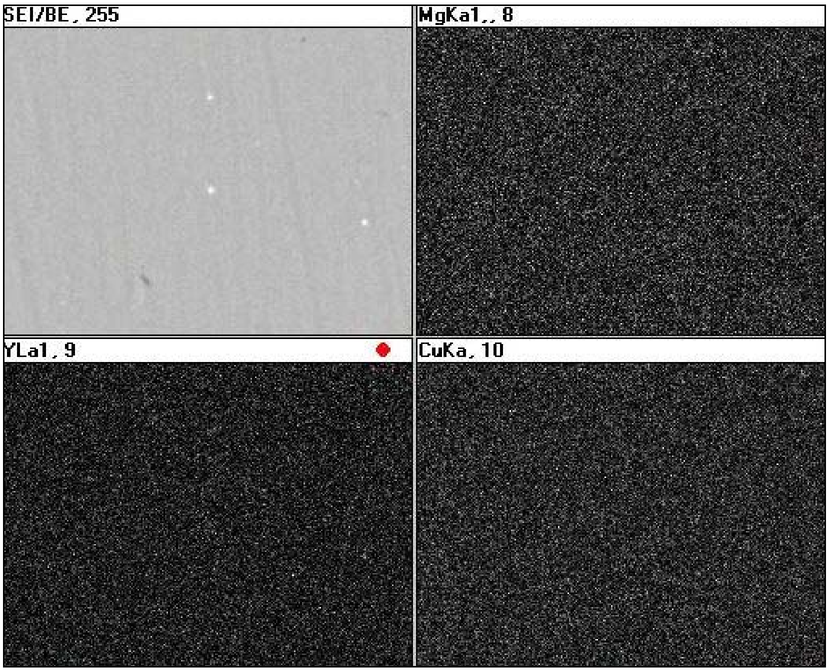

(b)

Fig. 4.7 SEM/EPMA micrographs of the $Mg_{65}Cu_{25}Y_{10}$ metallic glass: (a) BEI image (b) mapping image.

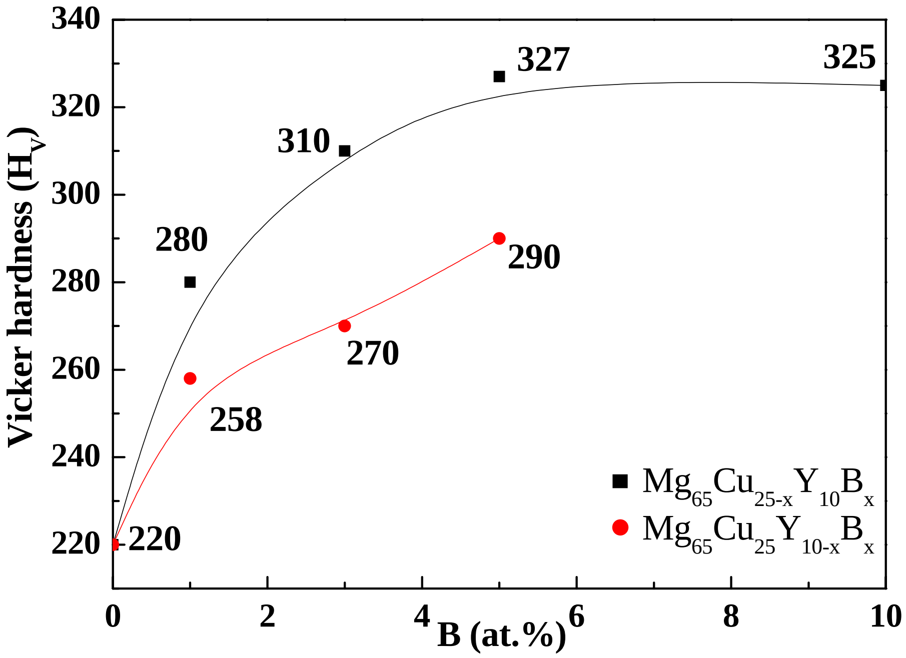

Fig. 4.8 Hardness as a function of B content for the $Mg_{65}Cu_{25-x}Y_{10}B_x$ and $Mg_{65}Cu_{25}Y_{10-x}B_x$ alloys.

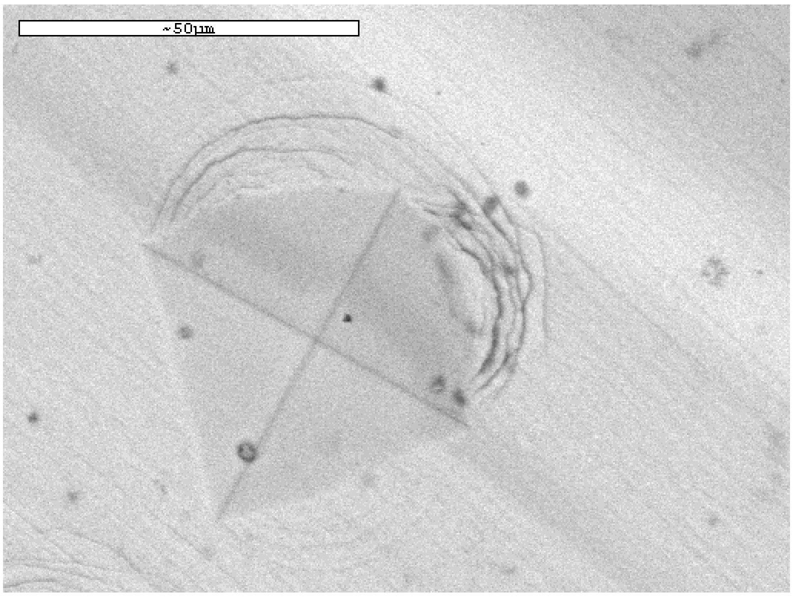

Fig. 4.9 SEM/BEI micrograph showing the shear bands in the Mg-Cu-Y-B alloy.

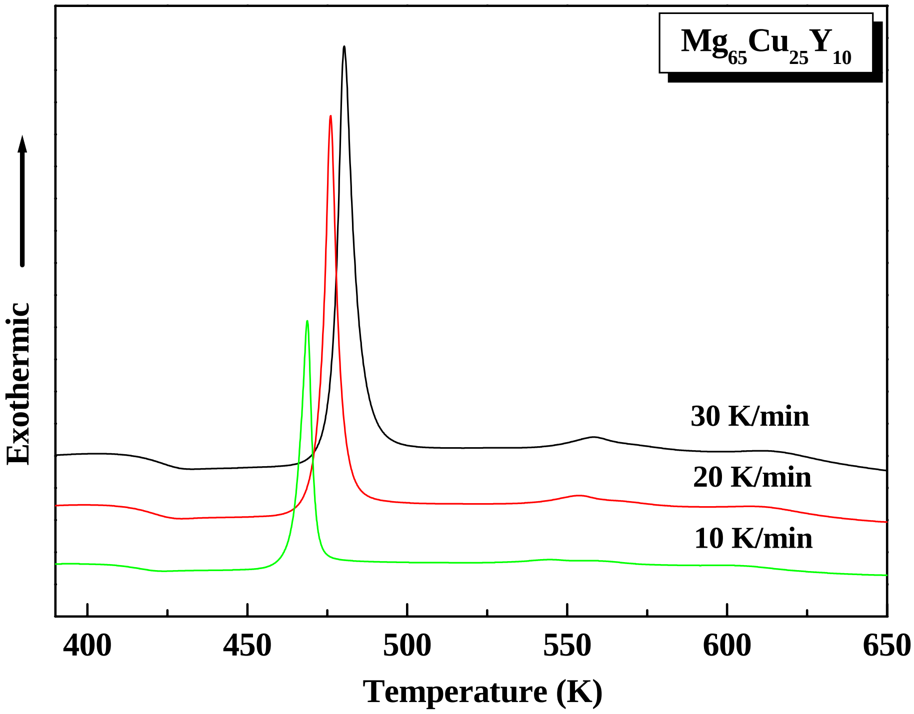

Fig. 4.10 DSC curves of the amorphous $Mg_{65}Cu_{25}Y_{10}$ alloy.

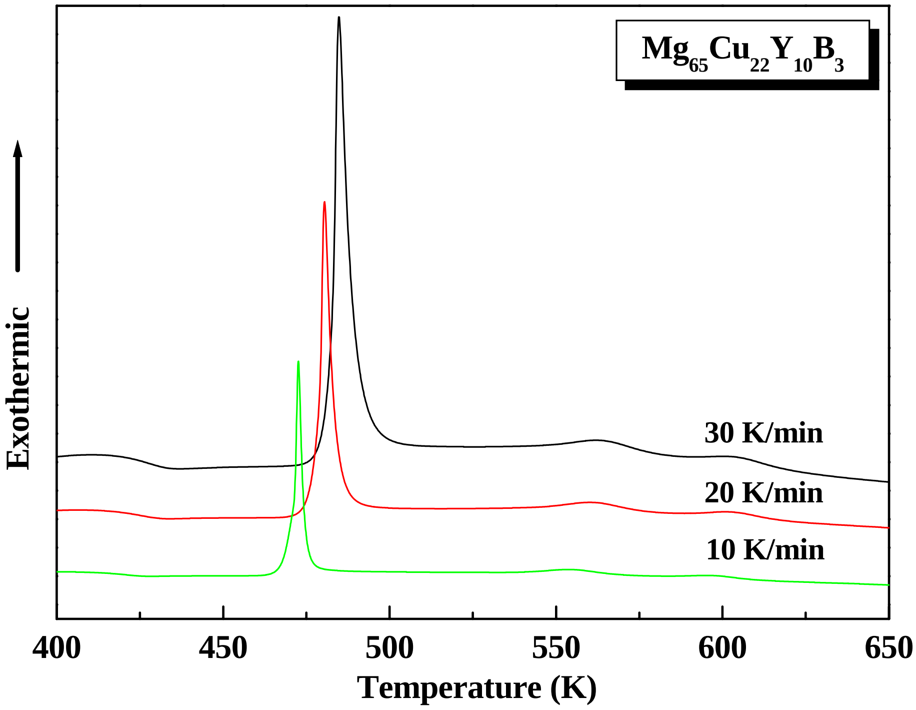

Fig. 4.11 DSC curves of the amorphous $Mg_{65}Cu_{22}Y_{10}B_3$ alloy.

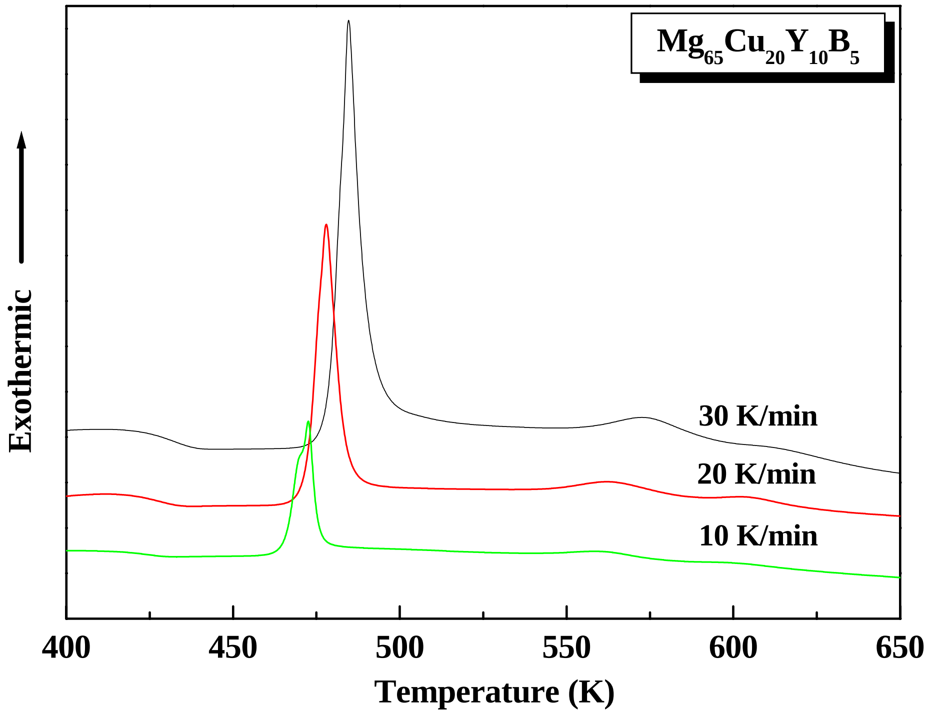

Fig. 4.12 DSC curves of the amorphous $Mg_{65}Cu_{20}Y_{10}B_5$ alloy.

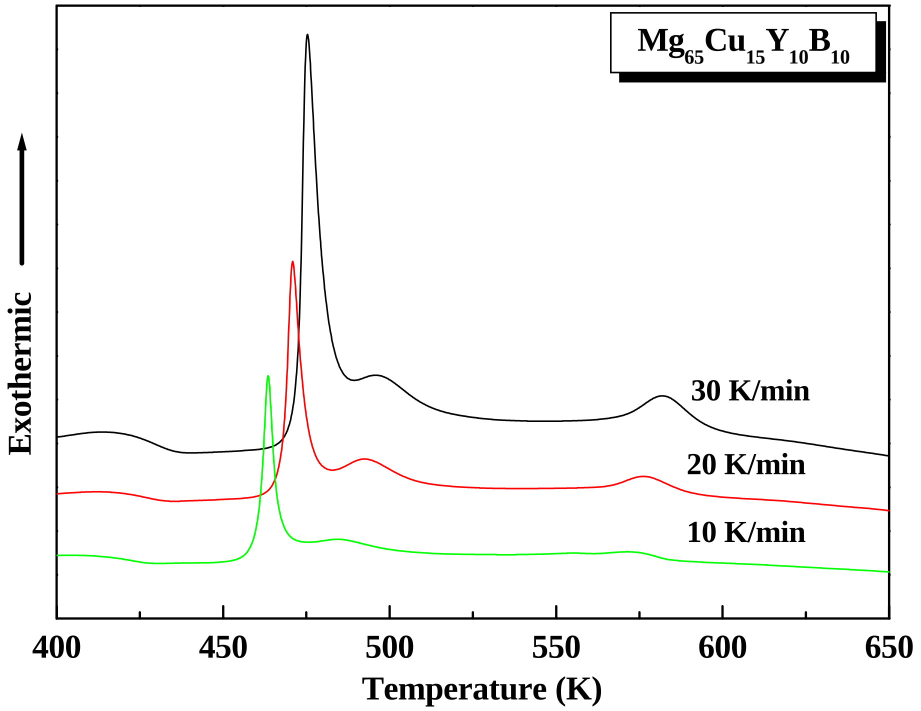

Fig. 4.13 DSC curves of the amorphous $Mg_{65}Cu_{15}Y_{10}B_{10}$ alloy.

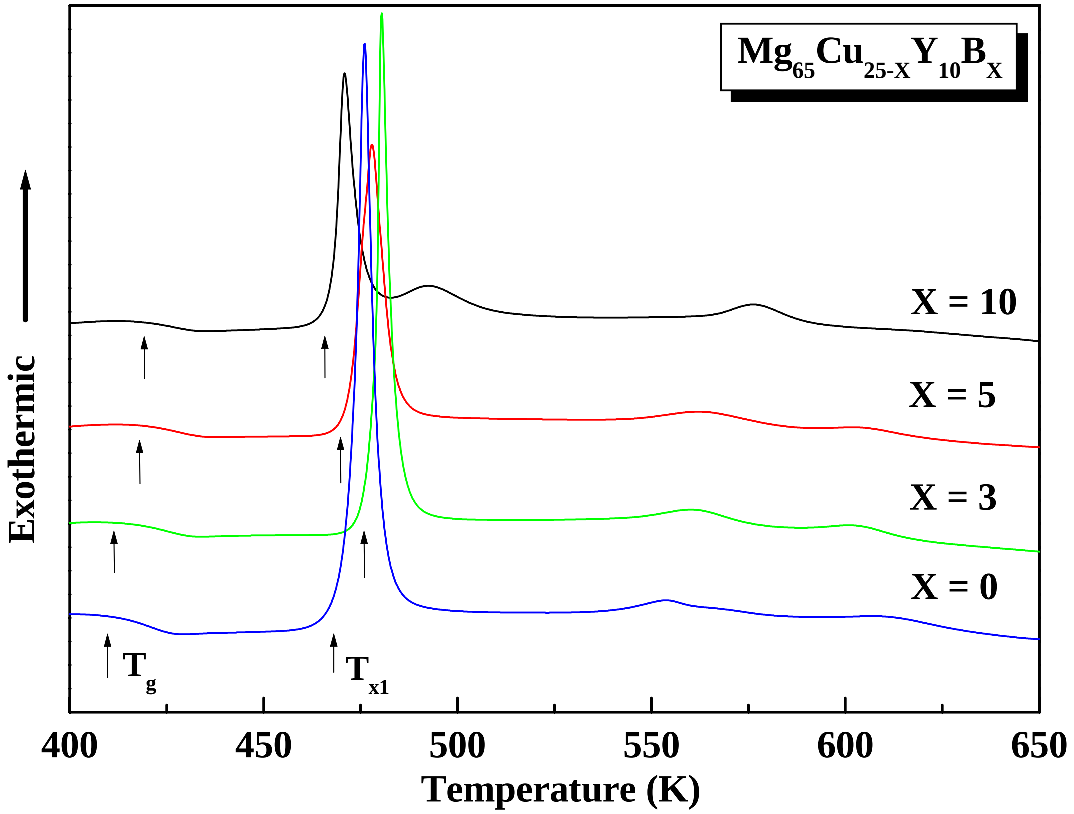

Fig. 4.14 DSC curves of the amorphous $Mg_{65}Cu_{25-x}Y_{10}B_x$ (x = 0, 3, 5, 10) alloy at a heating rate of 20 K/min.

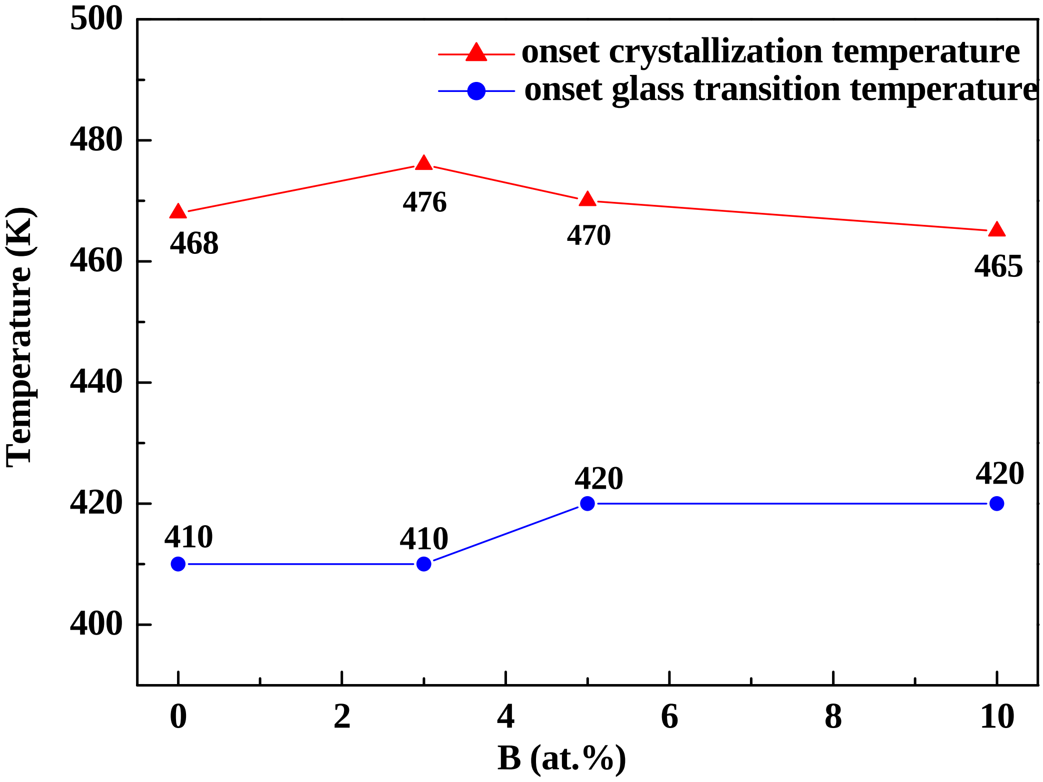

Fig. 4.15 Glass transition and crystallization temperature as a function of B content for the $Mg_{65}Cu_{25-x}Y_{10}B_x$ alloys.

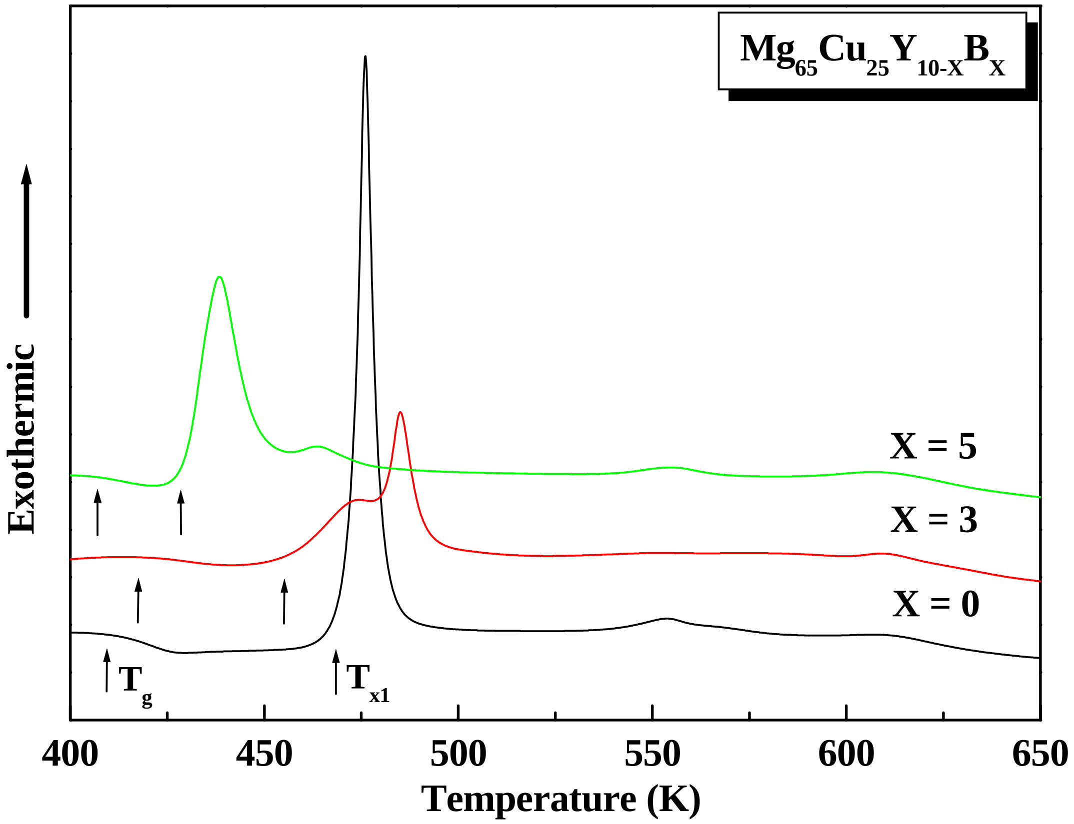

Fig. 4.16 DSC curves of the amorphous $Mg_{65}Cu_{25}Y_{10-x}B_x$ (x = 0, 3, 5) alloys at a heating rate of 20 K/min.

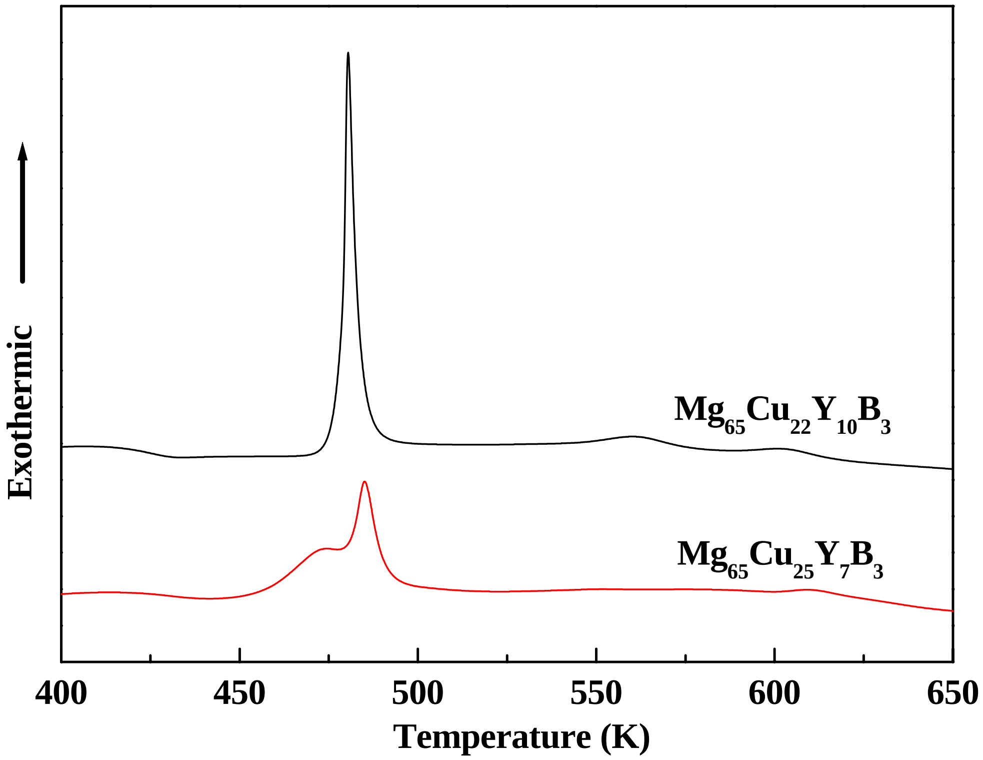

Fig. 4.17 DSC curves of the amorphous $Mg_{65}Cu_{25}Y_7B_3$ and $Mg_{65}Cu_{22}Y_{10}B_3$ alloys at a heating rate of 20 K/min.

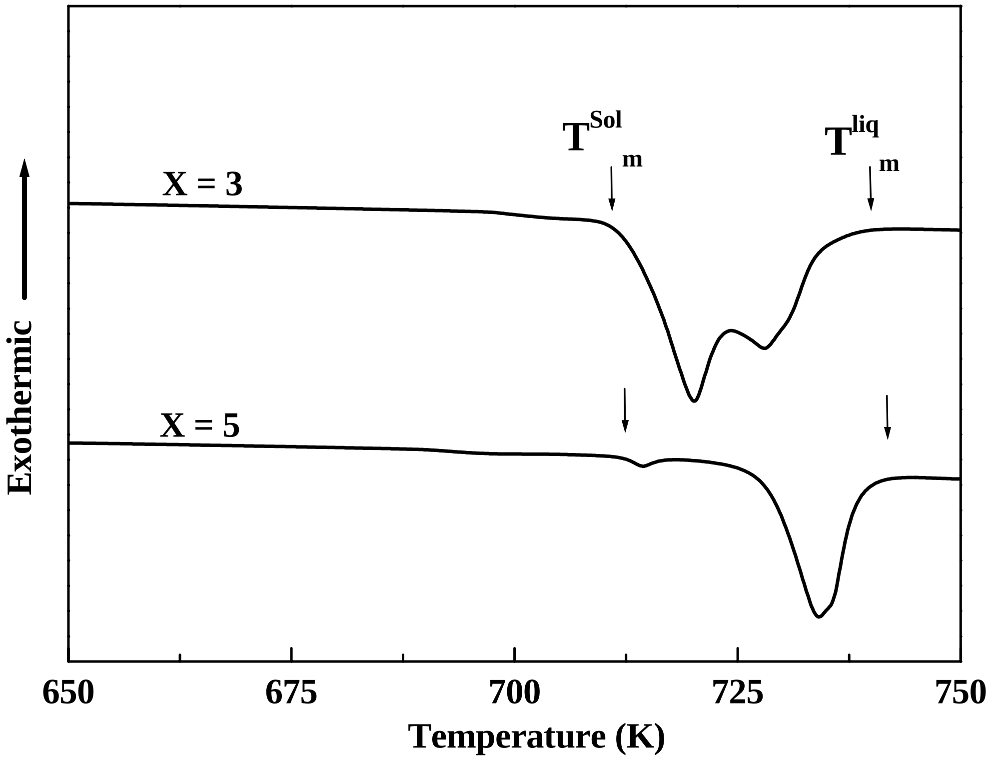

Fig. 4.18 DSC traces showing the melting endotherms obtained from the $Mg_{65}Cu_{25}Y_{10-x}B_x$ (x = 3, 5) alloy at a heating rate of 20 K/min.

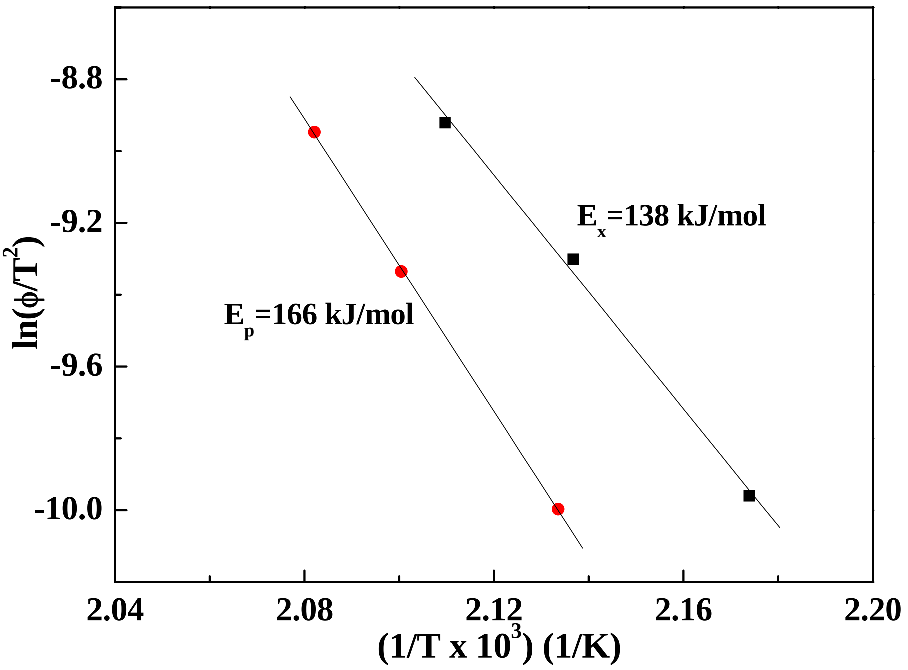

(a)

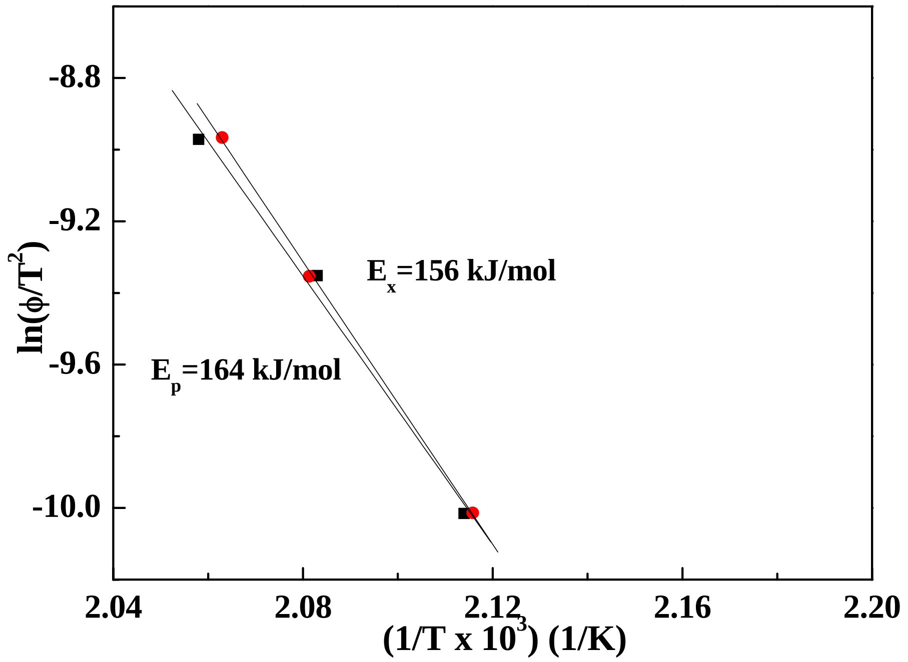

(b)

Fig. 4.19 Kissinger plots for the melt spun alloys: (a) $Mg_{65}Cu_{25}Y_{10}$ and (b) $Mg_{65}Cu_{22}Y_{10}B_3$.

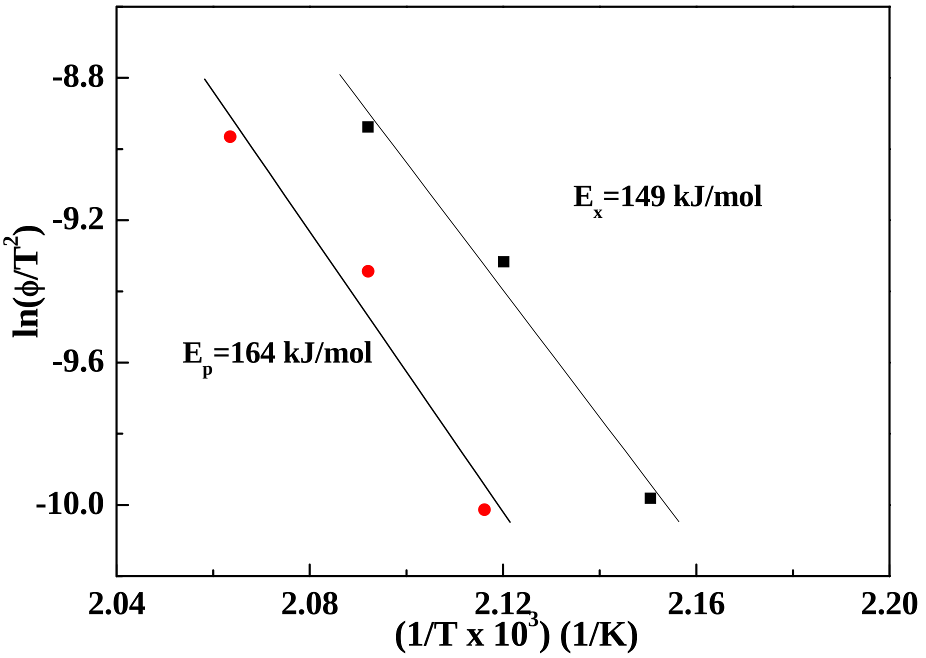

(a)

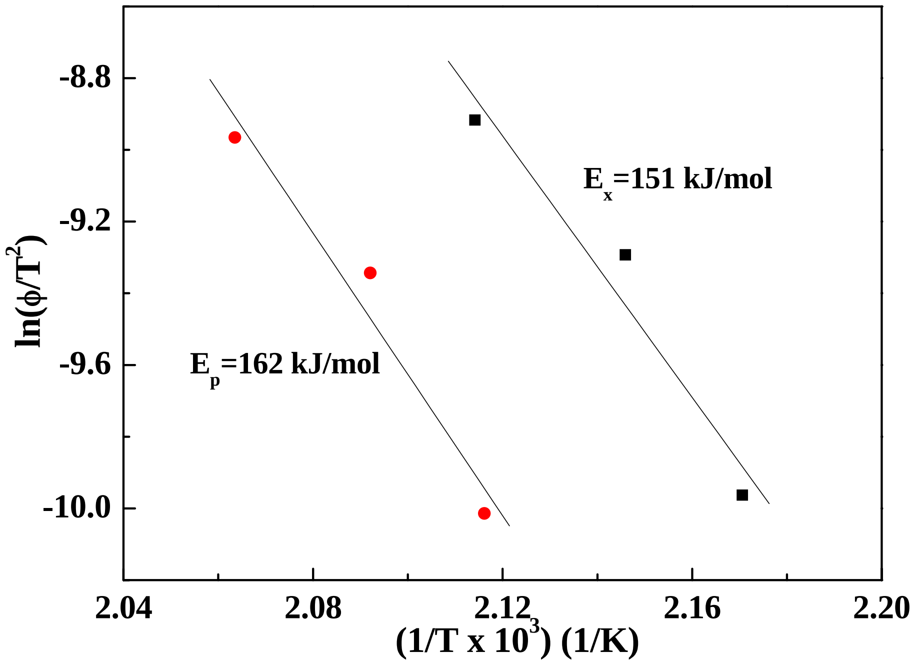

(b)

Fig. 4.20 Kissinger plots for the melt spun alloys: (a) $Mg_{65}Cu_{20}Y_{10}B_5$ and (b) $Mg_{65}Cu_{15}Y_{10}B_{10}$.

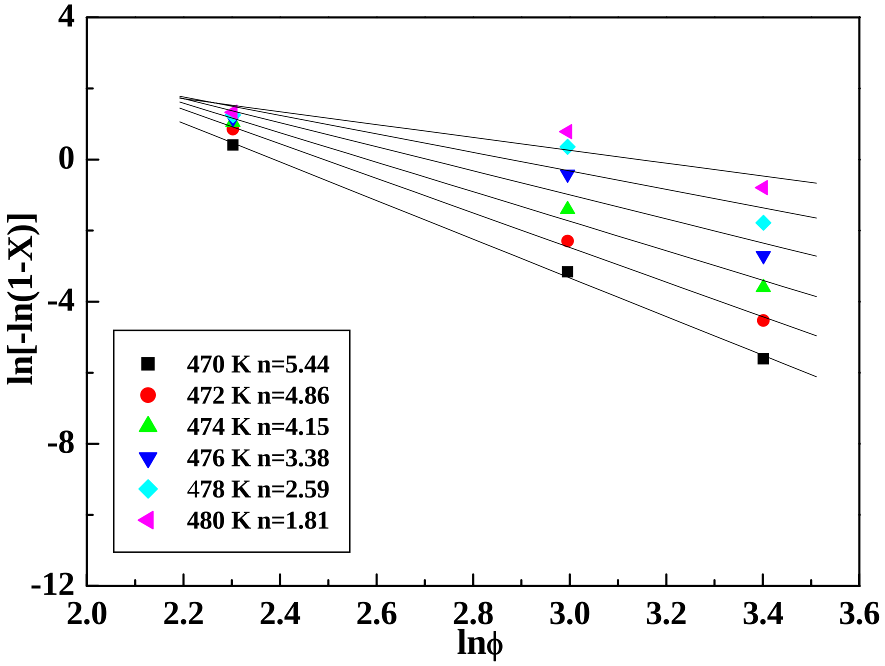

Fig. 4.21 The extraction of the n value from the modified non-isothermal equation for $Mg_{65}Cu_{25}Y_{10}$.

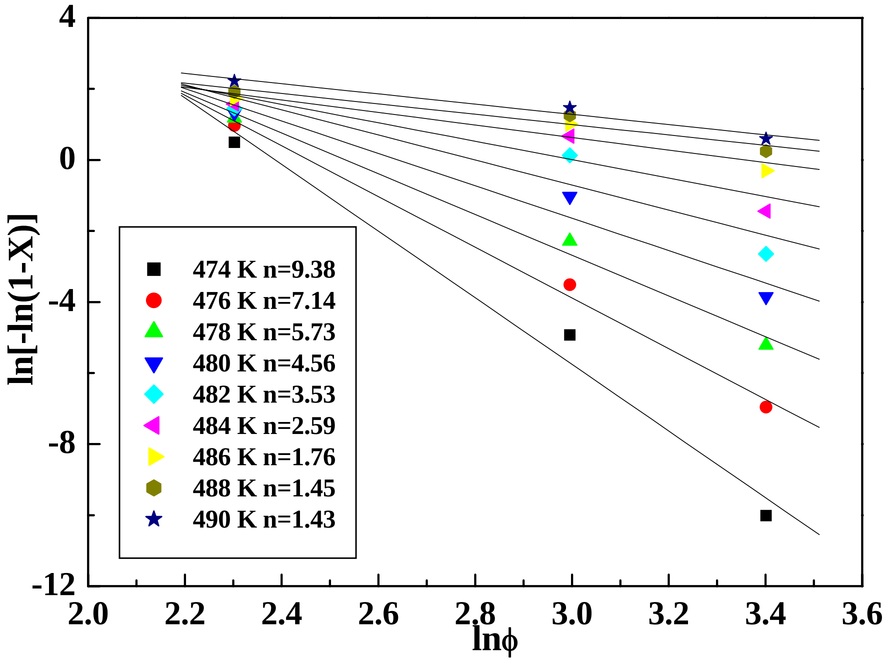

Fig. 4.22 The extraction of the n value from the modified non-isothermal equation for $Mg_{65}Cu_{22}Y_{10}B_3$.

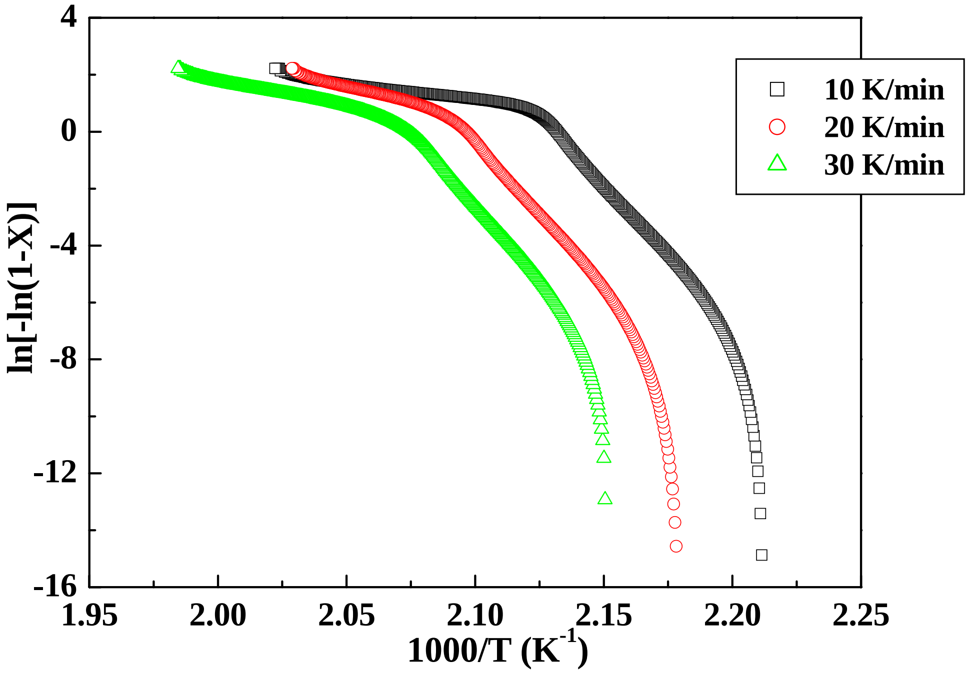

Fig. 4.23 Extraction of the activation energy from the modified non-isothermal DSC scan for $Mg_{65}Cu_{25}Y_{10}$.

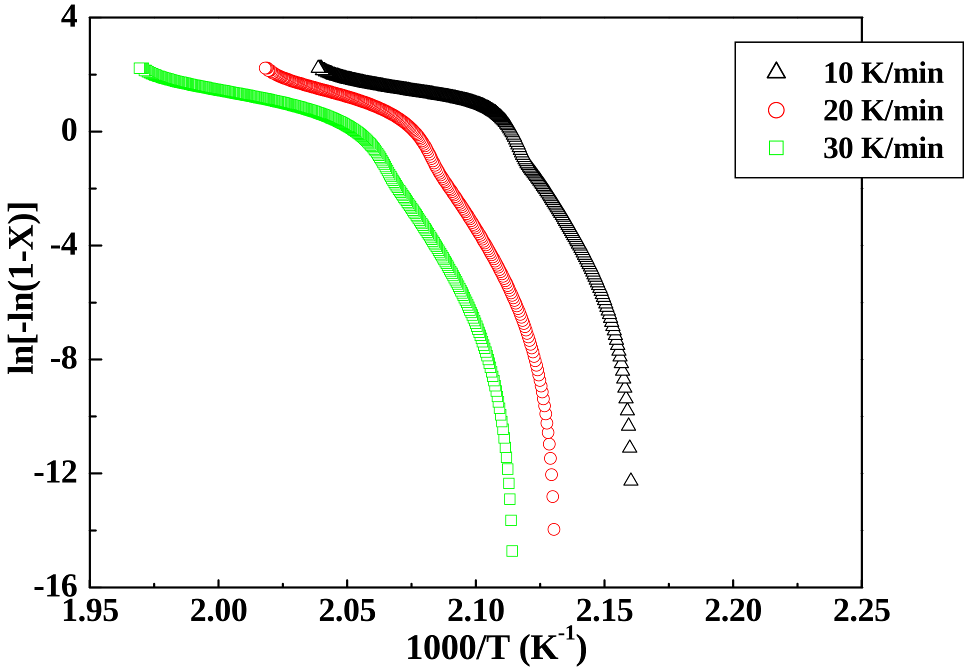

Fig. 4.24 Extraction of the activation energy from the modified non-isothermal DSC scan for $Mg_{65}Cu_{22}Y_{10}B_3$.

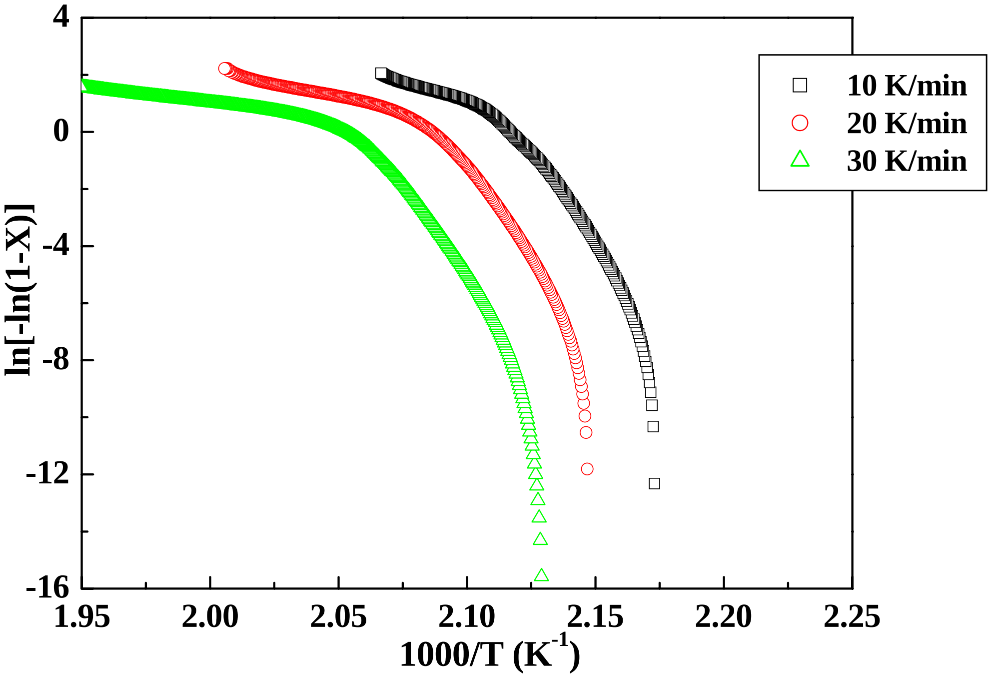

Fig. 4.25 Extraction of the activation energy from the modified non-isothermal DSC scan for $Mg_{65}Cu_{20}Y_{10}B_5$.

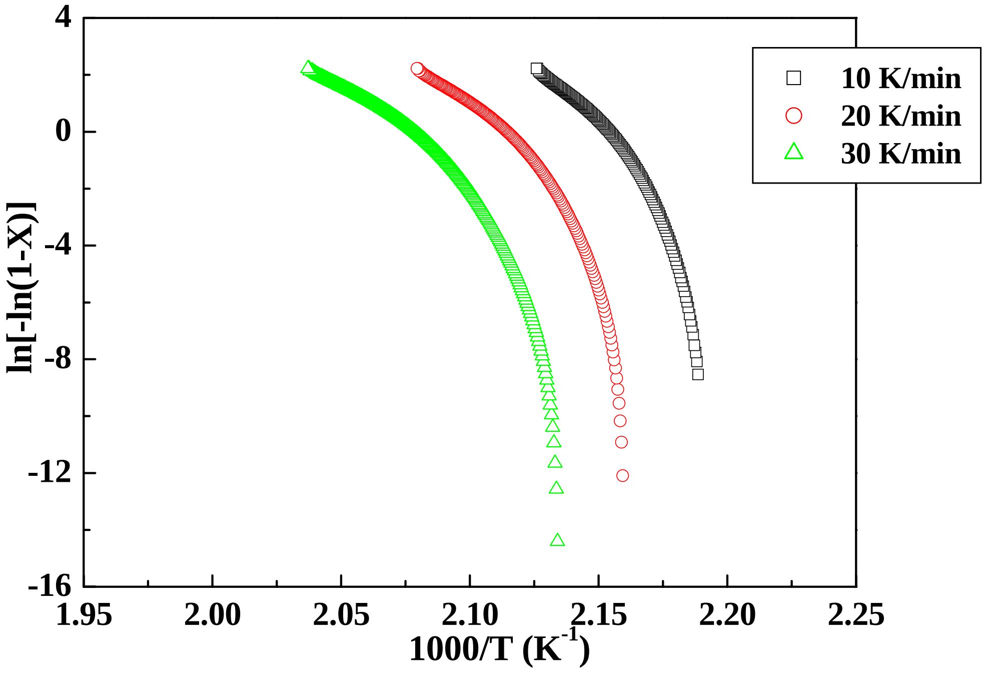

Fig. 4.26 Extraction of the activation energy from the modified non-isothermal DSC scan for $Mg_{65}Cu_{15}Y_{10}B_{10}$.

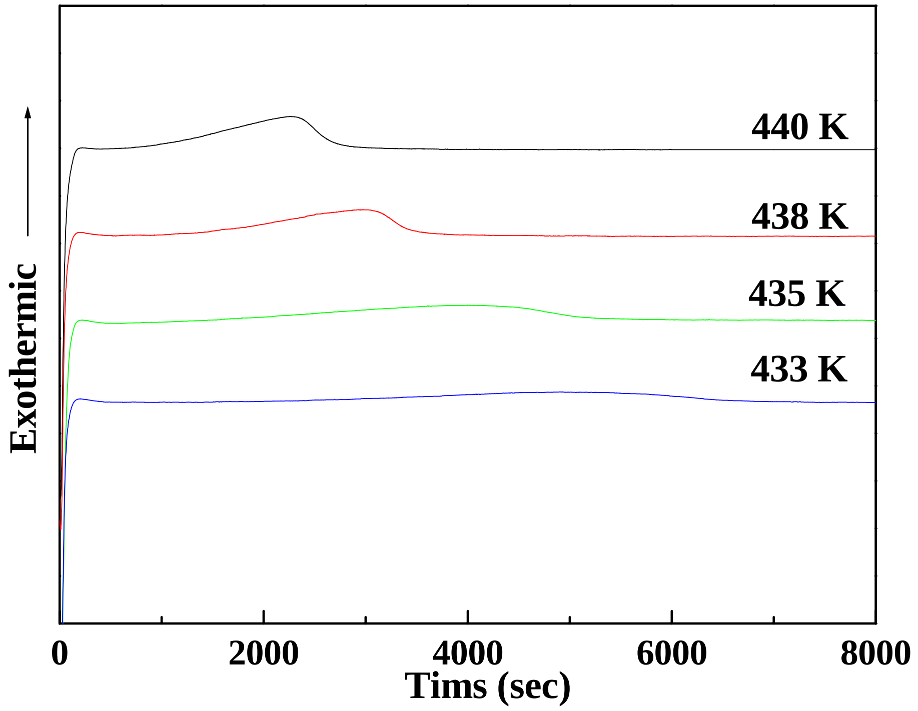

Fig. 4.27 DSC trace of isothermal annealing for $Mg_{65}Cu_{25}Y_{10}$ amorphous alloy.

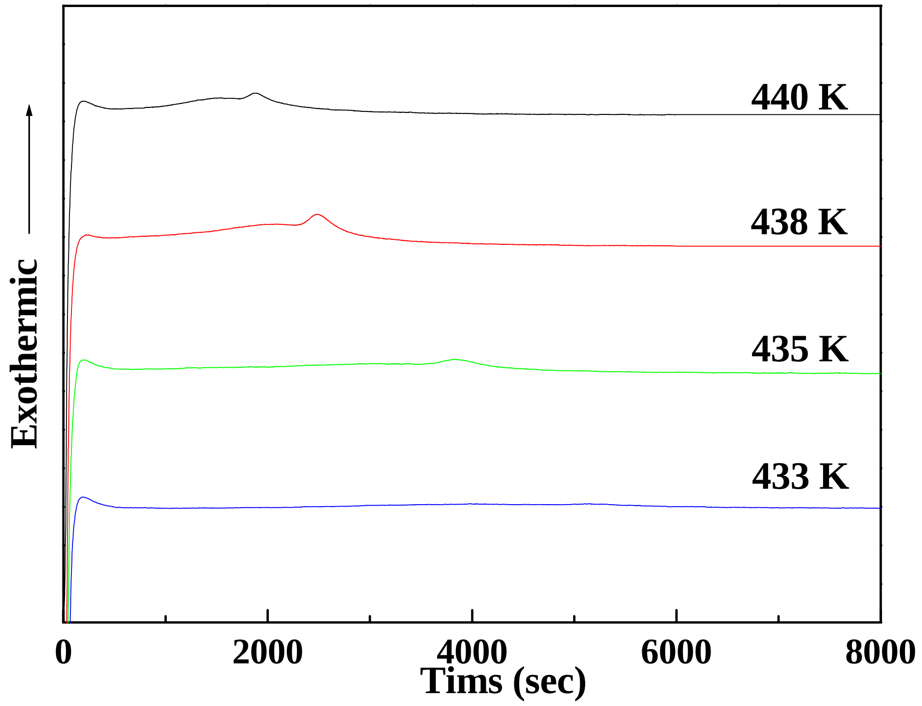

Fig. 4.28 DSC trace of isothermal annealing for $Mg_{65}Cu_{22}Y_{10}B_3$ amorphous alloy.

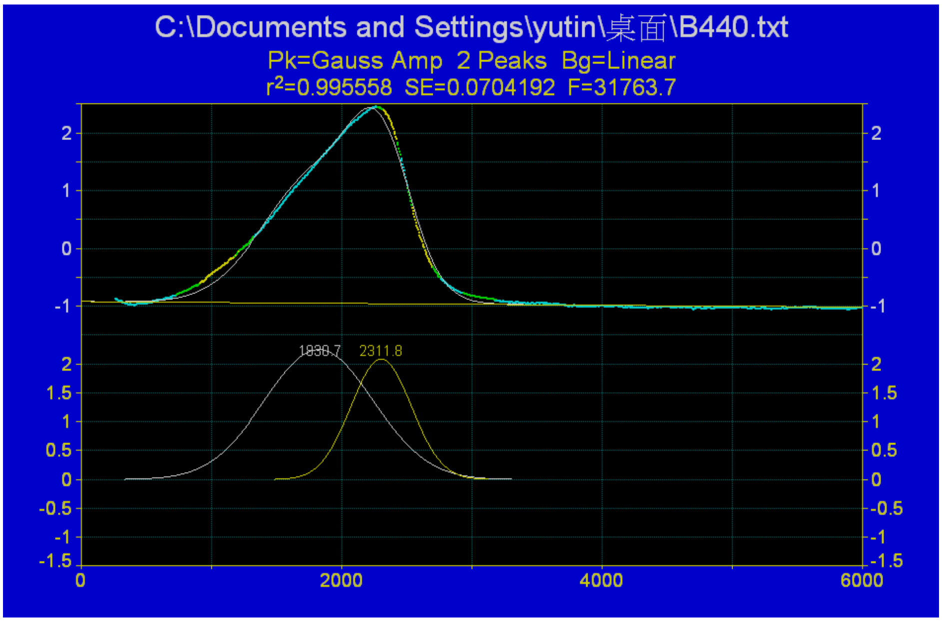

Fig. 4.29 PeakFit software for $Mg_{65}Cu_{25}Y_{10}$.

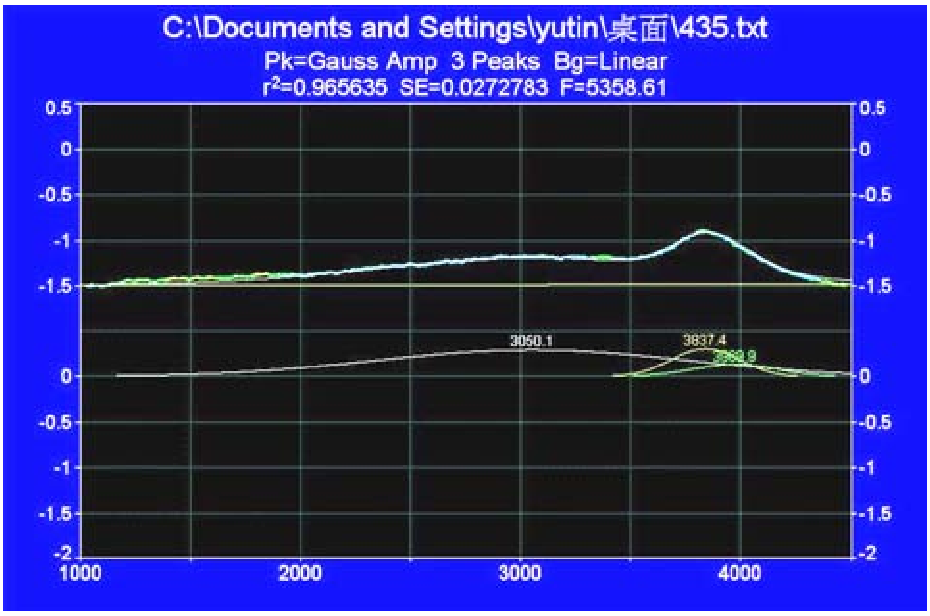

Fig. 4.30 PeakFit software for $Mg_{65}Cu_{22}Y_{10}B_3$.

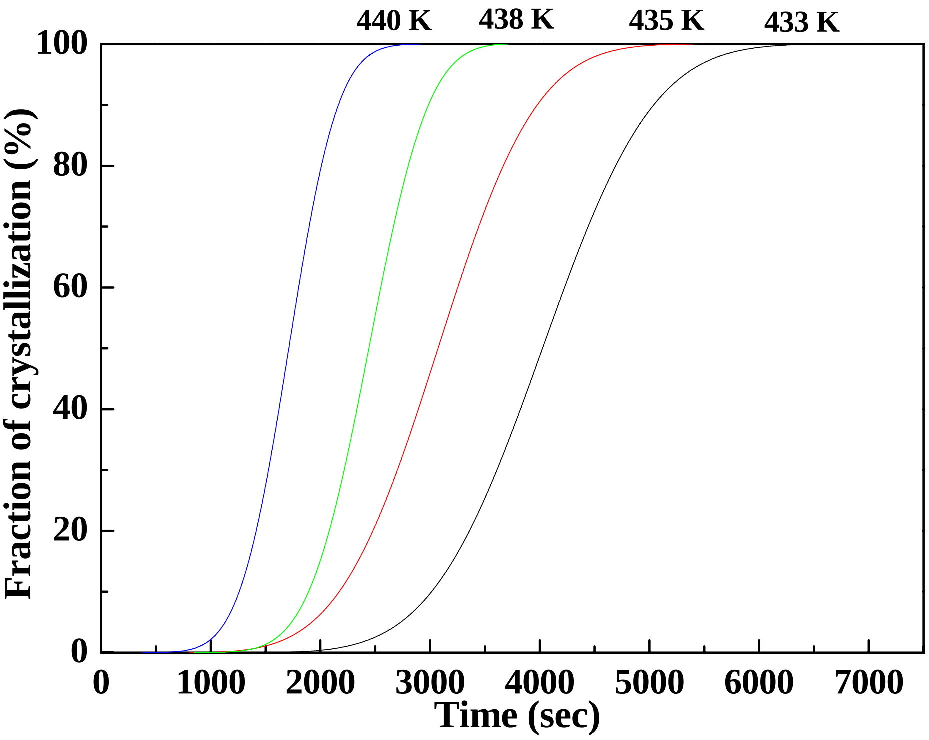

Fig. 4.31 The plot of transformed volume fraction versus time for $Mg_{65}Cu_{25}Y_{10}$.

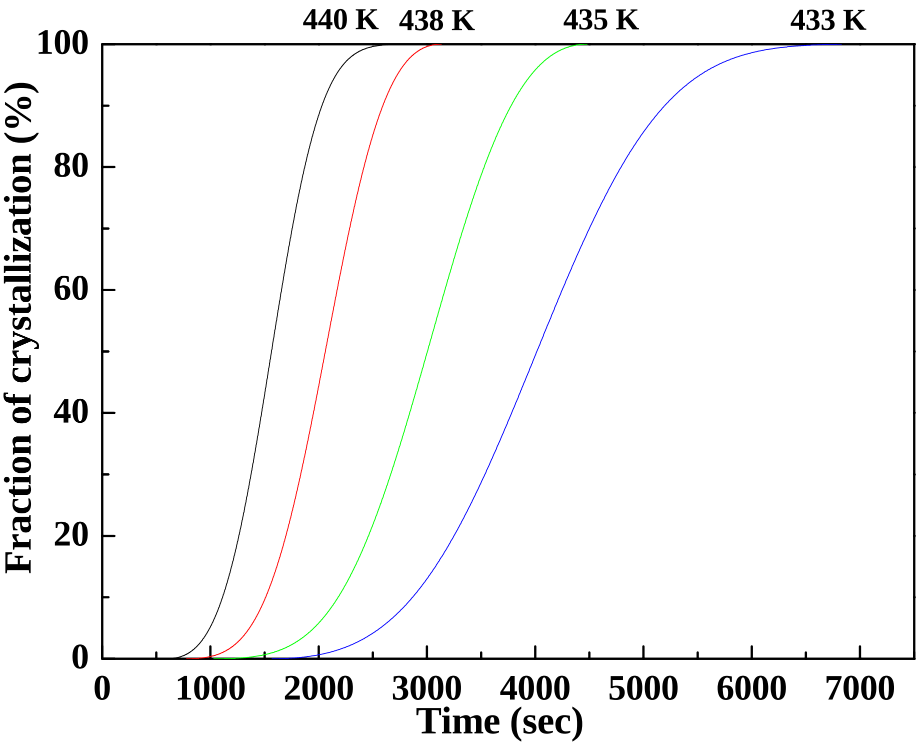

Fig. 4.32 The plot of transformed volume fraction versus time for $Mg_{65}Cu_{22}Y_{10}B_3$.

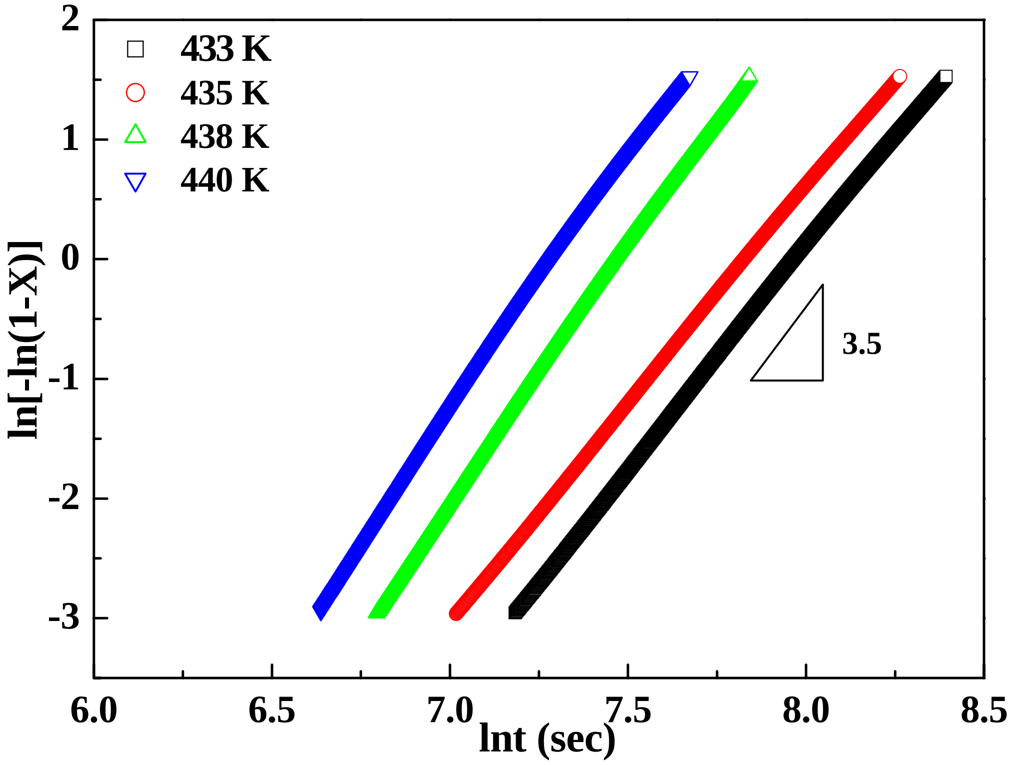

Fig. 4.33 The variation of Avrami exponent n for $Mg_{65}Cu_{25}Y_{10}$.

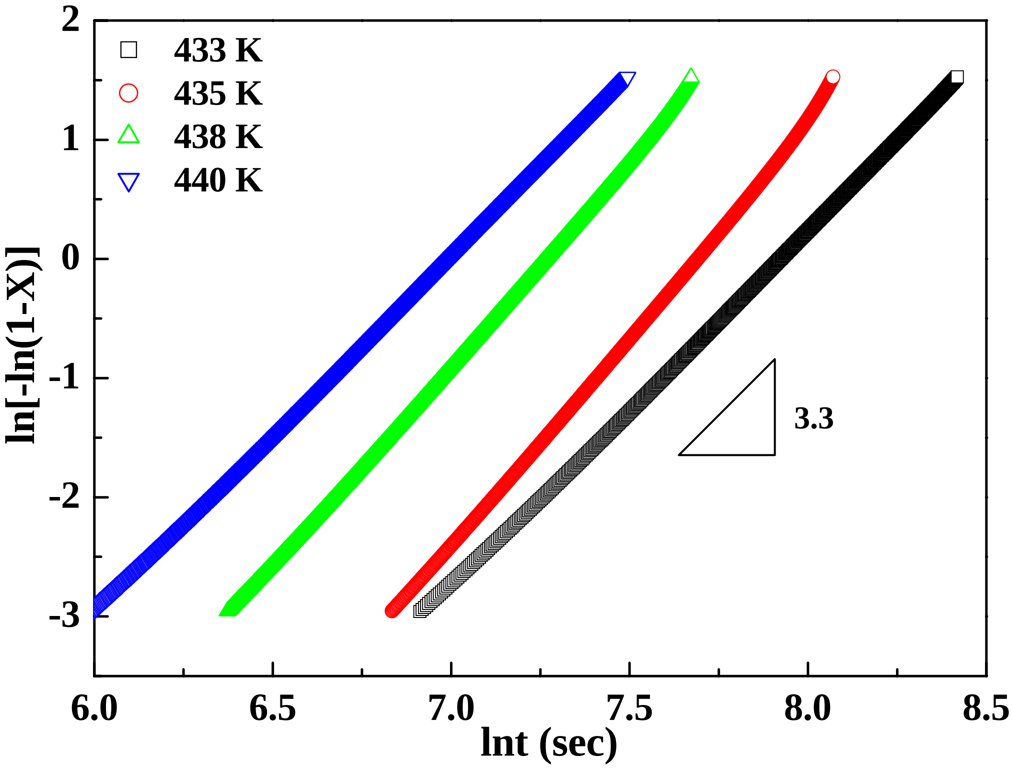

Fig. 4.34 The variation of Avrami exponent n for $Mg_{65}Cu_{22}Y_{10}B_3$.

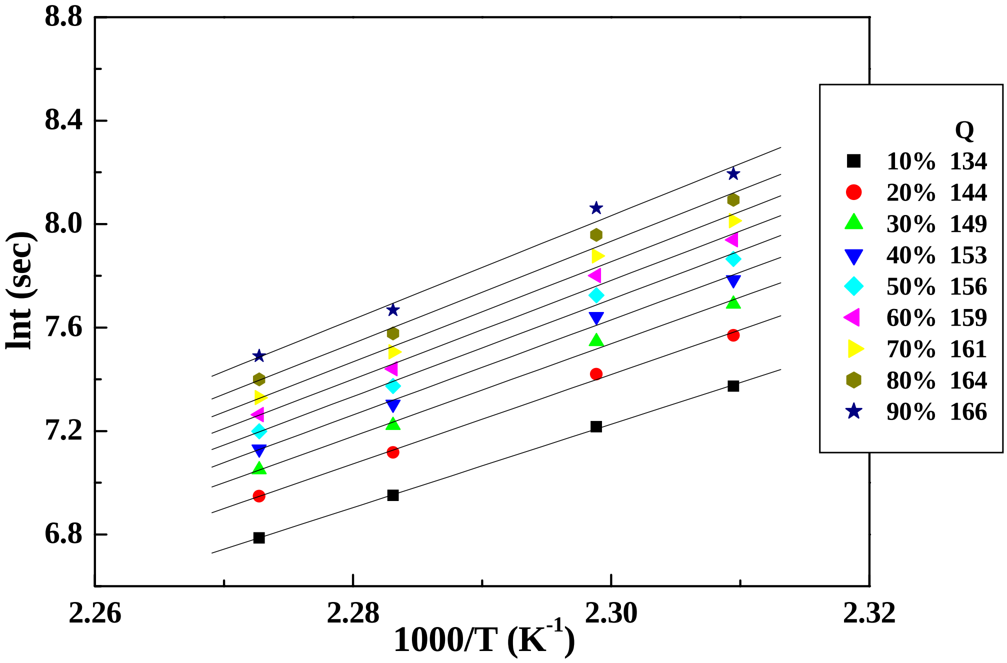

Fig. 4.35 Extraction of isothermal activation energy of the first crystalline phase for the $Mg_{65}Cu_{22}Y_{10}B_3$ amorphous alloy.

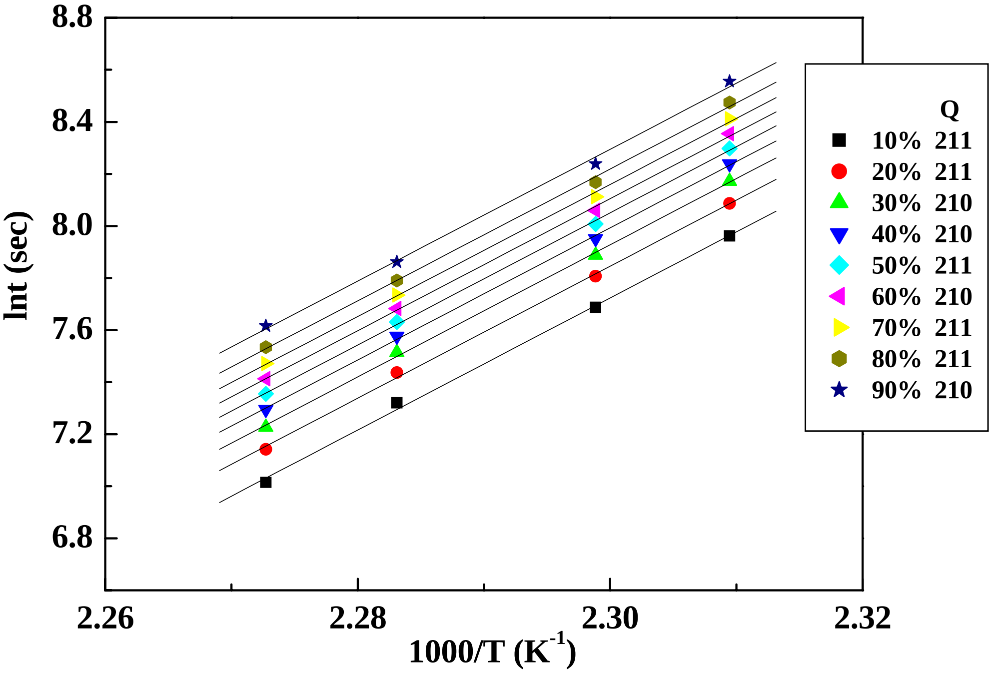

Fig. 4.36 Extraction of isothermal activation energy of the first crystalline phase for the $Mg_{65}Cu_{22}Y_{10}B_3$ amorphous alloy.

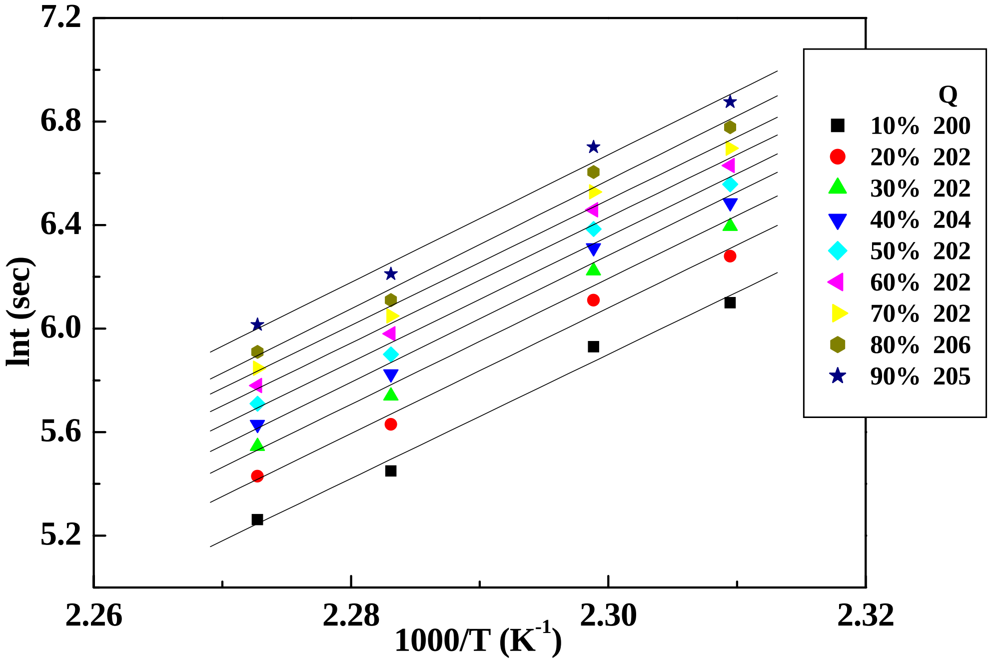

Fig. 4.37 Extraction of isothermal activation energy of the second crystalline phase for the $Mg_{65}Cu_{22}Y_{10}B_3$ amorphous alloy.

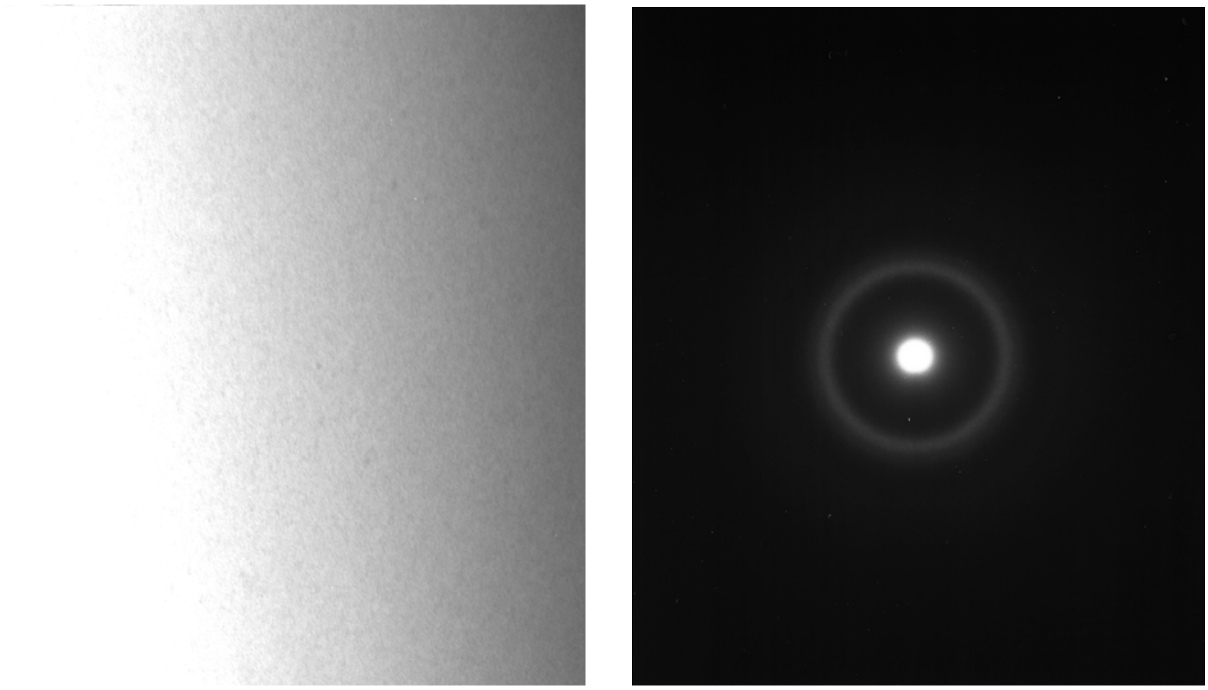
(a) (b)

Fig. 4.38 The TEM images of the as-melt-spun $Mg_{65}Cu_{22}Y_{10}B_3$ amorphous alloy: (a) Bright field image and (b) Selected area diffraction pattern.

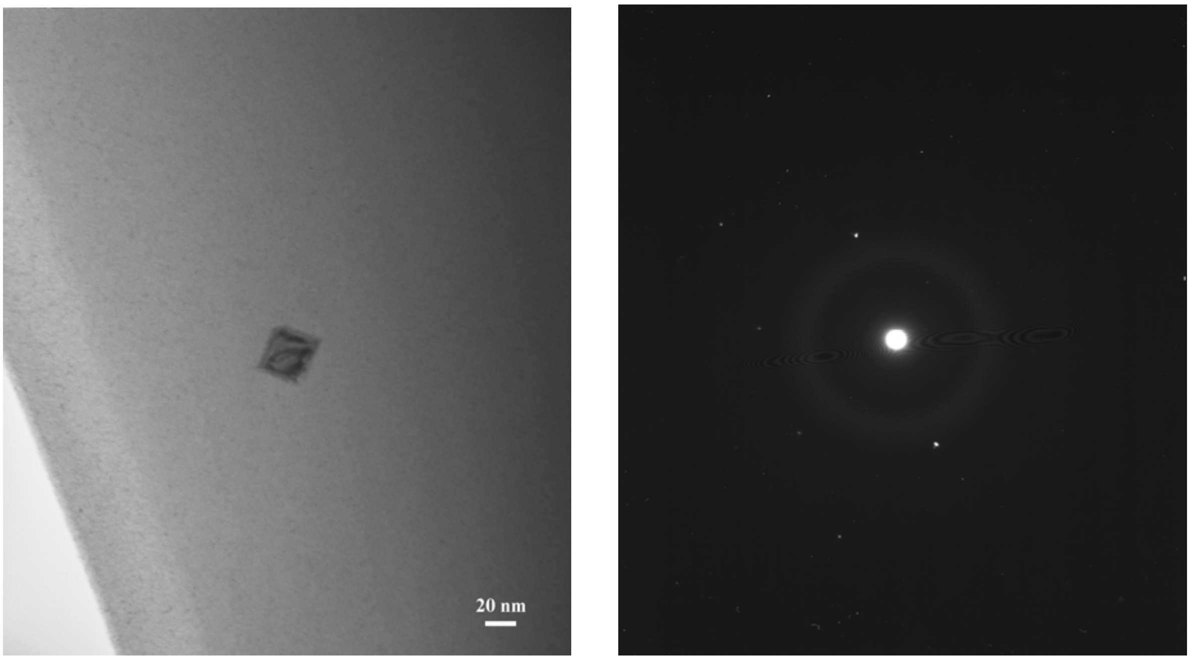

Fig. 4.39 The TEM images of the yttrium oxide particle in the as-melt-spun $Mg_{65}Cu_{22}Y_{10}B_3$ amorphous alloy: (a) Bright field image and (b) Selected area diffraction pattern.

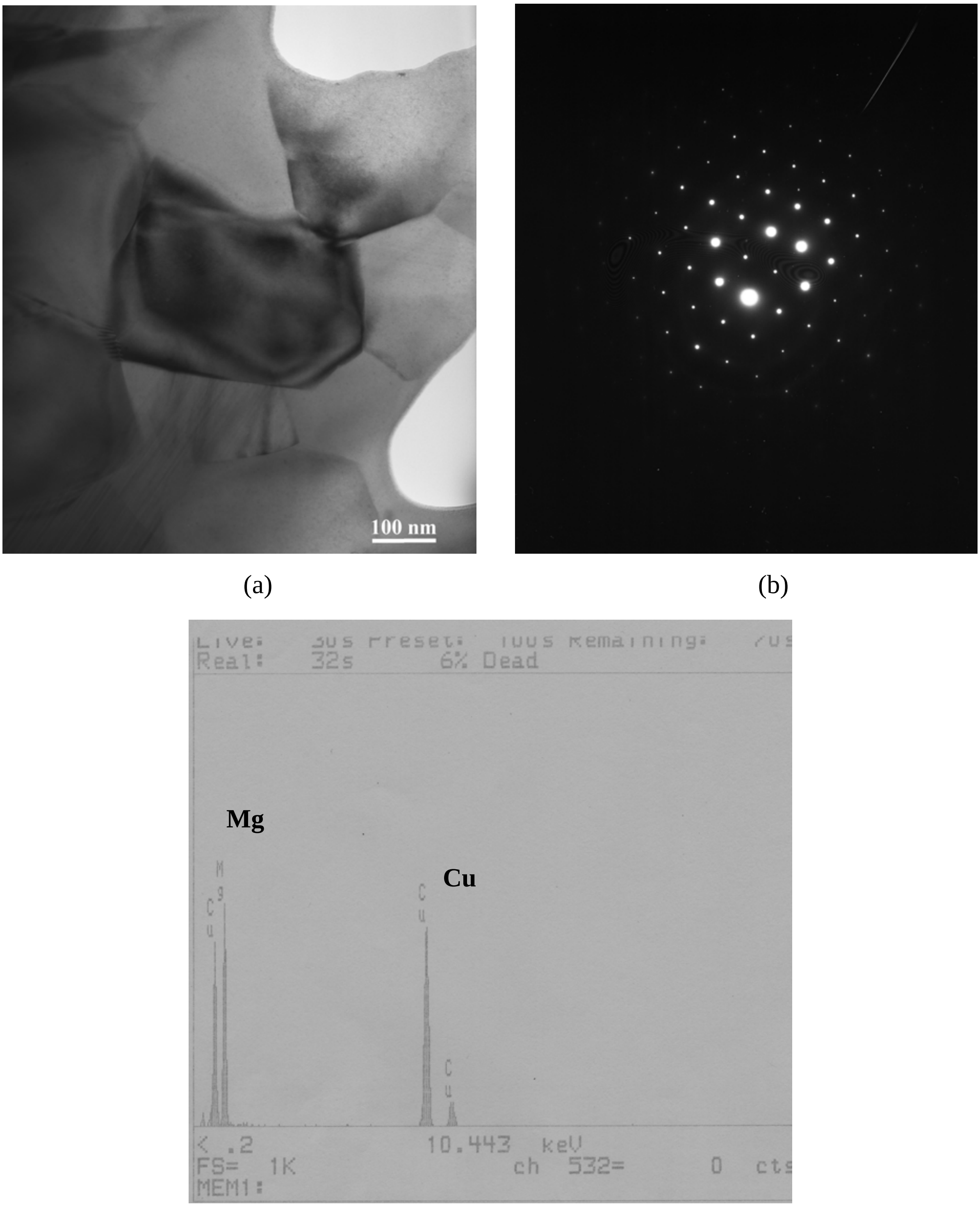

(a) (b)

(c)

Fig. 4.40 The TEM images of the crystallization in the $Mg_{65}Cu_{22}Y_{10}B_3$ amorphous alloy annealed to 670 K then cooled to room temperature: (a) Bright field image, (b) Selected area diffraction pattern, and (c) EDS analysis.

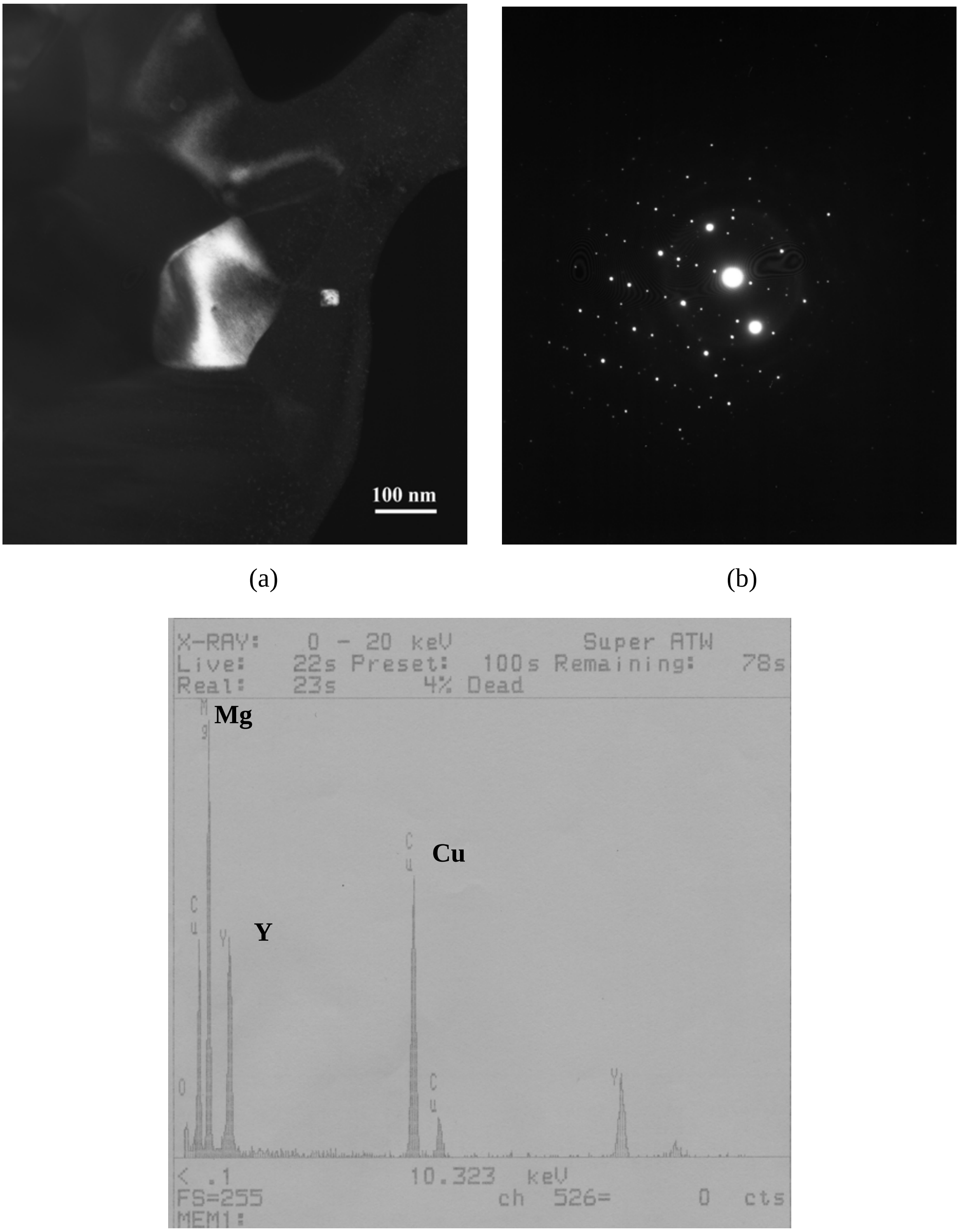

(a) (b)

(c)

Fig. 4.41 The TEM images of the crystallization in the $Mg_{65}Cu_{22}Y_{10}B_3$ amorphous alloy annealed to 670 K then cooled to room temperature: (a) Bright field image, (b) Selected area diffraction pattern, and (c) EDS analysis.

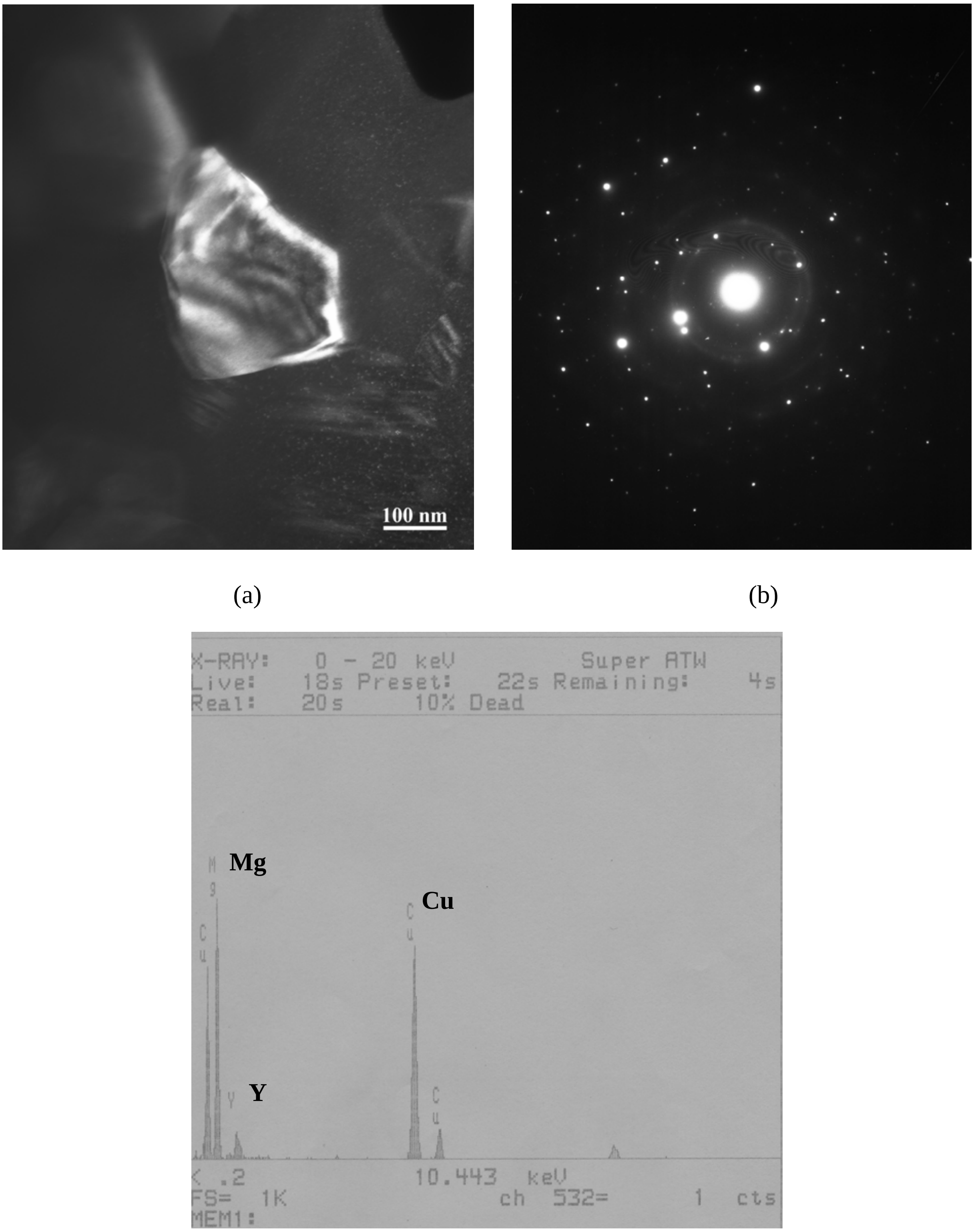

(a)

(b)

(c)

Fig. 4.42 The TEM images of the crystallization in the $Mg_{65}Cu_{22}Y_{10}B_3$ amorphous alloy annealed to 670 K then cooled to room temperature: (a) Bright field image, (b) Selected area diffraction pattern, and (c) EDS analysis.

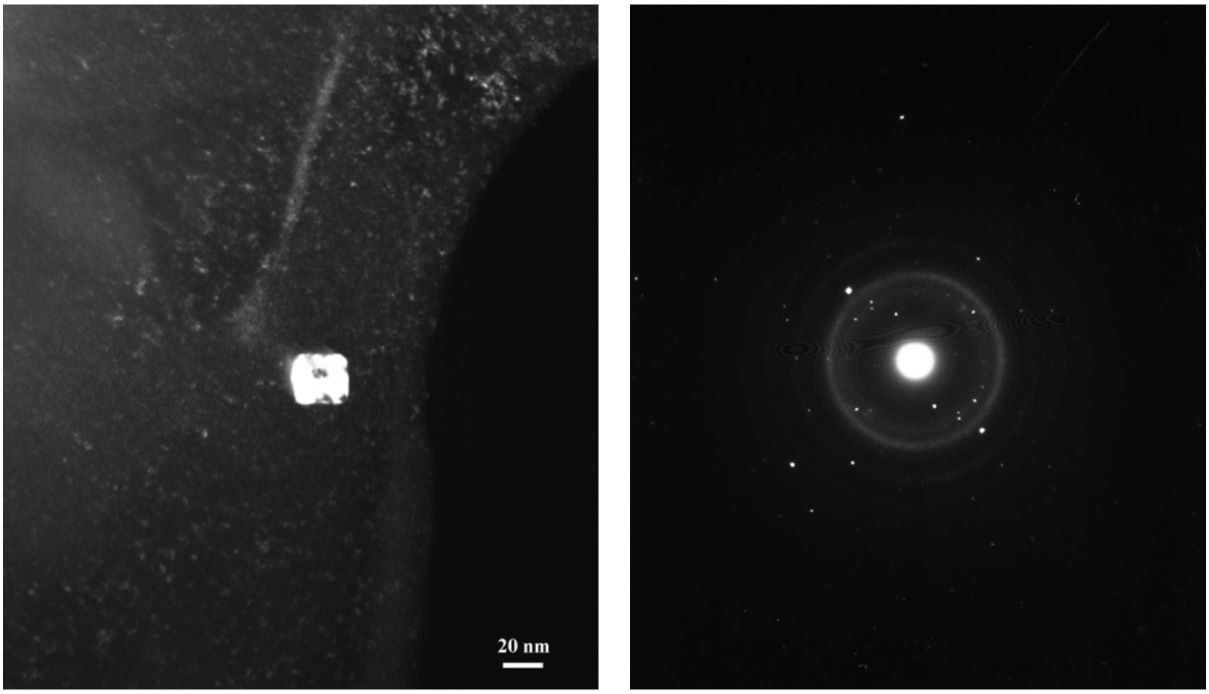

(a) (b)

Fig. 4.43 The TEM images of the crystallization in the $Mg_{65}Cu_{22}Y_{10}B_3$ amorphous alloy annealed to 670 K then cooled to room temperature: (a) Bright field image and (b) Selected area diffraction pattern.

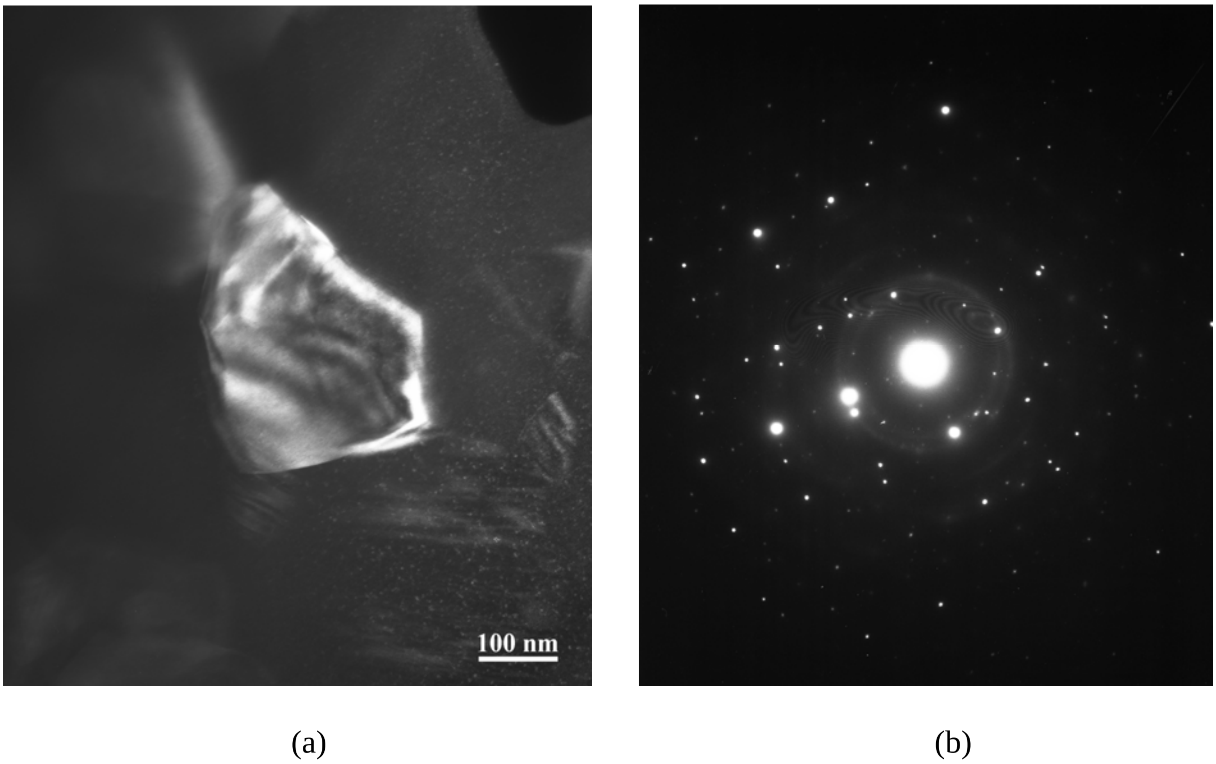

(a) (b)

Fig. 4.44 The TEM images of the crystallization in the $Mg_{65}Cu_{22}Y_{10}B_3$ amorphous alloy annealed to 670 K then cooled to room temperature. (a) Bright field image and (b) Selected area diffraction pattern.

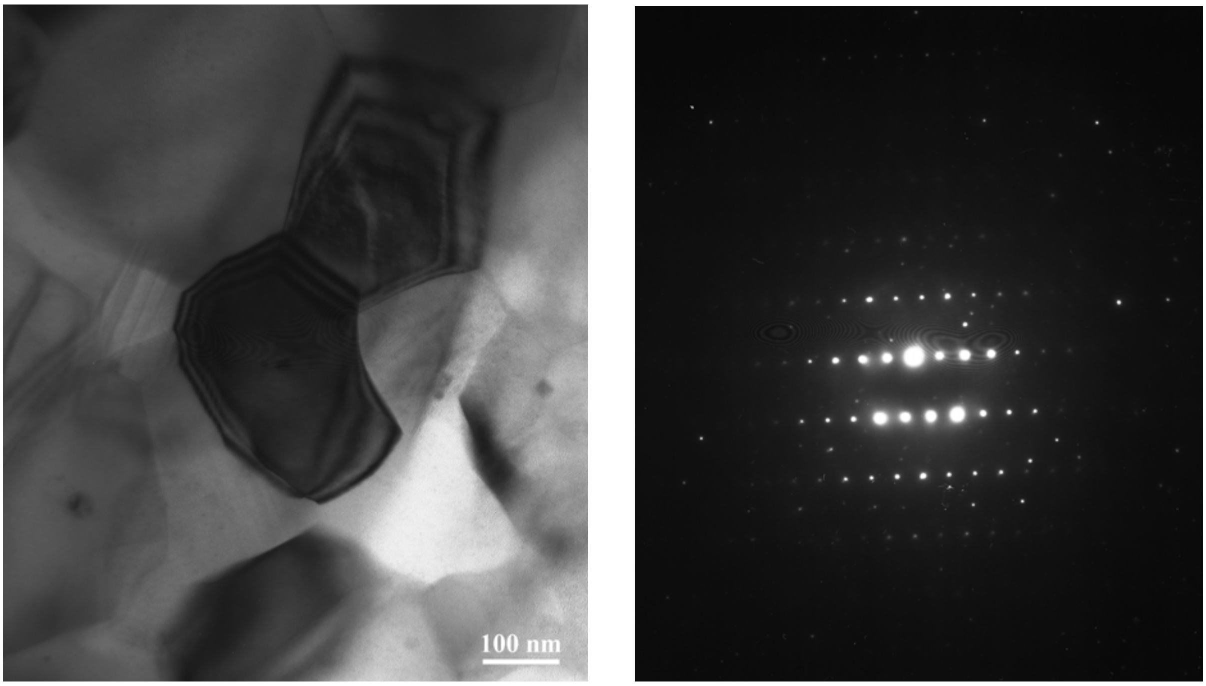

(a) (b)

Fig. 4.45 The TEM images of the crystallization in the $Mg_{65}Cu_{22}Y_{10}B_3$ amorphous alloy annealed to 670 K then cooled to room temperature: (a) Bright field image and (b) Selected area diffraction pattern.

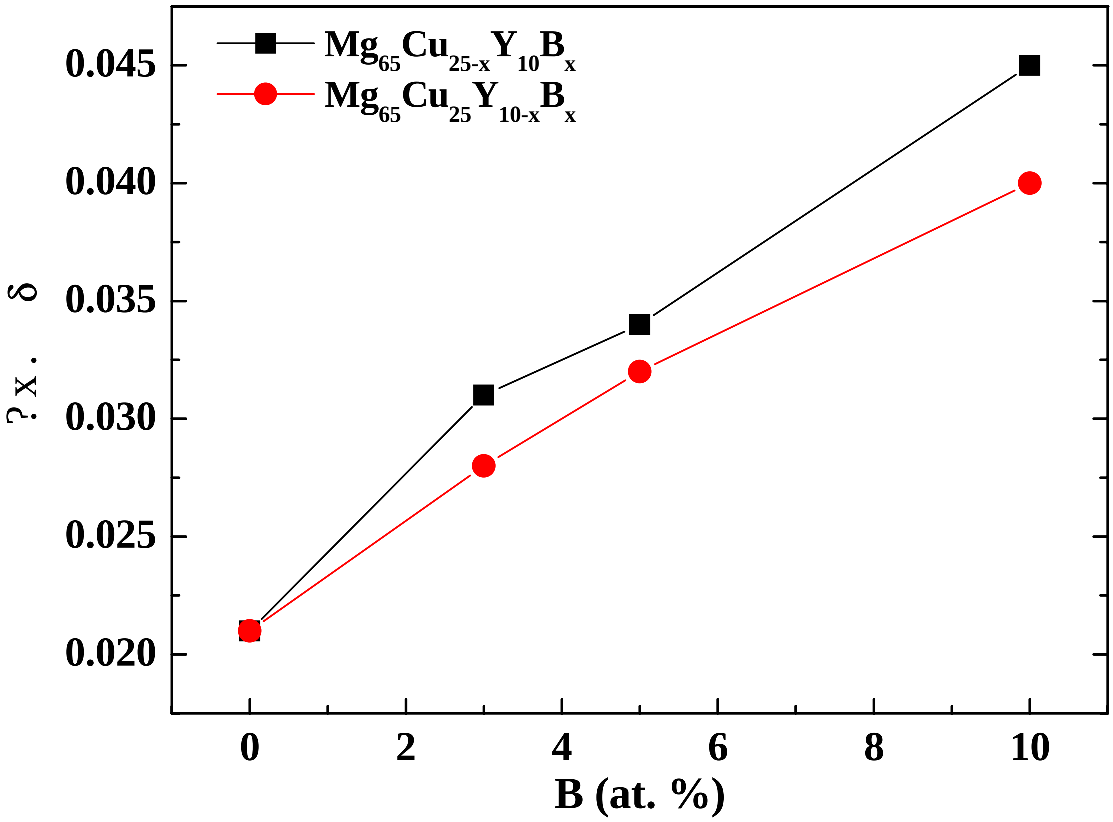

Fig. 5.1 Bonding parameter for the Mg-based alloys against boron content.

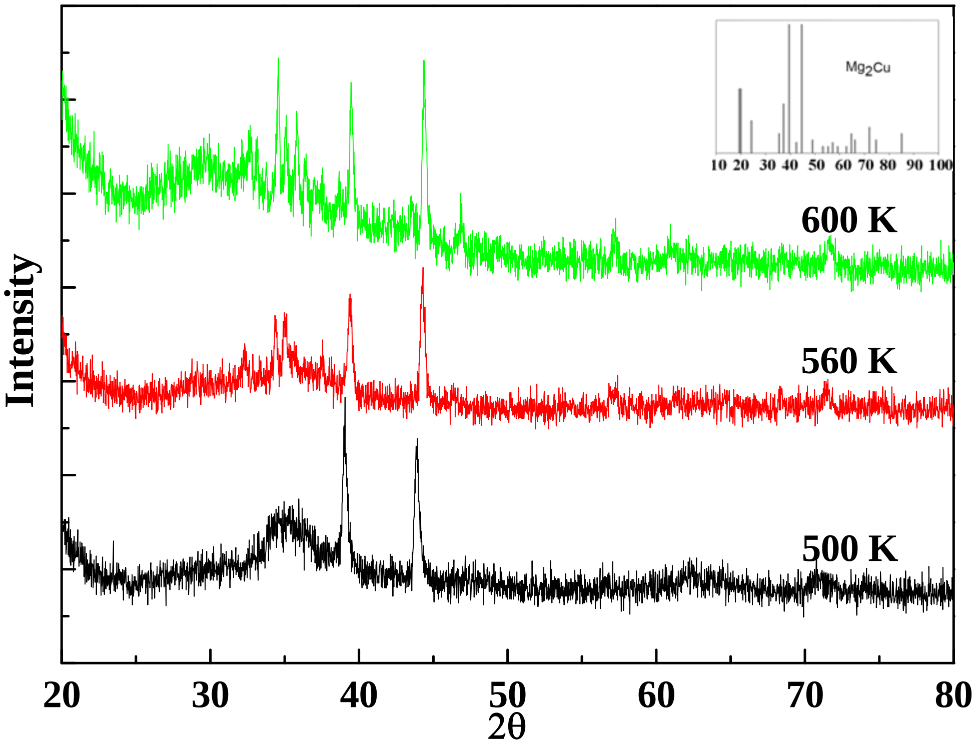

Fig. 5.2 The overall crystallization in the $Mg_{65}Cu_{22}Y_{10}B_3$.

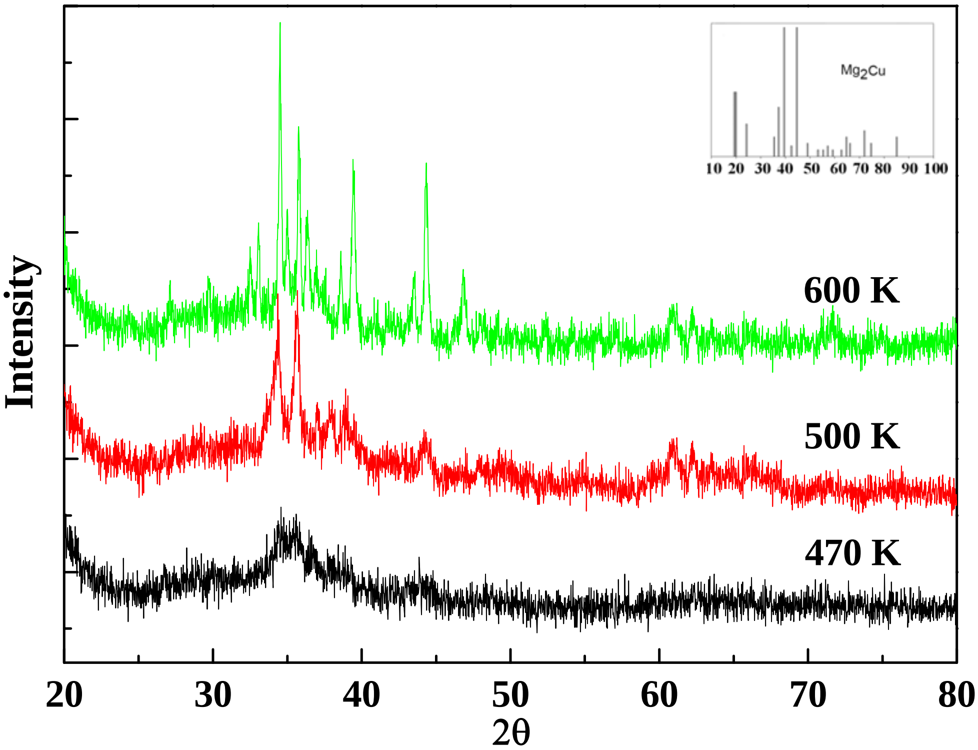

Fig. 5.3 The overall crystallization in the $Mg_{65}Cu_{15}Y_{10}B_{10}$.

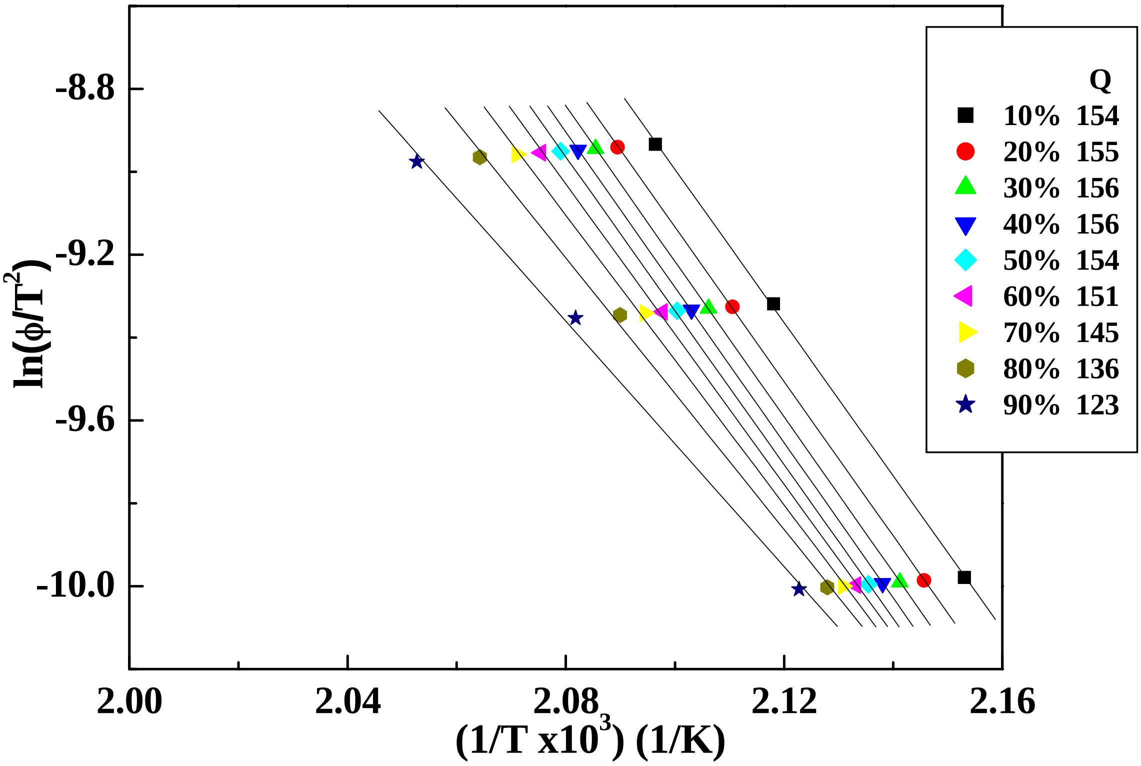

Fig. 5.4 Extraction of non-isothermal activation energy for the $Mg_{65}Cu_{25}Y_{10}$.

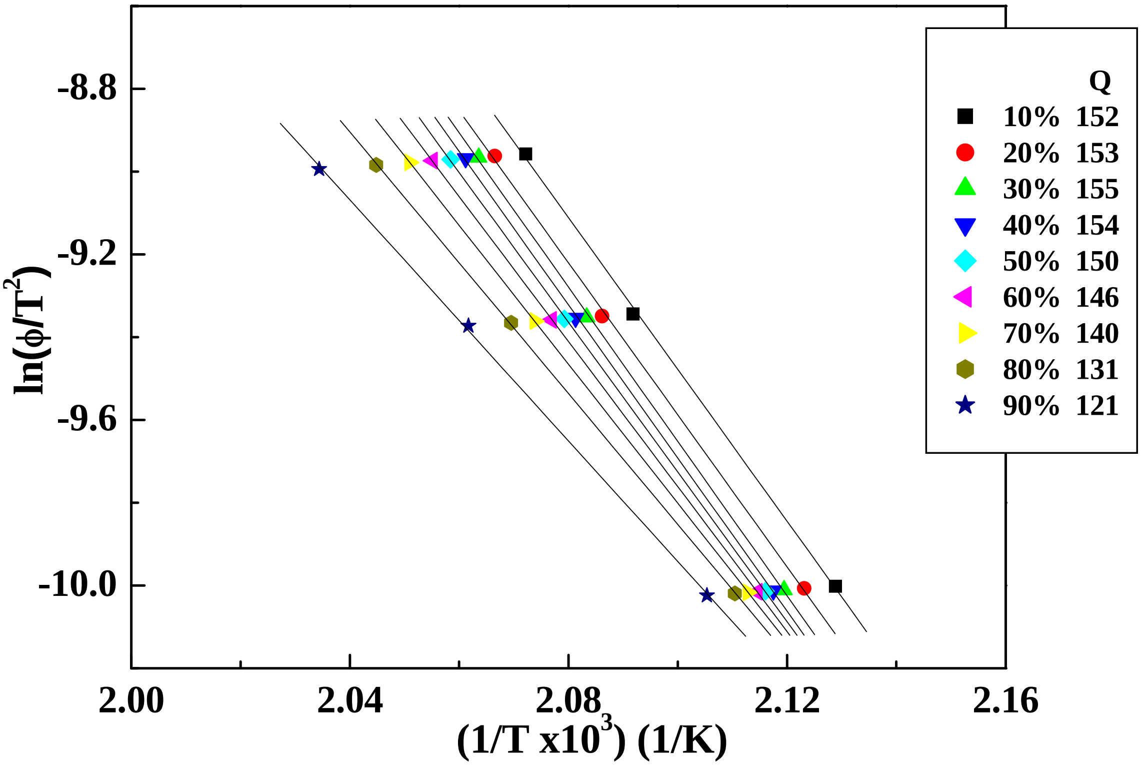

Fig. 5.5 Extraction of non-isothermal activation energy for the $Mg_{65}Cu_{22}Y_{10}B_3$.

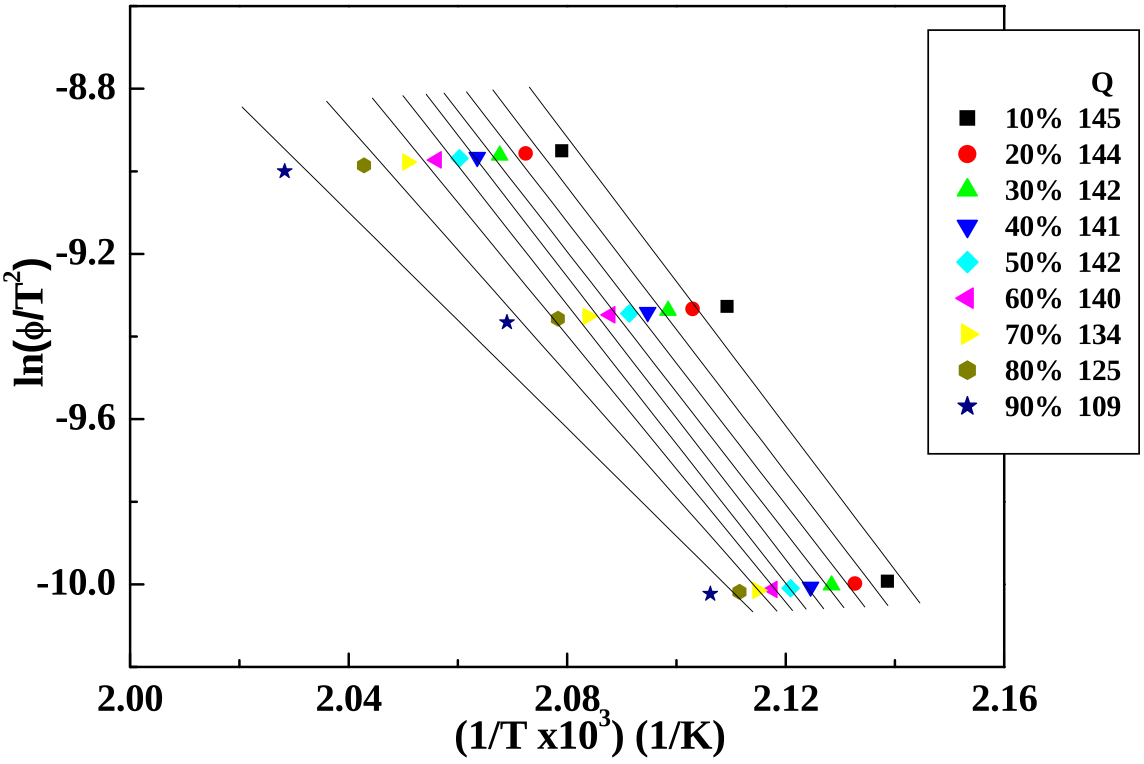

Fig. 5.6 Extraction of non-isothermal activation energy for the $Mg_{65}Cu_{20}Y_{10}B_5$.